Investigation of anisotropic properties of musculoskeletal tissues by high frequency ultrasound

Zur Erlangung des akademischen Grades

d o c t o r r e r u m n a t u r a l i u m (Dr. rer. nat)

Mathematisch-Naturwissenschaftlichen Fakultät I

Lakshmanan Sannachi, M.Sc. Phys.

Präsident der Humboldt-Universität zu Berlin

Prof. Dr. Jan-Hendrik Olbertz

Dekan der Mathematisch-Naturwissenschaftlichen Fakultät I

Prof. Dr. rer. nat. Andreas Herrman

Gutachter/in: 1. Herr Prof. Dr. Kay Raum

2. Herr Prof. Dr. Peter Fratzl

3. Herr Prof. Dr. Claus-Christian Glüer

Datum der Einreichung: 06. Januar 2011

Datum der Promotion: 03. Juni 2011

Zusammenfassung

Knochen und Muskel sind die wichtigsten Gewebe im muskuloskelettalen System welche dem Körper die Bewegungen möglich machen. Beide Gewebetypen sind hochgradig strukturierter Extrazellulärmatrix zugrundegelegt, welche die mechanischen und biologischen Funktionen bestimmen. Viele physiologische Gegebenheiten wie physischer Zustand, Alter, Genetik und medizinische Behandlungen beeinflussen die mechanischen und strukturellen Eigenschaften dieser Gewebearten. Um die Mechanismen zu verstehen, welche in gewebebeeinflussende Vorgänge involviert sind, muss nicht nur die Knochenquantität sondern auch die Knochenqualität in mikroskopischer und makroskopischer Größenordnung bekannt sein. Ultraschalltechniken sind im klinischen Umfeld für Gewebecharakterisierung außerordentlich gut geeignet. Sie haben den Vorteil den Gewebeaufbau und dessen funktionelle Eigenschaften auf verschiedenen Größenordnungen analysieren zu können.

In dieser Studie wurden die räumliche Verteilung der anisotropen elastischen Eigenschaften und der Gewebemineralisation im humanen kortikalen Femur untersucht. Zylindrische Stanzbiopsieproben wurden mit hochaufgelöster akustischer Mikroskopie (SAM) und Synchrotron-µCT (SR-µCT) analysiert. Für alle Proben wurden die elastischen Koeffizienten und die mittlere Gewebemineralisation mittels SAM beziehungsweise SR-µCT bestimmt. Die homogenisierten elastischen Eigenschaften wurden aus einer Kombination der mesoskalaren Porosität und der Gewebeelastizitätsmatrix mit Hilfe eines asymptotischen Homogenisierungsmodells ermittelt. Der Einfluss der Gewebemineralisierung und der Strukturparameter auf die mikroskopischen und mesoskopischen elastischen Koeffizienten wurde unter Berücksichtigung der anatomischen Position des Femurschaftes untersucht.

Es wurde ein Modell entwickelt, mit welchem der intramuskuläre Fettgehalt als Fleischqualitätsparameter des porcinen *musculus longissimus* nichtinvasiv mittels quantitativem Ultraschall mit einer Frequenz von 3,2 MHz und dessen spektraler Analyze des Echosignals bestimmt werden kann. Systembeeinflussende Effekte und Schallausbreitungseffekte mit Auswirkung auf die Spektralanalyse wurden analysiert und korrigiert. Muskelspezifische Parameter wie Dämpfung, *spectral slope*, *midband fit*, *apparent integrated backscatter* und cepstrale Paramter wurden aus den RF-Signalen extrahiert. Die

Einflüsse der Muskelkomposition und Strukturparameter auf die spektralen Ultraschallparameter wurden untersucht. Die anisotropen akustischen Eigenschaften von porcinem Muskelgewebe wurden auf Faserebene mit hochfrequenter Ultraschallmikroskopie untersucht. Die Parameter Schallgeschwindigkeit, Impedanz, Dämpfung und Elastizität werden durch die Muskelfaserorientierung beeinflusst und weisen höhere Werte parallel zur Faserlängsrichtung als senkrecht zur Faserorientierung auf. Die größte Abhängigkeit von der Faserorientierung wurde bei der Dämpfung gefunden. Beim Vergleich von akustischen Eigenschaften mit histologischen Schnitten mittels Bildregistrierung zeigten sich keine signifikanten Unterschiede zwischen den individuellen Fasertypen.

Die in dieser Studie gewonnenen detaillierten und lokal bestimmten Knochendaten können möglicherweise als Eingabeparameter für numerische 3D FE-Simulationen dienen und damit die gewöhnlich genutzte Annahme eines homogenen und isotropen Knochengewebes ablösen. Darüber hinaus kann die Untersuchung von Veränderungen der lokalen Gewebeanisotropie neue Einsichten in Studien über Knochenumbildung geben, wie es beispielsweise in Hinblick auf Frakturheilung, Knochenerkrankungen, Alter oder Anpassung an veränderte Belastungszustände an Knochen-Implantat-Grenzflächen nach endoprothetischen Operationen der Fall ist. Diese auf Gewebeebene bestimmten Daten von Muskelgewebe können in numerischen Simulationen von akustischer Rückstreuung genutzt werden um diagnostische Methoden und Geräte zu verbessern.

Schlagwörter: Akustische Impedanz, Anisotropie, elastische Eigenschaften, akustische Mikroskopie, kortikaler Knochen, intramuskuläres Fett, Muskel, Cepstrum, integrierte Rückstreuung

Abstract

Bone and muscle are the most important tissues in the musculoskeletal system that gives the ability to move the body. Both tissues have the highly oriented underlying extracellular matrix structure for performing mechanical and biological functions. Many pathological conditions such as physical condition, age, genetic background and treatment change the mechanical and structural properties of these tissues. In order to understand the mechanisms involved in tissue alteration due to several conditions, not only bone quantity, but also its quality needs to be characterized at microscopic and macro molecular tissue level. Ultrasound technique shows considerably more promise for the tissue characterization within a clinical setting. It has ability to assess tissue architecture and function properties at multiple scales.

In this study, the spatial distribution of anisotropic elastic properties and tissue mineralization within a human femoral cortical bone shaft were investigated. Cylindrically shaped punch biopsy samples were analyzed using high resolution ultrasonic cylindrical scanning microscopy (SAM) at 50 MHz and synchrotron radiation μCT (SR-μCT). For all samples the average tissue elastic coefficients and average tissue mineralization were derived from the SAM and SR-μCT measurements, respectively. The homogenized meoscopic elastic properties were determined by a combination of mesoscale porosity and tissue elastic matrix using a asymptotic homogenization model. The impact on tissue mineralization and structural parameters of the microscopic and mesocopic elastic coefficients was analyzed with respect to the anatomical location of the femoral shaft.

A model was developed to estimate meat quality parameter, intramuscular fat of porcine *musculus longissimus* non-invasively using a quantitative ultrasonic device with a frequency of 3.2 MHz by spectral analysis of ultrasonic echo signals. System specific effects and sound propagation effects on the spectral analysis were analyzed and corrected. Muscle specific acoustic parameters, i.e. attenuation, spectral slope, midband fit, apparent integrated backscatter, and cepstral parameters were extracted from the measured RF echoes. The impact of muscle composition and structural properties on ultrasonic spectral parameters was analyzed. The anisotropic acoustic properties of this porcine muscle were investigated at fiber level using a high frequency scanning acoustic microscope. The parameters: speed of sound, impedance, attenuation and elastic coefficient were affected by the muscle fiber

orientation and have higher values along fiber long axis compared to those in the direction perpendicular to the long fiber axis. The most dominant direction dependency was found for the attenuation. A comparison of the acoustic properties with site-matched histological images did not reveal significant differences between the individual fiber types.

The detailed locally assessed bone data in this study may serve as a real-life input for numerical 3D FE simulation models instead of the commonly used assumption that bone tissue is homogeneous and isotropic. Moreover, the assessment of changes of local tissue anisotropy may provide new insights into the bone remodelling studies, e.g., in the course of fracture healing, bone pathologies, aging, or adaptation to modified loading conditions at the bone-implant interface after endoprothetic surgeries. The data provided at tissue level and investigated ultrasound backscattering from muscle tissue, can be used in numerical simulation FE models for acoustical backscattering from muscle for the further improvement of diagnostic methods and equipment.

Keywords: Acoustic impedance, anisotropy, elastic properties, acoustic microscopy, cortical bone, intramuscular fat, muscle, cepstrum, apparent integrated backscatter

Table of Contents

List of figures

List of tables

Abbreviations and Nomenclature

Abbreviations

AR	Anisotropy ratio
ANOVA	Analysis of variance
BF	Back fat
HA	Hydroxyapatite
HC	Haversian canal
IS	Interstitial Tissue
OS	Osteon
PBS	Phosphate buffered saline
PMMA	Polymethylmethacrylate
RF signal	radio frequency signal
ROC	Radius of curvature
ROI	Region of interest
SAM	Scanning acoustic microscope
SOS	Speed of sound
SR-μCT	Synchrotron radiation micro computed tomography
STO, FTG, FTO	Muscle fiber types: slow-twitch oxidative, fast-twitch glycolytic and fast-twitch oxidative
TGC	Time gain compensation

Nomenclature

α	Attenuation
C	Transverse isotropic stiffness matrix
c_{ij}	Elastic or stiffness coefficient
$c_{HA}, c_{coll}, c_{H20}$	Elastic tensor of hydroxyapatite, collagen and water
ρ	Mass density
d	Thickness
f	Frequency
k_{HA}, k_{H2O}	Bulk modulus of hydroxyapatite and water
μ_{HA}, μ_{H2O}	Shear modulus of hydroxyapatite and water
γ	Poisson's ratio
$S(f,z)$	Power spectrum function of frequency and distance
τ_{max}	Cepstrum maximum peak time value
v	Speed of sound
$V(\theta,t)$	Voltage with respect angle and time
vf_{HA}, vf_{coll}	Volume fraction of hydroxyapatite and collagen
λ	Wavelength
Z	Acoustic impedance

Thesis Outline

Chapter 1 Introduction: 1) Establishes the importance of musculoskeletal tissue elastic and structural properties investigation, and carries out literature survey of these tissue type's ultrasonic studies and their drawbacks and finally the aims of this study. 2) Discusses skeletal muscle physiology and anatomy in order to develop a basic knowledge which is necessary before an explanation of the interaction between ultrasound and skeletal muscle can be attempted. 3) Discusses many of the fundamental acoustic equations and the interaction of acoustic wave with simple homogeneous material, inhomogeneous materials and biological tissue like bone and muscle.

Chapter 2 Materials and methods: 1) Discusses some of the other techniques used for musculoskeletal tissue characteristics. 2) Explains the principle of the scanning acoustic microscope. 3) Explains the preparation of samples, techniques and methods used to estimate the acoustic, structural and chemical composition of the bone and muscle at microscopic and macro molecular levels.

Chapter 3 Results: Explains the anisotropic acoustic properties at microscopic level, chemical and structural properties, correlation between the acoustic and chemical composition, acoustic properties at macroscopic level and influence of the structural and chemical properties on the acoustic parameters.

Chapter 4 Discussions: Discusses the results obtained at microscopic and macroscopic levels.

Chapter 5 Summary: Looks into the holistic aspects of the work that was undertaken and presents a general summary.

Chapter 6 References: Cites all the published papers and book articles that were referred to in this thesis.

I Introduction

I.1 Musculoskeletal system

A musculoskeletal system is an important organ system that gives the ability to move the body. It is comprised of several tissue types. Its primary functions are supporting the body, protecting vital organs and allowing motion. Large tissue part involving for this function properties in this system are bone and muscle. Skeletal bone is the main storage system for calcium and phosphorus and provides stability to the body. In contrast to most other tissues, bone is able to heal and has capacity to restore its structure and function. Muscles keep bones in place and also play a role in the movement of the bones. Both bone and muscle have the highly orientated underlying extracellular matrix structure to perform mechanical, biological and chemical functions.

Many pathological conditions such as physical condition, age, genetic background and treatment change the mechanical and structural properties of both bone and muscle tissues. There are a number of medical imaging techniques that are used to assess the functional properties of musculoskeletal tissues in every day clinical diagnosis. Ultrasound, computed tomography, magnetic resonance imaging and nuclear medicine being the most common. Among them, ultrasound technique shows considerably more promise for the tissue characterization within a clinical setting. For a clear understanding the effect of various pathological conditions on a biological system, the micro architecture and functional properties of that system at tissue level should be analyzed. The ultrasonic technique has the advantage that it is able to assess those properties at multiple-scale.

The following sections list the, important features of both bone and muscle tissue types, the type of specimen selected in this study, and the modalities available for understanding their function properties and their drawback, contain a discussion on how to solve these problems and finally, outline the aim of this study.

I.1.1 Cortical bone

Stiffness is one important characteristic of bone material biomechanical competence. It depends on material and structural properties at several hierarchical lengths scales (Fig. I.1). The mechanical properties of bone are altered in the aging population and in osteoporotic patients [1;2]. Another important feature of bone tissue is its capacity of regeneration, which is most evident as an endogenous healing after a traumatic fracture, but also occurs permanently and through the entire skeleton in a process called remodeling. These characteristics lead to a tissue compound that is not only highly heterogeneous and anisotropic at all hierarchy levels as a result of perfect adaptation to external and intrinsic loading conditions, but also dynamic with respect to tissue resorption, synthesis, and maturation. Mineralization of the collagen fibrils is a process that can be divided into two phases. First phase is called primary mineralization which is a fast process that is associated with mineral deposition into the newly formed osteoid. Second phase is called secondary mineralization, which is a slow process associated with further intra- and interfibrillar mineral depositions, crystal growth and maturation over a period of several years [3].

It is well accepted that not only bone quantity but also its quality needs to be characterized to understand the mechanisms involved in bone alteration due to several conditions such as physical condition, nutrition, age, pathologies and treatment [4]. Usually, the mechanical properties of bone have been measured at the macroscopic level using standard mechanical testing. However, the primary source of alteration of bone mechanical integrity has to be found at tissue level such as defects of mineralization and collagen stability [5-7] or microstructural anomalies. Consequently, methods for direct analysis of bone microarchitecture [8;9], mineralization [10;11], and mechanical properties [12;13] at the microscopic scale are required to assess the effects of various physiopathological conditions, aging or even the effectiveness of treatments. That fulfills the knowledge gap existing between tissue alterations and the resulting mechanical behavior at the macroscopic scale.

High-resolution imaging modalities, e.g. micro-computed tomography [14;15], synchrotron radiation μCT [16-18] and micro-magnetic resonance imaging [19], have been applied in addition to histomorphometric analysis for assessing three-dimensional microstructural properties *in vitro*. Among them, x-ray microradiography [20] and monochromatic SR-μCT [18] measurements provide complementary information about

mineralization at tissue level in 2D or 3D, respectively. However, the main limitation of these techniques is that they are unable to give bone elastic properties at tissue level.

However, several mathematical models have been developed to predict bone elasticity from the degree of mineralization [21;22] most often radiographic measurements e.g., dual-energy x-ray absorptiometry, quantitative computed tomography and SR-μCT. Although several studies have showed increase in mineralization with respect to tissue stiffness, the principal relation between them is not yet clear and, given the typical variation in density and elasticity in most materials [23]. It concludes that mineral density will not be able to determine tissue elasticity with sufficient accuracy. Particularly, information about tissue anisotropy cannot be obtained from the measurement of mass density. High resolution measurement techniques such as nanoindentation or scanning acoustic microscopy is needed to measure elasticity at tissue-level [24;25].

Nanoindentation [13;26] and acoustic microscopy [27] are directed at measuring material elastic properties and their anisotropy. Nanoindentation is a micro-probing method which allows the measurement of elastic modulus with a spatial resolution in some cases of better than 1 μm [12;13;28]. Although nanoindentation allows highly localized estimates of elastic properties in several locations at the sample surface, it is not adapted to providing a detailed spatial distribution of the elastic properties at the specimen surface. This represents a current limitation of this technique, given that bone is a non-uniform and heterogeneous material.

Ultrasonic techniques evaluate bone mechanical properties and offer advantages over direct biomechanical testing given their nondestructive character (avoiding damage to the material during the test). Multi-scale assessment of bone elastic properties is possible using ultrasonic methods. These methods have been widely used for the *in vitro* investigation of bone specimens elastic properties both at the macroscopic or structural level [28-31] and microscopic or tissue level [27;32;33]. They are suitable for measuring the regional variations of elastic properties at different scales which include [30;31] or exclude the cortical porosity [4;25;27;34]. Scanning acoustic microscopy (SAM) used in reflection is a nondestructive imaging technique which has been used for the analysis of bone with spatial resolutions in the 1–140 μm range depending on the ultrasonic frequency and transducer characteristics [27]. SAM images represent the spatial distribution of the material surface acoustic reflectivity.

Using an adequate calibration procedure, acoustic reflectivity can be translated into acoustic impedance values, which is depends on tissue material properties such as density and elasticity of the material in the probing direction [27;35;36]. When combined with local density estimates (e.g., such as X-ray micro-computed tomography data), acoustic impedance estimates can be used to derive tissue stiffness [4;25;37]. Furthermore, it has been shown that Z alone is an excellent proxy for the tissue stiffness coefficient in the probing direction [34;36]. Therefore, SAM is an appropriate micro-imaging technique for quantitatively assessing the microstructure and the spatial distribution of elastic properties of highly heterogeneous materials like bone.

The femur is the longest, strongest, and heaviest bone in the human body. It is one of the principal load bearing bones in the lower extremity [38;39]. It is a common skeletal site of fracture in elderly people. Osteoporotic fractures of the femur usually represent an early sign of osteoporosis and may announce future fractures at other sites such as the radius or the spine. Femoral shaft fractures often occur due to high energy forces such as motor vehicle collisions. The complications and injuries associated with femur fractures in the adult can be life-threatening and may include hemorrhage, internal organ injury, wound infection, fat embolism, and adult respiratory distress syndrome [40]. The assessment of cortical bone at the radius using X-ray densitometry techniques may be used as a diagnostic tool to predict fracture risk [41] and to initiate therapeutic actions [42;43]. With the advent of a new generation of quantitative ultrasound (QUS) devices measuring *in vivo* the speed of sound at the proximal femur [44-46], a parameter sensitive to porosity and tissue stiffness [37;47], it becomes necessary to quantitatively assess the microstructure and tissue properties of the femur. For example, combined knowledge of the fine heterogeneous spatial distribution of both bone microstructure and elastic properties [4;25;34] can be used as input in computational models such as finite-difference methods. It provides insight into the propagation of elastic waves in the femur in an attempt to elucidate what bone properties are revealed by quantitative ultrasound techniques and is also beneficial to finite-element modeling in relating the heterogeneous tissue elastic characteristics to the macroscopic biomechanical behavior of the whole bone at a site of frequent fracture.

In previous studies, the elastic properties of the human femoral cortical bone were analyzed with a limited number of specimens and bone range covered was between 40% and 70% of the total length of the femur [30;33;48;49]. In addition, each measurement made was

still of a discrete nature. Even though such studies were able to provide some detailed information, their discreteness prevented them from providing a continuous model for the whole bone, since they did not cover an entire bone. Their work was mainly of an experimental nature in the sense of a test of their ultrasonic technology. One study [50] was found with a range of 15% to 85% of femur length, even though only elastic constants for the main diagonal of the reduced fourth order stiffness tensor were analyzed in this range. However, those studies were carried out with frequency range of 2 – 5 MHz which determines the elastic properties by both bone matrix and porous structure.

I.1.2 Skeletal muscle

The most important and unique feature of skeletal muscle tissue is able to contract in order to move the bones when stimulated by nerve impulses [51]. In this, muscle fibers are stacked lengthwise are surrounded by connective tissue. In a strong contraction the length of a muscle is reduced to about 60 percent of its length when relaxed. Many pathological conditions exhibit a change in mechanical and structural properties of muscle [52-54]. Muscle dystrophy is a hereditary, degenerative skeletal muscle disease in which the contractility of muscle decreases as a result of a loss in the ability of collagen fibers to distend [55;56]. The two most notorious variations, Duchenne and Becker comprise the main of cases and are extremely debilitating. Meat industrial interest in the muscle structure and constituents is interested with the nutritional value of the tissue. The quality of the meat is related to the marbling or fat % in the tissue [53;57;58]. Muscles with a reasonable percentage of fat are ranked as more tender and favorable. The ability to accurately determine the quality of meat based on tissue composition has great economic value to the meat industry.

Pork is the most important meat in Germany with approximately 60 kg consumed per capita and year. Factors like pig breed, gender, feeding, ante mortem handing and post mortem treatment haved been shown to affect the final meat quality of the economically important loin *longissimus* muscle [59]. The intramuscular fat content is widely considered as one of the major parameters influencing qualify and sensory characteristics of meat [60]. The IMF range from 2 to 3.5% in porcine *longissimus* muscle at the $2^{nd}/3^{rd}$ rib have been proposed as benchmarks for optimal taste [61-63]. However, recent investigations performed in German pig populations revealed average IMF values of about 1 to 1.5% indicating that only

a minority of the animals actually reach the proposed minimum IMF threshold level of 2% [64].

For the establishment of a sensory quality based marketing system, the classification of meat according to the IMF levels is necessary. Several techniques have been proposed to estimate the IMF on hanging pig carcasses. Infrared spectroscopy [65] and dual energy X-ray absorptiometry [66] and magnetic resonance imaging [67] have been shown to be reasonably correlated with IMF. However, these methods are time consuming, therefore they may have only limited suitability for high throughput analyses on hot carcasses in common slaughter facilities. Ultrasound is a fast and non-destructive method that has been demonstrated to be a promising alternative for the prediction of IMF. First studies have either measured the sound velocity [68;69] or have analyzed the texture of the gray scale backscatter images [58;70]. Although these methods have been quite successful in the prediction of IMF in living steers and hot carcasses with R^2 values up to 0.75 [70-72], the studies performed in porcine muscle were less predictive ($R^2 \leq 0.4$) [73;74].

During the last decade, spectral analysis of the backscattered ultrasound signals has been shown to provide more detailed information about tissue constitution compared to conventional image texture or sound velocity analyses [75;76]. One major advantage of spectral analysis of the radio frequency RF backscatter signals is that it contains quantitative information composition and elastic properties of structures that are comparable to or smaller than the acoustic wavelength. The frequency dependence of acoustic backscatter can therefore be used to quantify structural dimensions that are not visible in the ultrasound image or to differentiate different tissue types [77-80]. In muscle tissue, the major acoustic inhomogeneities are considered to be the connective tissue interfaces between adjacent muscle fibers and between muscle bundles [75]. Alterations of this structure can be considered to affect the backscatter spectrum. Lizzi [81] has introduced several spectral parameters that are related to the structure of the scatterers. While the slope of the obtained power spectrum *m* (dB/MHz) is related to the size, midband fit (dB, value of the linear fit at the center frequency) and spectral intercept *I* (dB, extrapolated amplitude value at 0 MHz) are affected by size, concentration, and impedance of the scatterers [81;82]. Another common spectral estimate is the apparent integrated backscatter amplitude *AIB* (dB, power spectrum within the bandwidth of the transducer) [83]. Tissue boundaries that are separated at distances larger than the wavelength and the spatial resolution limit of the imaging system, e.g., the

marbling structure in muscle, can often be seen directly in the US grayscale images. A precise estimation of distance distributions along the sound propagation path from RF signals is possible using cepstral analysis [84].

The composition of connective tissue is affected by several parameters, e.g., age or breeding. Moreover, IMF is known to alter the connective tissue structure due to the deposition of fat inside the perimysium, i.e. between the muscle fiber bundles [85]. This deposition is associated with a partial destruction of the connective tissue honeycomb structure, which reduces mechanical strength and shear modulus of the tissue [53;54] and explains the association with sound velocity. On the other hand, the acoustic properties of fat are remarkably different from those of muscle and connective tissue. Therefore, an increasing amount of fat deposited between muscle fibers and fiber bundles is hypothesized to alter the characteristics of the backscatter power spectrum and to increase the amplitude of reflections at muscle bundle boundaries. Moreover, an increase of backscatter and reflections amplitudes should result in an increase of the attenuation in muscle [86;87].

Thus far, only few studies have focused the use of spectral analysis to predict the IMF content of bovine muscle [76;88] and porcine muscle [89]. The latter performed analysis of unprocessed backscatter signals obtained with a medical diagnostic ultrasound device to estimate the intramuscular fat content of porcine loin muscle. Although promising results could be obtained (root mean squared error of prediction RMSEP = 0.36%), neither the instrument nor the prediction errors have yet proved satisfying for industrial use at slaughter. A prerequisite of a reliable ultrasound spectral analysis is an exact knowledge of the sound properties at the region of interest (ROI). These properties are affected by system properties, e.g., center frequency, bandwidth and sound field produced by the transducer, but also by refraction and attenuation in all tissues along the sound propagation path [90]. The incorporation of sophisticated calibration and correction methods is anticipated to improve the accuracy of ultrasound based IMF predictions [91].

Many different models have been proposed to extract statistically averaged information from the backscattered radio frequency signals measured within a distinct tissue volume. In recent years, the microstructural tissue features have been successfully derived by fitting the measured backscatter spectrum to a theoretical backscatter model that uses form factors. Form factors are functions that approximate the backscatter characteristics of a single

scattering structure according to geometry and elastic properties of the scatter and the surrounding medium [92;93]. The convergence of fitting between measured and theoretical predicted backscatter spectrum can be increased with some restriction of model parameters, e.g., with a prior knowledge of scatter size, density and relative acoustic impedance change.

I.1.3 Specific Aims

The specific aims are to estimate the anisotropic acoustic properties of cortical bone (in this study: *human femur*) and skeletal muscle (in this study: *porcine musculus longissimus*) at tissue level and macro level, analyze their affection by tissue composition and structural properties, provide them as input parameters in their FE simulation model in order to understand their adaption during implants and to give a proper interpretation of clinical techniques.

The specific objectives of bone (human femur) measurements are

a. Develop a new acoustic scanning procedure to determine anisotropic elastic property of cortical bone at tissue level.
b. Analyze the spatial distribution of micro and macro level elastic properties of the entire human femur.
c. Analyze the spatial distribution of structural parameters and the degree of mineralization of entire human femur.
d. Address the relation between structural properties and bone elasticity at micro and mesoscale.

The specific objectives of muscle (porcine musculus longissimus) measurements are

a. Assess anisotropic ultrasonic propagation properties and material properties of single muscle fibers.
b. Determine the acoustic properties of intermediate tissues (skin and fat layers) which lie on a sound propagation path between the transducer and the evaluated muscle tissue in intact carcass ultrasonic measurement to optimize the correction algorithms of backscattered RF signal spectral analysis.
c. Compare ultrasonic parameters estimated at micro and macro level with compositions and structural parameters to find their influence.
d. Develop a method to predict muscle composition and structural parameters by non-destructive ultrasonic measurement.

I.2 Hierarchical structure of musculoskeletal tissues

I.2.1 Cortical bone

I.2.1.1 Cortical bone structure

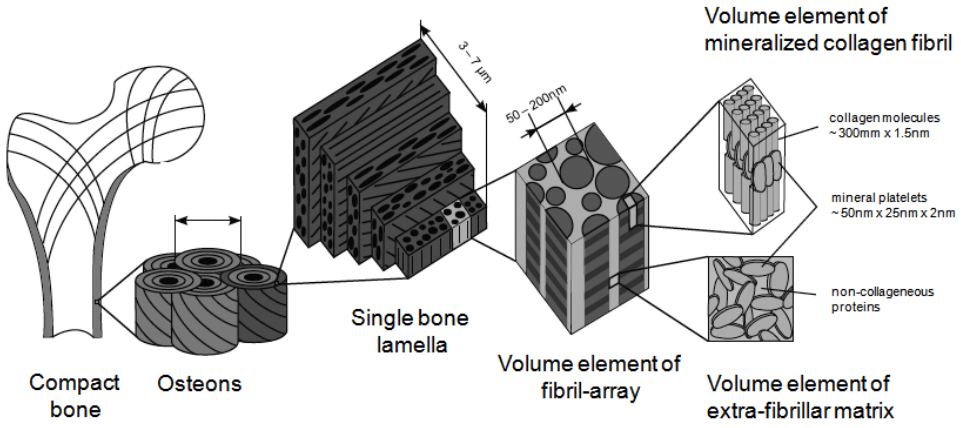

Figure I.1 *Hierarchical structural organization of cortical bone (adapted from [94]).*

Bone is a material arranged in different hierarchical level according to the structural components involved. Structure features on lower levels serve as the building blocks for higher levels. Each hierarchical level contributes to the overall mechanical properties. A detailed classification of the structure hierarchy across the size scales of varying length is shown in Fig. I.1 [94-99].

- Whole bone – contains both cortical and trabecular bone
- Cortical bone – microstructure of cortical bone is composed of regular, cylindrically shaped lamellae (osteons)
- Osteon – building block of the cortical bone, formed by lamellae (made of subsequently rotated sub-lamellae ‘twisted plywood’ assembly) with Haversian channels
- Fibril array – long unidirectional aligned fibrils, bond in an extra fibrillar matrix
- Mineralized collagen fibril – semi crystalline aggregation of collagen molecules
- Major components – mineral crystals, collagen molecules, organic molecules and water

Bone is distinguished into cortical and cancellous types at macroscopic scale. The microstructure of cortical bone is composed of regular, cylindrically shaped units called osteons. Its mechanical properties are influenced greatly by the porosity, the mineralization and the organization of collagen fibrils arrays. It is, therefore, difficult to predict micro-properties *in vivo* by measuring mechanical properties at macrostructural level. In general, values for mechanical properties of bone at macrostructral level vary from one bone to another as well as within different regions of the same bone.

At length scales below several microns, the variety of bone tissue are reduced to different mineralized collagen fibrils arrangements (Fig. I.2). At this level, the effective stiffness properties of bone depend on the properties of the collagen fibril's constituents, their microstructure, and orientation distribution, also the mineral content and the shape of the mineral particles [100]. The main classes of cortical bone are defined as woven bone and lamellar bone. Lamellar bone is a laminated structure similar to plywood [101;102]. Different theories exist as to how these laminates are organized in bone and in other natural occurring tissues. Regardless, the mechanical properties are determined by the arrangement of the lamellae. Osteonal bone, or Haversian bone, has cylindrical lamellae surrounding a central canal, known as the Haversian canal. Haversian and Volkmann's canals form an interconnected network of porosity in cortical bone tissue, serving the purposes of the cardiovascular and nervous systems. Osteons may be considered as fiber reinforcements running along the principal direction of the whole bone. In this sense, the remainder of cortical bone that is not osteonal bone (i.e. the reinforcements) is called interstitial bone. This tissue includes the remnants of old osteons that have been partially remodeled. Finally, a more disordered woven bone structure is formed, which has different mechanical properties from lamellar bone. Woven bone is typically found in young individuals. As time passes, the phenomenon of remodeling transforms this tissue into mature osteonal bone. Whether lamellar or woven, all bone tissue at this hierarchical level is comprised of mineralized collagen fibrils.

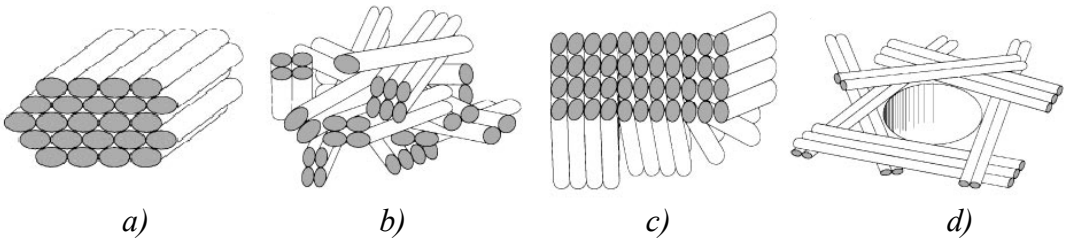

Figure I.2 *Schematic depiction of collagen fibril array observed in different collagen-based tissues. a) Parallel fibril array, b) woven fiber structure, c) plywood like structure and d) radial fibril arrays[98].*

At the nanoscale, bone consists of collagen type I molecules (triple helices of length: ~ 300 nm and diameter: ~ 1.5 nm), self-assembled in a staggered fashion to form collagen fibrils with diameter of ~100 nm [98], hydroxyapatite (HA) minerals, water and noncollagenous proteins (NCPs) like the extrafibrillar proteins that glue together adjacent collagen fibrils [103]. The toughness of bone is determined mainly from a continuous collagen matrix. The organization of the elementary components within the ultrastructure of mineralized tissues has some controversy. This controversy concerns first the distribution of mineral and collagen in the ultrastructure, i.e. the question as to how much mineral is present inside and outside the fibrils. In fact, the ratio of extrafibrillar to intrafibrillar mineral varies from tissue to tissue. Second, the controversy concerns the impact of the organization of the elementary components on the mechanical interaction of collagen and hydroxyapatite in the ultrastructure.

I.2.1.2 Mechanical models for bone

Current experimental techniques in mechanical testing are limited to specific length scales and their usage requires a high amount of effort and resources. Micromechanical modeling of bone tissue is therefore an attractive, complementary method of investigation, which was used in several publications to assess the elastic stiffness properties of bone microstructures.

In the past decade, mechanical models for mineralized collagen fibrils have been developed by several investigators. Akiva et al. [104] calculated the stiffness of a bone lamella made of sub-lamellae using a platelet reinforced composite model. Akkus [105] used micromechanical methods to calculate the elastic stiffness of a mineralized fibril and

investigated the partitioning of applied stresses in the composite and varied mineral content also mineral shape and investigated the impact on the fibril properties. Yoon and Cowin [106] estimated the elastic constants of a single osteonal lamella in a multiscale approach with different micromechanical methods taking the contained water into account. Jaeger and Fratzl [107] and Kotha et al. [108] introduced a 2D model of a mineralized fibril with a staggered mineral platelet arrangement and investigated the influence of changes in geometry and mineralization. Hellmich et al. [21] proposed a continuum-micromechanical model representing collagen-mineral interaction in the elasticity of mineralized tissues as an open mineral foam matrix unidirectionally reinforced by collagen molecule inclusions (Eq.(I.1)).

$$C_{ultra}^{MTI} = \left\{(1-f_{col})c_{foam} + f_{col}:\left[I + P_{col}^{foam}:\left(c_{col}-c_{foam}\right)\right]^{-1}\right\} : \left\{(1-f_{col})I + f_{col}\left[I + P_{col}^{foam}:(c_{col}-c_{foam})\right]^{-1}\right\}^{-1} \quad \text{(I.1)}$$

where c_{col} and c_{foam} are stiffness tensors of collagen and mineral foam matrix. f_{col} is volume fraction of collagen molecules. P_{col}^{foam} is the fourth order tensor characterizing the interaction between the inclusion and the matrix.

Recently, Nikolov and Raabe [100] developed a multiscale micromechanical model that leads from the mineralized fibril level to the fibril-array level. Their fibrils are coated by mineral to account for extra-fibrillar mineralization. Resinger and Pahr [94] investigated the influence of degree of mineralization and collagen stiffness on fibril and fibril-array stiffness using a multiscale continuum micromechanical model. Justin M. Deuerling et al.[109] predicted extracellular matrix elastic constants using the measured orientation distribution function for the hydroxyapatite crystals to average the contribution of misoriented mineralized collagen fibrils.

The macroscopic properties measured by low frequency ultrasound are affected both by the elastic properties of the tissue matrix and by the porous microstructure. Rho et al. [28] also found that the macroscopic modulus of cortical bone can be predicted by a combination of tissue porosity and the tissue "mixture" modulus. Recently, the mechanical properties of cortical bone at mesoscale level has been given particular attention [110-112], in association with novel techniques such as nanoindentation [13] and quantitative scanning acoustic microscopy (SAM) [27;37;113]. These techniques give access to the elastic properties of the

bony matrix mentioned above. Furthermore, SAM and various microscopic imaging techniques give access to the structural distribution of mesoscopic porosity. There is a need for reliable methods to give proper interpretation of acoustic microscope and nanoindentation data in terms of macroscopic elasticity. In particular, phenotyping, the investigation of structure–function relationships and remodeling and numerical modeling of bone response to mechanical loads at various length scales would all benefit from such methods. Mathematical models using homogenization techniques and micromechanical methods can give excellent insight since they explicitly relate the effective properties to the micro/meso structural properties and in the final instance they give relatively accurate predictions of effective moduli.

Several mechanical models proposed in the past two decades provided a great deal of insight into the micro– meso–macro relationships. Recently, Baron et al. [114] and Grimal et al. [110] have developed numerical models to compute the elastic properties of cortical bone with realistic mesoscale structures derived from images. W.J. Parnell and Q. Grimal [115] have developed a new model to determine effective cortical bone elasticity using asymptotic homogenization method by modeling the low frequency elastic wave propagation through an idealized material that models the local mesostructure.

I.2.2 Skeletal muscle

I.2.2.1 Muscle structure

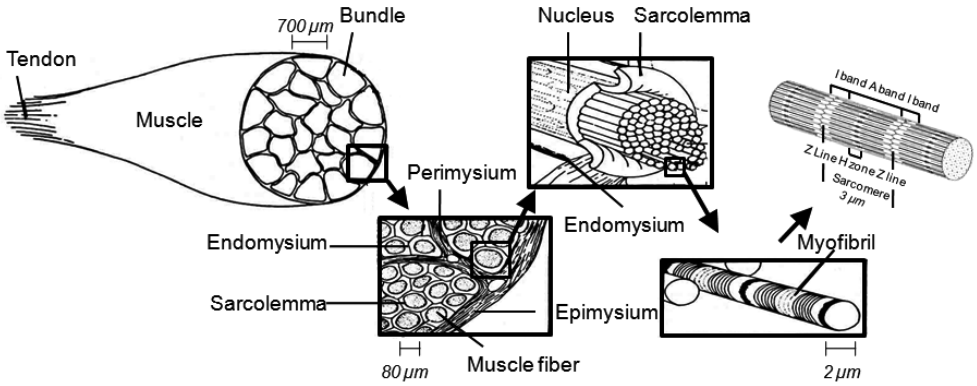

Figure I.3 *Structural organization of skeletal muscle (adapted from www.animal.ufl.edu).*

From the cellular to the whole muscle level, muscles are organized in a hierarchical manner (Fig. I.3).

- Skeletal muscle – consists of thousands of muscle cells, blood vessels, nerve fibers and connective tissue wrappings; covered externally by the epimysium
- Muscle bundle – bundle of muscle fibers surrounded by connective tissue, perimusium
- Muscle fiber – array of myofibrils, stacked lengthwise; surrounded by endomysium
- Myofibril – rod-like contractile element; composed of sarcomeres
- Sarcomere – the contractile unit, composed of myofilaments made up of proteins [116]

Each sarcomere has a band of thick filaments and thin filaments. In the middle of the sarcomere called the A band. They are flanked on both sides by thin filaments. The thin filaments is anchored to the Z line in the I band in one of their end and the other end partially overlaps the thick filaments [51]. Due to the pattern provided by both the filaments, skeletal muscle is also called striated muscle.

The central region of the sarcomere where there is no overlap between those two types of filaments called the H zone. The thick filaments widen slightly at their middle portions, and the widened middle portions of adjacent thick filaments are in register. That is called the M line. The space between overlapping thick and thin filaments is connected by projections called cross bridges from the thick filaments. In a cross section, each thick filament is surrounded by a hexagonal array of six thin filaments and each thin filament is surrounded by a triangular array of three thick filaments (Fig. I.4) [51].

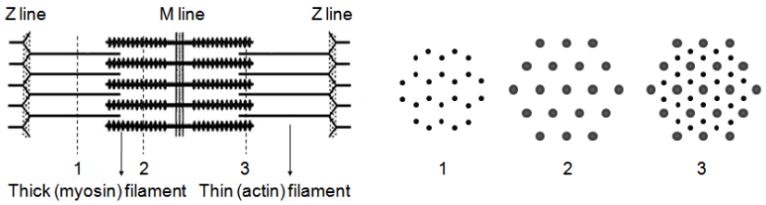

Figure I.4 *One sarcomere (sectioned lengthwise) and lattice like arrangement of thick and thin filaments (1,2,3 cross cut views) (adapted from www.physioweb.med.uvm.edu).*

In skeletal muscle, 80% of the proteins are in the total myofibril content [117]. Myosin and actin are the structural proteins that make up the myofibrils and are responsible for sarcomere contraction in living muscle and rigor mortis in the post-mortem muscle. The primary composite of thick filaments is myosin. The myosin molecule heads form the cross bridges between thick and thin filaments. Thin filaments contain the contractile proteins, actin and other proteins, troponin and tropomyosin. The α-actin is a binding protein found in Z disks. Purified α-actin is a rod shaped molecule which can bundle actin filaments together into parallel arrays. The protein titin run parallel to the thick and thin filamentsin the sarcomere and attaches the thin filaments to the Z disks. These titin filaments are very elastic and hypothesized to act as springs to help keep the thick filaments centered in the Z disks.

The myofibrillar proteins are the main water binding components in the muscle. The polar structure of the water molecules causes it to be attracted by positive and negative charges of muscle protein. The charged and polar side groups of muscle protein tend be on the outside, and in contact with water. Non-polar side groups tend to be on the hydrophobic interior of the protein. Water molecules are bound by the myofilament network. This water holding capacity is changes depending on the muscle pH value which affects the net charge of the myosin molecule. At the isoelectric point of myosin and actin, pH 5.0, where both negative and positive charges are almost equal, the bond between actin and myosin causes the myofilament lattice to shrink and expel water [118].

The lipid has four functions in living animals: membrane structural components, source of energy, protective component and involvement in cellular recognition. Plasma membrane is made up of two molecular layers of lipid (mostly phospholipids) such that the hydrophobic, non-polar, fatty acid tails (fatty acid moieties) are aligned together, leaving the hydrophilic, polar, head groups facing outward. Lipids in adipose tissue contain a large amount of trigulceride (99%). The triglyceride consists of all 3 hydroxyl groups on the glycerol molecule being esterified with a fatty acid chain [87] (smith). Intramuscular fat is responsible for marbling seen in certain cuts of beef [119]. In humans, excess accumulation of fat is associated with insulin resistance and type 2 diabetes.

The acoustic properties of muscle are affected by the muscle compositions percentage of water, fat and protein [87;89;120]. But those compositions vary for different muscle groups. Since each skeletal muscle type has different compositions, it would be no surprise to

find differing acoustic properties. Also, similar tissue types will produce different acoustic parameters depending on whether the muscle is in a diseased state. Based on this information it is important to know the percentage of fat, water, and protein of the skeletal muscle under investigation.

I.2.2.2 Intramuscular connective tissue

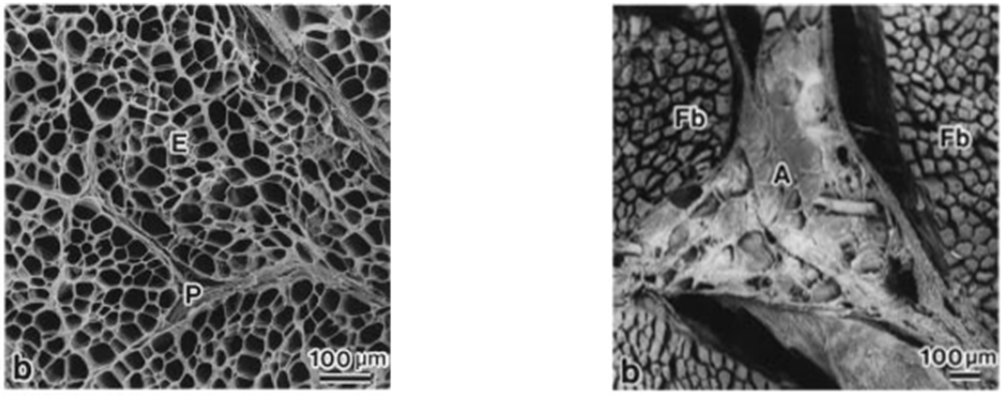

a) *b)*

Figure I.5 *Scanning electron microscope images of intramuscular connective tissue of longissimus muscle. a) The endomysium (E) shows a honeycomb structure, and perimysium (P) consists of several layers of sheets. B) The adipose tissue (A) is observed between muscle fiber bundles during fattening [85].*

Intramuscular fat is deposited inside the perimysium, i.e., between the muscle fiber bundles [85]. During the increase of IMF, the adipose tissues are formed in perimysium (Fig. I.5). At this time, the ribbon like structure is appeared between the endomysium and the connective tissue surrounding fat cells. This s due to disorganizations of perimysium. The disorganization of the perimysium causes the partial breakdown of the honeycomb structure of endomysia, which is bundled by the perimysium [53;54]. Alterations of this structure and mechanical strength affect the homogeneity of the muscle.

I.3 Acoustic Theory

I.3.1 Sound propagation in homogeneous medium

I.3.1.1 Sound propagation

In the following section the theoretical background of acoustic wave propagation in homogeneous, non-attenuated medium is considered. Sound propagation through a medium creates periodic changes in pressure, density and temperature as a function of time. The general wave equation describes the propagation of wave in a non attenuated medium. For the pressure variation:

$$\nabla^2 p = \frac{1}{v^2}\frac{\partial^2 p}{\partial t^2}, \tag{I.2}$$

where $p(x,t)$ is excess pressure as a function of distance and time and v is the speed of sound. This deviation is developed from the continuity equation and the equation of motion. Changes in density related to changes in pressure are described by the equation of state:

$$p = \rho_e v^2, \tag{I.3}$$

where ρ_e is the excess density. The pressure changes are related to a change in particle displacement through the equation of motion:

$$\rho_0 \frac{\partial u}{\partial t} = -\nabla p, \tag{I.4}$$

where $\rho_0$is the equilibrium density, $\vec{u} = u_x\hat{x} + u_y\hat{y} + u_z\hat{z}$ is the particle displacement velocity and ∇ is the divergence operator. The continuity equation is based on the conservation of mass and describes the motion of particle which produces a change in density

$$\frac{\partial s}{\partial t} + \nabla \cdot u = 0 \tag{I.5}$$

where $s = \rho_e/\rho$ is the fractional increase in the density.

I.3.1.2 Transmission and Reflection

The behavior of acoustic waves at the interface between two isotropic media can be described by the laws of ray optics. The reflection and transmission of acoustic wave incident on a planar interface are described with the help of a specific medium parameter called acoustic impedance Z [121]. The impedance is the product of the density ρ of a medium and the velocity v of a given wave propagating in it. The unit of impedance is rayl [1 rayl=1 $kgm^{-2}s^{-1}$]:

$$Z = \rho v . \tag{I.6}$$

If the acoustic wave is incident perpendicular to the planar boundary between the mediums having the impedance values Z_1 and Z_2, then the reflection and transmission coefficients are described as:

$$R = \frac{Z_2 - Z_1}{Z_2 + Z_1}, \tag{I.7}$$

$$T = \frac{2Z_2}{Z_2 + Z_1}. \tag{I.8}$$

If the wave is not perpendicular to the boundary, each refracted ray obeys Snell's law. This law may alternatively be expressed as the requirement that the tangential components of the wave vector be conserved across a boundary, so that $k_1 \sin\theta_1 = k_1 \sin\theta_2$ [121]. The acoustic normal impedance at the boundary is:

$$Z = \frac{\rho v}{\cos\theta}. \tag{I.9}$$

When the acoustic wave is travelling from fluid to solid medium, the incident wave will generate a reflected wave in the fluid and in the solid a longitudinal wave (l) and a shear wave (s). The reflection and transmission coefficients for this case:

$$R(\theta) = \frac{Z_l \cos^2 2\theta_s + Z_s \sin^2 2\theta_s - Z}{Z_l \cos^2 2\theta_s + Z_s \sin^2 2\theta_s + Z}, \tag{I.10}$$

$$T_l(\theta) = \frac{2Z_l \cos^2 2\theta_s}{Z_l \cos^2 2\theta_s + Z_s \sin^2 2\theta_s + Z}, \tag{I.11}$$

$$T_s(\theta) = \frac{-2Z_s \cos^2 2\theta_s}{Z_l \cos^2 2\theta_s + Z_s \sin^2 2\theta_s + Z}. \tag{I.12}$$

Under the condition of normal incidence, the shear waves are not generated and the reflection coefficient is reduced to Eq. (I.7)

I.3.1.3 Theory of Anisotropy

The material which has different physical properties at different directions is anisotropic materials, such as bone, muscle and wood. The constitutive equation for such a material is the conventional form of Hook's law,

$$\sigma_i = c_{ij}\, \varepsilon_j \,. \tag{I.13}$$

where σ_i and ε_j are the stress and strain tensor. i and j indicate the orthogonal direction of the coordinates ($i, j = 1,2,3$). $C(c_{ij})$ is the elastic coefficient matrix. The stiffness matrix [C] of a transverse isotropic material in the standard abbreviated subscript notation has the form:

$$[C] = \begin{bmatrix} c_{11} & c_{12} & c_{13} & 0 & 0 & 0 \\ c_{12} & c_{11} & c_{13} & 0 & 0 & 0 \\ c_{13} & c_{13} & c_{33} & 0 & 0 & 0 \\ 0 & 0 & 0 & c_{44} & 0 & 0 \\ 0 & 0 & 0 & 0 & c_{44} & 0 \\ 0 & 0 & 0 & 0 & 0 & (c_{11} - c_{12})/2 \end{bmatrix}. \tag{I.14}$$

Stress – strain relations can also be expressed in terms of the compliance tensor S such that, $\varepsilon_i = s_{ij}\sigma_j$ where the compliance tensor is the inverse of the stiffness tensor. For anisotropic material, the compliance and stiffness tensors are related to the material properties of Young's modulus E, Poisson's ratio γ, and the shear modulus G. The compliance tensor of a transverse isotropic material is:

$$[S] = \begin{bmatrix} 1/E_1 & -\gamma_{12}/E_1 & -\gamma_{31}/E_3 & 0 & 0 & 0 \\ -\gamma_{12}/E_1 & 1/E_1 & -\gamma_{31}/E_3 & 0 & 0 & 0 \\ -\gamma_{13}/E_1 & -\gamma_{13}/E_1 & 1/E_3 & 0 & 0 & 0 \\ 0 & 0 & 0 & 1/G_{13} & 0 & 0 \\ 0 & 0 & 0 & 0 & 1/G_{13} & 0 \\ 0 & 0 & 0 & 0 & 0 & [2(1+\gamma_{12})]/E_1 \end{bmatrix}. \tag{(I.15}$$

The indices 1 and 3 denote the directions perpendicular (*x* direction) and parallel (*z* direction) to the long axis of the femur. The calculation of a sound wave scattering at plane boundaries has been described in [122]. The impedance measured normal to the boundary Z^n can be described in terms of traction force T_{in} and particle velocities v_j,

$$-T_{in} = (Z^n)_{ij}\, v_j \qquad i,j = x,y,z \tag{I.16}$$

where $\hat{n}$ is the direction in which the impedance is measured. Eq.(I.16) can be written in matrix notation:

$$-T_{in} = \frac{n_{iK} c_{KL} k_{Lj}}{\omega}\, v_j, \tag{I.17}$$

where

$$n_{iK} = \begin{bmatrix} n_x & 0 & 0 & 0 & n_z & n_y \\ 0 & n_y & 0 & n_y & 0 & n_x \\ 0 & 0 & n_z & n_y & n_x & 0 \end{bmatrix}, \tag{I.18}$$

and

$$k_{Lj} = \begin{bmatrix} k_x & 0 & 0 \\ 0 & k_y & 0 \\ 0 & 0 & k_z \\ 0 & k_z & k_y \\ k_z & 0 & k_x \\ k_y & k_x & 0 \end{bmatrix}. \tag{I.19}$$

The acoustic impedance matrix elements for the direction $\hat{n}$ are:

$$(Z^n)_{ij} = \frac{n_{iK} c_{KL} k_{Lj}}{\omega}, \tag{I.20}$$

where c_{KL} are the components of the stiffness tensor [*C*] and $\omega = 2\pi f$ is the radian frequency. The impedance coefficients in symmetry directions *x* and *z* are:

$$\omega(Z^n)_{xx} = c_{11}n_x k_x + c_{66}n_y k_y + c_{55}n_z k_z + c_{56}(n_y k_z + k_y n_z) + c_{15}(n_z k_x + k_z n_x) + c_{16}(n_x k_y + k_x n_y) \tag{I.21}$$

$$\omega(Z^n)_{zz} = c_{55}n_xk_x + c_{55}n_yk_y + c_{33}n_zk_z + c_{34}(n_yk_z + k_yn_z) + c_{35}(n_zk_x + k_zn_x) + c_{45}(n_xk_y + k_xn_y) \quad \text{(I.22)}$$

For a compressional wave propagation in the *x*-direction $k_x = \frac{\omega}{v_{Px}}$, $k_y = k_z = 0$, $n_x = 1, n_y = n_z = 0$. v_{Px} is the phase velocity of the longitudinal wave. Therefore Eq. (I.21) becomes

$$\omega(Z^n)_{zz} = c_{11}k_x, \quad \text{(I.23)}$$

which can be written in the form:

$$(Z^n)_{xx} = \sqrt{c_{11}.\rho} \quad \text{(I.24)}$$

Similarly, the impedance for a compressional wave propagating in the z- direction is:

$$(Z^n)_{zz} = \sqrt{c_{33}.\rho}, \quad \text{(I.25)}$$

Eq. (I.24) and Eq. (I.25) show that if the wave propagation direction and particle displacement are normal to the interface and the propagation direction is parallel to the direction *i*, the acoustic impedance normal to the surface $(Z^n)_{ii}$ is directly proportional to the elastic coefficient c_{ii} and the mass density ρ. Eq. (I.21) and Eq. (I.22) are valid for the general anisotropic case. Therefore, the impedance for the propagation not parallel to the elastic symmetry axes can easily be obtained by rotation of the elastic stiffness tensor [122]. For the transverse isotropic case, rotation in the *xz* plane yields [123]:

$$c(\theta) = c_{33}cos^4\theta + 2(c_{13} + 2c_{44})sin^2\theta cos^2\theta + c_{11}sin^4\theta. \quad \text{(I.26)}$$

where θ is the rotation angle. It can be seen that $c(0^o) = c_{33}$ and $c(90^o) = c_{11}$. Combining Eq. (I.25) with Eq. (I.26) gives

$$(Z^n)_\theta = \sqrt{c(\theta).\rho}\ . \quad \text{(I.27)}$$

I.3.2 Sound propagation in an inhomogeneous medium

In consideration of sound propagation in real media, it is necessary to start from inhomogeneous, attenuating media. Attenuation is the result of conversion of sound energy by absorption and scattering. The following section describes the mechanisms of absorption and scattering.

I.3.2.1 Scattering

The scattering of sound waves is the redirection of sound that takes place when waves encounter an obstacle (scattering particle) or non-homogeneity. It can be defined as changes of amplitude, frequency, phase velocity or the direction of propagation as the result of an obstacle in the medium. The basic concept introduces the scattered pressure wave composed of the actual pressure wave minus the undisturbed wave [124-126]. The shape and intensity of scattered field depends mainly on the shape of the scatterer, its compressibility and density as well as it physical expansion. For large particles $ka \gg 1$ compared with the wavelength, sound is considered to be reflected and diffracted rather than scattered as shown in section (I.3.1.2). The concept of scattering in the narrow sense refers to cases where $ka \approx 1$ (Mie scattering) or $ka \ll 1$ (Rayleigh scattering). Often, the ratio of total diffuse power D_{str} to the intensity of incident wave I_0 called effective scattering cross section σ_{eff} is used as a measure for the characterization.

For the case $kr \gg 1$ (large distance to the observation point r) and $ka \ll 1$ (Rayleigh scattering), the scattered wave intensity at a scattering particle is:

$$I_{Rayleigh} = I_0 \frac{\omega^4 a^6}{9v^4 r^2}\left(\frac{\kappa_1 - \kappa_2}{\kappa_1} + 3\frac{\rho_2 - \rho_1}{2\rho_2 + \rho_1}cos\theta\right)^2. \tag{I.28}$$

The scattered intensity is proportional to the fourth power of the frequency and the sixth power of radius of the particle. The κ_i compressibility and the densities ρ_i only influence the angle at which the scattering is zero. The effective scattering cross section is:

$$\sigma_{eff} = \frac{4\pi\omega^4 a^6}{9v^4 r^2}\left(\left|\frac{\kappa_1 - \kappa_2}{\kappa_1}\right|^2 + \frac{1}{3}\left|\frac{3\rho_2 - 3\rho_1}{2\rho_2 + \rho_1}\right|^2\right). \tag{I.29}$$

For the case $ka \ll 1$, σ_{eff} is only a fraction of the scatterer cross-sectional area. For the case $ka = 1$, which corresponds to Mie scattering, leads to complicated results. The simplest solution is obtained for the case of a non-compressible particle (κ infinite) for $ka \gg 1$ and $kr \gg 1$ [127]:

$$I_{Mie} = I_0 \frac{a^2}{4r^2}\left(1 + cot\frac{\theta}{2} J_1^2(ka\, sin\theta)\right) , \tag{I.30}$$

where $J_1$is the Bessel function of first order. In contrast to Rayleigh scattering, here the frequency dependence is given by a complicated form in the square of the Bessel function. Also the scattering parameter ka has a different effect on the shape of the scattering field.

I.3.2.2 Absorption

While sound is propagating through a medium, wave is attenuated by converting some of the sound wave into heat. Absorption is the result of various physical phenomena that occur in the propagation of ultrasonic waves in a real attenuating medium. The weakening of the wave by absorption increases with propagation length, shown in Eq. (I.31) based on the intensity:

$$I = I_0 e^{-\alpha x} , \tag{I.31}$$

where α is the absorption coefficient and I is the intensity. The main absorption mechanisms are viscous losses, heat conduction and relaxation processes. In fluids, resistance to sound wave penetration is called viscosity.

$$\alpha = \frac{\omega}{v}\frac{1}{\sqrt{2}}\sqrt{\frac{\sqrt{1 + (\omega\tau)^2} - 1}{1 + (\omega\tau)^2}}, \tag{I.32}$$

where α refers to the viscous losses caused by absorption and τ the relaxation time. Another mechanism of absorption is caused by heat. The classical absorption coefficient is composed of two derivatives developed by Stokes and Kirchoff including the viscous and thermal conductivity losses of the media.

$$\alpha_{classical} = \frac{\omega^2}{2\rho_0 v^3}\left[\frac{4}{3}\eta + (\gamma - 1)\frac{\kappa}{c_p}\right], \quad \text{(I.33)}$$

where η is the shear viscosity, the heat capacity of κ and γ is the ratio of the specific heat capacity at constant pressure c_p and constant volume c_V. The bulk of the energy conversions are caused by chemical, thermal and structural absorption mechanisms. These are also known as bulk viscosity [128].

I.3.3 Sound propagation in biological tissue

Ultrasonic wave propagating through biological tissue is affected by tissue structures that have a varying compressibility and density at different length scales. The amplitude of the original sinnal becomes attenuated as the depth of penetration increases. Attenuation in the biological tissue is due to absorption, reflection and scattering at interfaces between tissue layers.

I.3.3.1 Reflection

Reflection in biological tissue is predicted by the difference in acoustic impedance of the various tissue types at the interface (i.e., the degree of impedance mismatch). The higher the degree of acoustic impedance mismatch is greater the amount of reflection. Due to extremely lower acoustic impedance of air relative to biological tissues, the degree of reflection is high at the air/tissue interface. For this reason, it is important to apply conducting gel (an acoustic coupling medium) on surface of transducer to eliminate any air pockets between the transducer and the skin surface. Otherwise most of the ultrasound waves will be reflected limiting tissue penetration.

I.3.3.2 Scattering

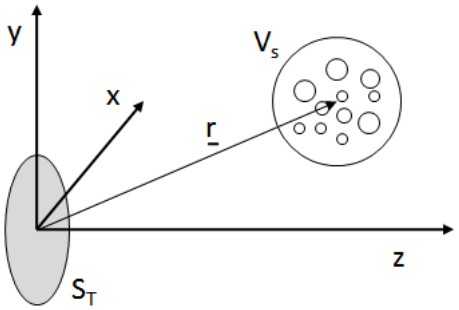

Figure I.6 *Scattering geometry showing the transducer active surface S_T and the volume V_s enclosing the scatterers [129].*

More information about the physical properties of tissue used in diagnostic ultrasound originates from scattering processes. Tissue identification and clinical diagnosis are routinely performed by the observation of scattered ultrasound. Due to the relevance of the scattering processes to the echo and transmission imaging techniques, nowadays research in ultrasonic tissue characterization aims at describing tissue microstructure through the analysis of the backscattered signal. The theory behind the scattering process in the biological tissue is explained below. For sound propagation through typical tissues without hard inclusions, the variations $\Delta\rho$ and $\Delta\kappa$ in density ρ and compressibility κ are small around mean values ρ_0 and κ_0 with relative variation γ_ρ and γ_κ:

$$\begin{aligned} \kappa &= \kappa_0 + \Delta\kappa \\ \rho &= \rho_0 + \Delta\rho \\ \gamma_\kappa &= \Delta\kappa/\kappa_0 \\ \gamma_\rho &= \Delta\rho/\rho_0. \end{aligned} \tag{I.34}$$

In this case, sound propagation can be described by the wave equation for inhomogeneous media for pressure variation $p(\underline{r},t)$ at point $\underline{r}$ and time t [124]:

$$\nabla^2 p - \frac{1}{c_0^2}\frac{\partial^2 p}{\partial t^2} = \frac{1}{c_0^2}\frac{\partial^2 p}{\partial t^2}\gamma_\kappa(\underline{r},t) + \nabla\gamma_\rho(\underline{r},t)\,.\,\nabla p\,. \tag{I.35}$$

With the first Born approximation, the wave equation for the Fourier transformed pressures $P_i(\underline{r}, t)$ and $P_s(\underline{r}, t)$ can be expressed as (where i –incident wave and s - scattered wave):

$$\nabla^2 P_s + k^2 P_s = -k^2 \gamma_k(\underline{r}) P_i + \nabla \gamma_\rho(\underline{r}) \,.\, \nabla P_i \,. \tag{I.36}$$

The solution can be found by the volume integral over a volume Vs containing all contributing scatterers (Fig. I.6):

$$P_s(\underline{r}, \omega) = \int_{V_s} k^2 \gamma_k(\underline{\tilde{r}}) P_i(\underline{\tilde{r}}, \omega) g(\underline{r}|\underline{\tilde{r}}, \omega) + \gamma_\rho \nabla P_i(\underline{\tilde{r}}, \omega) \,.\, \nabla g(\underline{r}|\underline{\tilde{r}}, \omega) d^3\underline{\tilde{r}}, \tag{I.37}$$

where $g(\underline{r}|\underline{\tilde{r}}, \omega)$ is the three dimensional free space Green's function and the gradient operator is with respect to $\underline{\tilde{r}}$. When the observation point is far away from the scattering volume Vs, the approximation:

$$\nabla g(\underline{r}|\underline{\tilde{r}}, \omega) \approx -j\underline{k_s} g(\underline{r}|\underline{\tilde{r}}, \omega), \tag{I.38}$$

holds, where $\underline{k_s}$ points in the direction of $\underline{r} - \underline{\tilde{r}}$, i.e., from the scatterers to the observation point and $\left|\underline{k_s}\right| = k$. When the scattering volume is further away than the transducer radius, the incident wave can be approximated locally by a plane wave and:

$$\nabla P_i(\underline{r}, \omega) \approx -j\underline{k_i} P_i(\underline{r}, \omega), \tag{I.39}$$

can be used. Here k_i is the wave vector of the incident field with magnitude k. In this case the solution can be simplified further to

$$P_s(\underline{r}, \omega) = \frac{k^2}{4\pi} \int_{V_s} \gamma_{k\rho}(\underline{\tilde{r}}) P_i(\underline{\tilde{r}}, \omega) \frac{\exp(jk|\underline{r} - \underline{\tilde{r}}|)}{|\underline{r} - \underline{\tilde{r}}|} \, d^3\underline{\tilde{r}}, \tag{I.40}$$

with the joint inhomogeneity function

$$\gamma_{k\rho}(\underline{\tilde{r}}) = (\gamma_k(\underline{\tilde{r}}) + \gamma_\rho(\underline{\tilde{r}}) \frac{\underline{k_i} \,.\, \underline{k_s}}{k^2}). \tag{I.41}$$

Many different models have been proposed in order to extract statistically averaged information from the backscattered radio frequency signals measured within a distinct tissue volume. In recent years, the microstructural tissue features have been successfully derived by

fitting the measured backscatter spectrum to a theoretical backscatter model that uses form factors [92;93]. Form factors (FF) are functions that approximate the backscatter characteristics of a single scattering structure according to geometry and elastic properties of the scatter and the surrounding medium [93]. The backscattered ultrasound signal from tissue can then be modeled by the superposition of scattered waves (approximated by the FF) from scatterers with a specific size, shape and distribution [92;93;130;131]. Commonly used form factors for biological tissues are the Gaussian, the fluid sphere, and the spherical shell, all describing spherically symmetric shapes [132]. For example, the theoretical power spectrum of an ensemble of Gaussian scatterers has a closed form solution

$$W_{theor}(k) = \left(\frac{a_{eff}^6 n z_{rel}^2}{36\pi^4}\right) e^{-0.827k^2 a_{eff}^6} \tag{I.42}$$

where a_{eff} is the average scatter radius and $nz_{rel}^2$is the scatter concentration. Many biological structures are anisotropic in terms of structure and elastic properties, form factors can be easily changes according to that.

I.3.3.3 Absorption

Attenuation of tissue is caused by scattering and absorption. The exact relaxation processes responsible for absorption in tissue are difficult to model. For this reason attenuation in tissue is measured and a parametric model is fitted to the data. To take absorption in biological tissue into account, wave equation (I.37) must be solved for a frequency-dependent complex compressibility$\kappa(\omega) = \kappa'(\omega) - \kappa''(\omega)$. However, the imaginary part of the wave vector due to attenuation is small in comparison to the real part, allowing the attenuation to be handled as a small perturbation.

For the homogeneous wave equation in an absorbing medium for a wave propagating in positive z direction, the solution is:

$$P(\omega, z) = P_0 \exp(-jkz - \alpha(\omega) - j\beta_{min}(\omega)), \tag{I.43}$$

with $\alpha(\omega)$ describing the frequency dependent attenuation and $\beta_{min}(\omega)$ representing the phase caused by the dispersive attenuation due to the Kramers-Kronig relation:

$$\beta_{min}(\omega) = \frac{1}{\pi} \int_{-\infty}^{+\infty} \frac{\alpha(\tilde{\omega})}{\tilde{\omega}^2 - \omega^2} d\,\tilde{\omega}\,. \tag{I.44}$$

In biological tissues α is small in comparison to kz. Therefore, absorption can be written for in the received voltage signal by multiplying with the attenuation term $\exp(-2\alpha(\omega)z)$ corresponding to the depth z in which the factor of 2 accounts for the signal being attenuated on the way to the scatter and back to the transducer.

As the attenuation coefficient $\alpha(\omega)$ is usually not derived analytically but can only be measured, different models exist to characterize the frequency dependence of tissue. For a wide range of ultrasound frequency a power function can be fitted to $\alpha(\omega)$:

$$\alpha(\omega) = \alpha_\nu \left|\frac{\omega}{2\pi}\right|^\nu . \tag{I.45}$$

While for water ν is two, in biological tissues ν is mainly in the range from 1 to 1.5. When the bandwidth of the ultrasonic system is not too large, the power law is often approximated by a linear relationship in the investigated frequency interval around a center frequency ω_c.

$$\alpha(\omega) = \alpha_1 \frac{\omega - \omega_c}{2\pi} + \alpha_0 . \tag{I.46}$$

In the above sections, the theory behind the sound propagation along homogeneous, inhomogeneous and biological tissue was explained. The wave propagation along biological tissue depends on their structures and compositions. Acoustic properties of some of tissues are summarized in

Table I.1 *Acoustic properties of some of biological tissues from the literatures [133-135]*

Tissue	Speed of sound [m/s]	Density [kg/cm^3]	Attenuation [dB/MHz/cm]	Impedance [Mrayl]
Water (37°C)	1523	0.994	0.002	1.52
Fat	1473	0.920	0.63	1.34
Muscle	1580	1.070	1.3	1.71
Liver	1550	1.060	0.94	1.65
Brain	1562	1.030	2.5	1.66
Bone	4080	1.810	15.0	7.8

II Materials and Methods

II.1 Complementary methods

II.1.1 Synchrotron radiation - µCT

The most important clinical measure for the diagnosis of metabolic bone changes and the quantitative evaluation of fracture risk is the so-called bone mineral density (BMD) [136]. However, the bone strength does not only depend on mineral density; microarchitectural properties play a major role in it [137;138]. Boivin and Meunier [139] assessed the degree of mineralization of bone (DMB) which in addition to the amount of bone tissue and microarchitectural organization, presumably determines bone strength using quantitative microradiography. The evaluation of DMB was shown to be interesting for precise understanding of the therapeutic action of agents for bone diseases. In particular, synchrotron radiation micro computed tomography (SR-µCT) provides 3D images with spatial resolution of one micron. Moreover, the use of a monoenergetic synchrotron beam which averts beam-hardening effects allows quantitative measurements of the DMB of bone samples. Indeed, the reconstructed gray values of tomographic images correspond directly to a map of the linear attenuation coefficient within the sample [140]. Since the absorption depends on the amount of mineral content (i.e. hydroxyapatite (HA)), a calibration method (Eq. (II.1)) using homogenous water solutions of different concentration of dipotassium hydrogen phosphate (K_2HPO_4), often employed for replacing HA in the medical routine was proposed to evaluate the three-dimensional distribution of the degree of mineralization within the sample [10].

$$\mu(E)_{water,salt} = [A_E + (\alpha - 1).B_E].c + B_E\rho_{water} \quad \text{(II.1)}$$

where $\mu(E)_{water,salt}$ is linear attenuation coefficient of the solution. A_E and B_E are mass attenuation coefficients of salt and water respectively and $\boldsymbol{c}$ is concentration of salt.

II.1.2 Histology

In biology and medicine, histology has been used for several years to visualize or differentially identify microscopic structures through the use of histological stains. It is performed by examining a thin slice of tissue under a light microscope or electron microscope. Skeletal muscle has three types of fiber depending on their functional properties, e.g., force of contraction, velocity of shortening and endurance [141]. They are: slow twitch oxidative (STO) with high endurance to fatigue, fast twitch oxidative (FTO) also enduring but with greater metabolic diversity and fast twitch glycolytic (FTG) with limited endurance but quick response. All these functional properties vary according to molecular and cellular differences between myofibers. The muscle fiber shortening speed will depend upon the speed of the molecular interactions between actin and myocin, and this depends upon the ATPase in the myosin molecules. The fatigability of a myofiber depends upon its ability to produce quantities of ATP rapidly enough to supply the contractile demand. ATP can be produced slowly and continuously by oxidative means, or rapidly for short periods by glycolysis. To differentiate between those functional property dependent muscle fibers, modified ATPase/NADH-TR staining is performed [142]. Depending on the types of ATPase and metabolic enzymes existing in muscle fibers, this type of staining shows various colors (Fig. II.1).

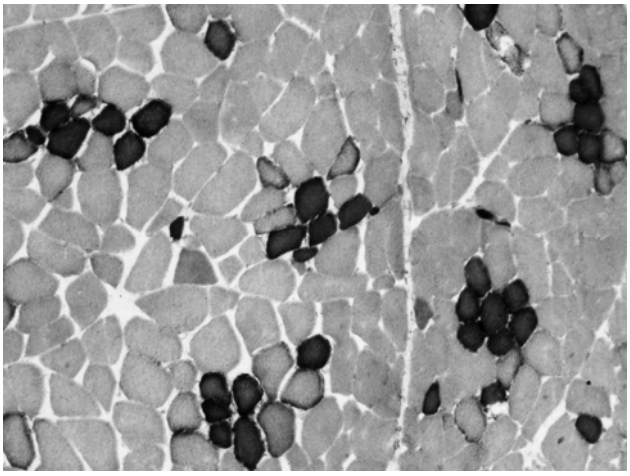

Figure II.1 *ATPase/NADH-TR stained histology. The dark gray corresponds to STO, intermediate gray to FTO and light gray to FTG. The white is from connective tissue.*

II.1.3 Chemical analysis

The muscle constituents e.g., water, protein and fat were determined by chemical analysis. Depending on the physical and chemical properties of individual constituents, different chemical analysis techniques were performed. In this study, meat quality trait related chemical parameters were focused on, such as dry matter, intramuscular fat, protein and drip loss. All these parameters were determined using standard procedure accordance to German Food Legislation [143]. Dry matter is the measurement of mass of tissue when completely dried using sea sand (Eq. (II.2)). After removing the dry matter amount from the raw muscle tissue mass, the remaining mass corresponds to amount of water content.

$$dry\ matter\ \% = \frac{sample\ weight\ after\ dried}{sample\ weight\ before\ dried} x\ 100 \quad \text{(II.2)}$$

The amount of intramuscular fat is determined by ether extraction. First, the sample is pre-treated with HCL and filtered. The filtrate is extracted with petroleum ether using a Soxtherm-apparatus [87]. The loss in weight of the sample is the ether extracted material or intramuscular fat %. Protein content is determined by oxidative digestion. Drip loss is measured using the EZ drip-loss method [144]. For this, samples were stored in plastic containers for 48 H at 4°C. Drip loss is given as the percentage amount of the weight lost compared to the weight of the sample before storage. All these chemical parameter were determined from homogenized samples.

II.2 Scanning acoustic microscopy principle

The main hardware components of the scanning acoustic microscope (SAM) are shown in the diagram (Fig. II.2): a three-axis high-precision scanning stage, a 200- MHz pulser/receiver (Panametrics 5900PR, Waltham, MA), spherically focused transducer (V605/60°: Valpey Fisher, Hopkinton, MA; V611: Valpey Fisher, Hopkinton, MA; V311: PANAMETRICS, Waltham, USA) and a PC containing two A/D-cards (8 bit AD-card CS8500 and 12 bit AD-card CS12400 , Gage Applied Technologies, Inc., Lachine, Mon, Canada). All components are controlled by custom software (SAM200; Q-BAM, Halle, Germany).

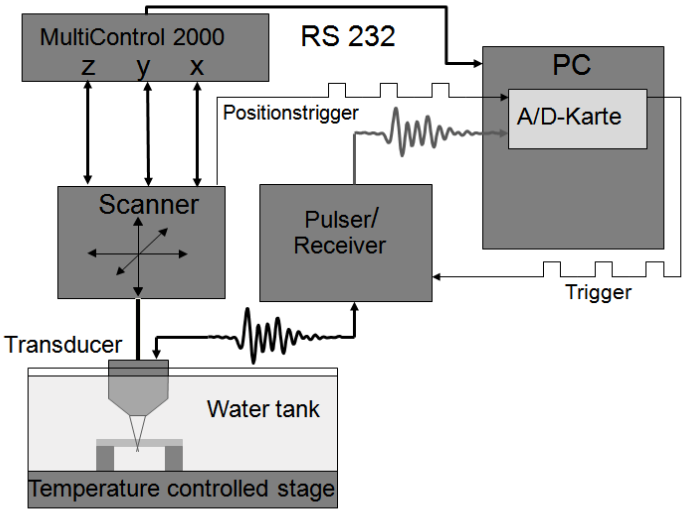

Figure II.2 *Block diagram of scanning acoustic microscope [128].*

The samples were completely immersed in a temperature controlled tank filled with distilled, degassed coupling fluid at desired temperature. The transducer focal plane was placed on the sample surface or inside the sample depended upon the acoustic parameter estimation. Finally, the C-scans were acquired with desired increment along the X and Y directions depending on the transducer beam resolution, whereas for each scanned point, the entire pulse-echo signal was stored.

The lateral resolution of spherically focused transducer, $D_{lateral}$ with numerical aperture *(N.A. = a/ROC)* is determined by the -6 dB transmit-receive beam width in the focal plane (Fig. II.3).

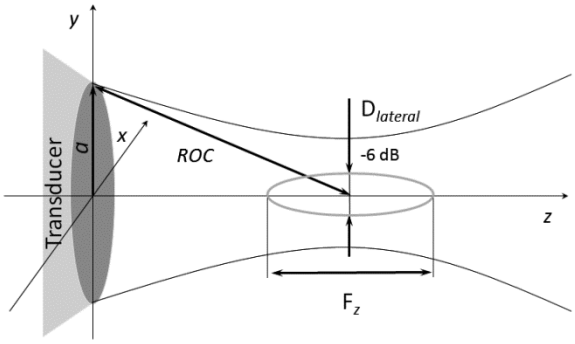

Figure II.3 *Sound field distribution of spherically focused transducer [128].*

$$D_{lateral} = 1.028\,\lambda\frac{ROC}{2a} \tag{II.3}$$

where, λ is the acoustic wavelength, *ROC* is the transducer's radius of curvature and *a* is the radius of the transducer, respectively.

The depth of focus F_z, is the distance between points along the beam axis where the intensity is 3 dB less compared to the focal point is:

$$F_z = 7.08\,\lambda\left(\frac{ROC}{2a}\right)^2 \tag{II.4}$$

The pulse-echo sound field characteristics were determined by the wire technique [145] and are summarized for all spherically focused transducers used in this study in Table II.***1***.

For spherically focused sound fields the condition of plane wave propagation can be approximated in the focal point [25;146]. At this point the incoming waves from the transducer are in phase and all shear wave components are diminished. Therefore, if the boundary between a liquid and an anisotropic material is placed in the focal plane normal to the sound beam axis, the acoustic impedance in the direction normal to the boundary is determined by Eq. (I.27) and the reflection coefficient becomes:

$$R = \frac{Z_1 - Z_0}{Z_1 + Z_0} \tag{II.5}$$

where Z_0 and Z_1 are the acoustic impedance of liquid and anisotropic material respectively. Eq. (II.5) shows that the acoustic impedance can be calculated from confocal reflection amplitude measured with acoustic scanning system.

Table II.1 *Pulse echo beam parameters [128;147].*

Manufacturer Model	Valpey Fisher V605/60 (50 MHz)	Valpey Fisher V611 (100 MHz)	PANAMETRICS V311 (10 MHz)
Medium	Water	PBS	PBS
Temperature	25	36	36
Pulse duration ($\tau_{(-20\ dB)}$)	46.0 ns	35.0 ns	110 ns
Center frequency	44.9 MHz	74.0 MHz	10.6 MHz
f_1 (-6 dB)	26.0 MHz	35.0 MHz	6.8 MHz
f_2 (-6 dB)	63.9 MHz	113.0 MHz	14.5 MHz
Depth of focus (-6 dB)	169 µm	89.75 µm	14420 µm
Confocal beam diameter (-6 dB)	23 µm	20.2 µm	640 µm

II.3 Cortical Bone

II.3.1 Sample preparation

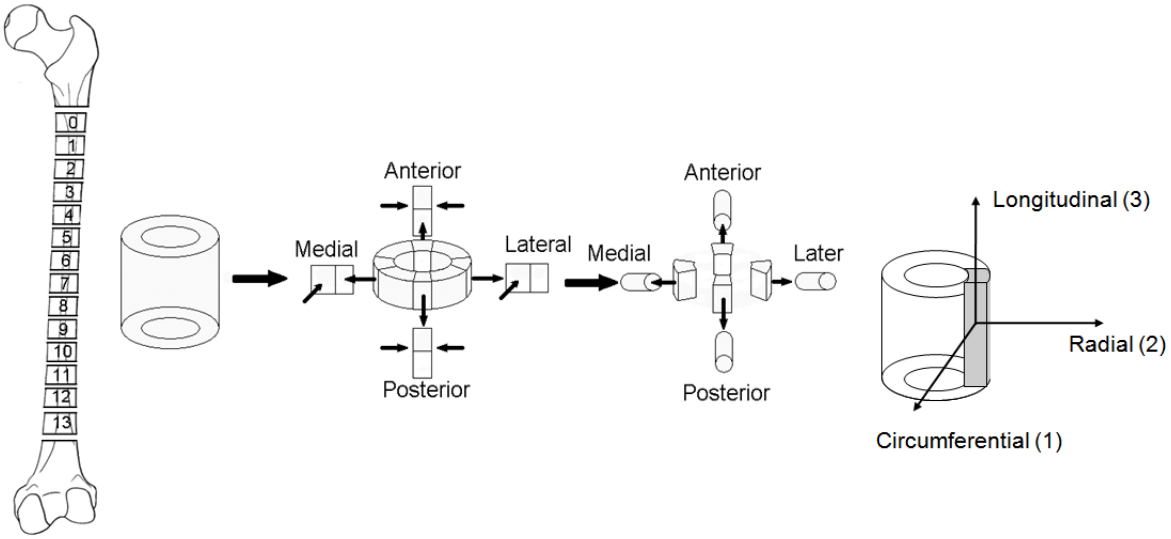

Figure II.4 *Schematic overview of cortical bone sample preparation from femur segments and orthogonal coordinate system for cortical bone [148].*

The shaft of one human femur (female, 72 years) was divided into 14 cross sections from proximal to distal of thickness approximately 22 mm with a diamond saw (Exakt – Trennschleifsystem Makro, Exakt Apparatebau, Norderstedt, Germany). Section 1 corresponds to the section closest to the hip and section 14 to the section closest to the knee. All sections were fixed and dehydrated in a graded series of ethanol (70%, 96% and 100% ETOH, immersion for 24 hours in each solution) and embedded in polymethylmethacrylate (PMMA) [148]. This procedure ensured that the water content was completely replaced by the embedding material. Then the discs were further divided into four parts from posterior, medial, anterior and lateral sections. To estimate complete anisotropic properties of cortical bone, cylindrically shaped samples with a diameter of 4.4 mm and its orientation of the long axis parallel to the radial axis of the femur shaft were drilled from all sections using a high precision lathe equipped with a diamond milling knife (Fig. II.4). The final surface smoothness was obtained by grinding with successively decreasing grain size (SiC paper #2400 and #4000; Struers GmbH, Willich, Germany).

II.3.2 Microscopic elastic properties estimation

II.3.2.1 Data acquisition

Before preparing cylindrical samples, all the cross sectional and traverse sectional samples were scanned with scanning acoustic microscope. In this case, the SAM described in (Sec. II.2) was equipped with spherically focused 50 MHz transducer (V605/60°, Valpey Fisher, Hopkinton, USA). The -6 dB pulse-echo field of the transducer was determined by measuring the scattered signal from a 10-µm diameter tungsten wire reflector translated throughout the focal region [145]. The sound field characteristics of the transducer are summarized in Table II.1.

The samples were completely immersed in a temperature controlled tank filled with distilled and degassed water at 25°C [27]. The sample surfaces were placed in the focal plane of the transducer. C-scans were acquired. The entire pulse echo signal was stored for each scanned point. A scan increment of 16 µm was chosen for the acquisition.

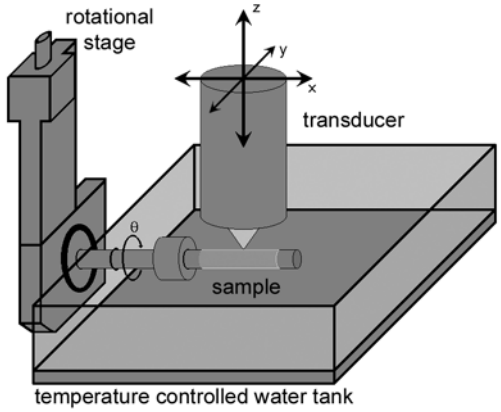

Figure II.5 *Experimental configuration for the femur cylinder scans [36]*.

For complete anisotropic property estimation of cortical bone from cylindrical sample, a rotational stage (DT-80; Micos GmbH, Eschbach, Germany) and a custom made sample holder were attached to the microscope (Fig. II.5). This setup allowed precise rotation of the cylinders in a temperature controlled water tank. The distilled and degassed water at 25°C used as coupling fluid.

For automatic eccentricity-compensated scans of the cylinder surfaces a new scanning procedure was developed and implemented in the microscope control software (Fig. II.6a). First, a *V(θ,t)* scan measured the time-of-flight (TOF) of the cylinder surface reflection at the centre of the manually selected *x*-scan range as a function of the rotation angle θ (Fig. II.6b). From the TOF the eccentricity of the cylinder long axis relative to the rotation axis was calculated. If the maximum variation of the transducer-sample distance due to an imperfect alignment with the rotation axis exceeded 50 µm, a readjustment of the sample was required. Otherwise for each rotation angle θ the *y*- and *z* coordinates with the best alignment of the focal point of the transducer with the cylinder surface were calculated.

For mapping the acoustic impedance at the cylinder surface successive scans in the *x* direction were acquired while the cylinder was rotated stepwise (*V(x,θ,t)* scan). After each *x*-scan the transducer was repositioned in the *y* and *z* directions. The radio frequency (RF) signals were captured every 20 µm and every 0.5° in *x*- and θ directions, respectively. The rotation step size corresponds to a lateral distance of 19.2 µm between two sampled points at the surface of the cylinder.

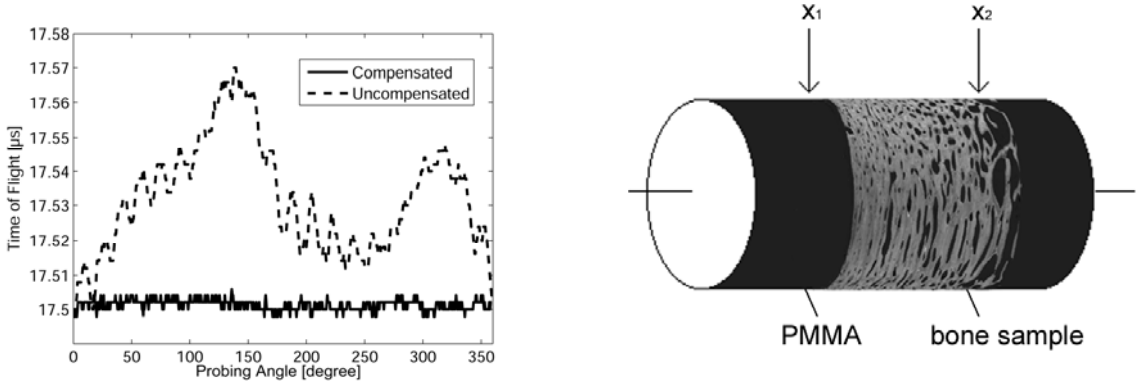

a) *b)*

Figure II.6 *Eccentricity compensation (a). From the TOF(θ) measured in the central region of the cylinder the deviation from the confocal TOF (17.55 µs) and hence the necessary correction in y and z directions were estimated. The TOF(θ) with eccentricity compensations shows an almost perfect confocal alignment. The entire surface reflectivity reconstruction of the sample is shown in (b) [36].*

II.3.2.2 Impedance estimation

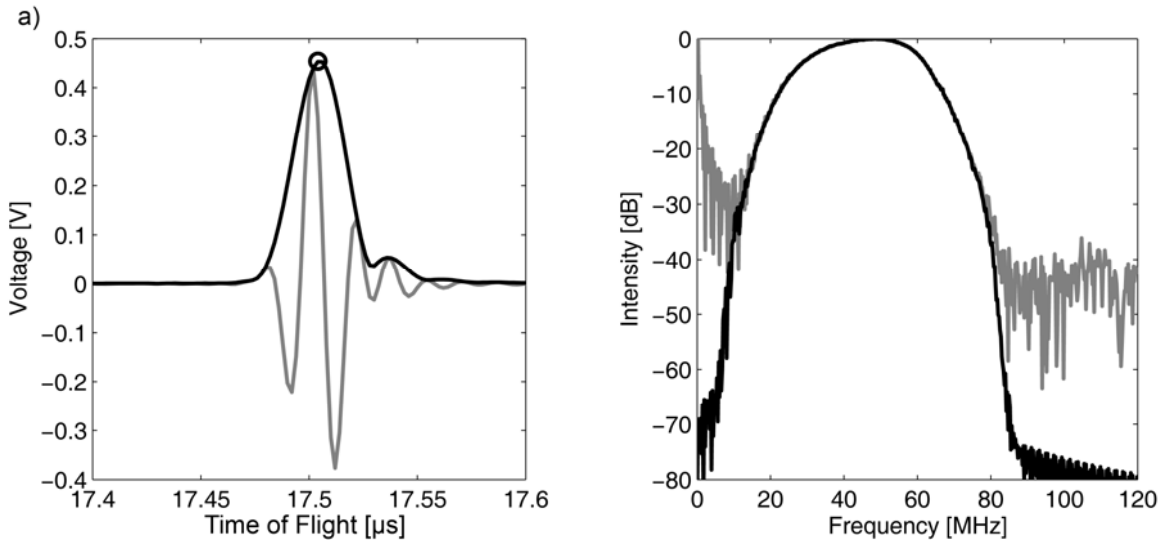

Figure II.7 *Band-pass filtered confocal pulse-echo signal (gray) and Hilbert-transformed envelope signal (black) obtained from a PMMA sample (a). The amplitude of the Hilbert-transformed signal (circle) was used for the impedance estimation. The unfiltered (gray) and filtered (black) power spectra in (b) show the elimination of the DC component by the applied band-pass filter [36].*

All RF signals were band-pass filtered with cut-off frequencies of 5 and 90 MHz using a zero-phase type II Chebyshev filter to remove the DC component as well as unwanted signals outside the bandwidth of the transducer (Fig. II.7) [27;37;145;149]. For homogenous reference materials (TPX®, polystyrene, polycarbonate, PMMA, suprasil®, aluminum, titanium) the pulse echo signal was measured as a function of the sample-transducer distance. A decrease of the reflection amplitude due to a small defocus can be compensated by a *TOF* dependent correction function [4;27;37;150]. The defocus corrected amplitudes of the Hilbert-transformed envelope signals were correlated with the known reflection coefficients of the reference materials, as described elsewhere [4;27;37]. Briefly, the amplitudes of the envelope signals were converted to decibels (0 dB corresponds to the confocal echo amplitude). For each transducer-sample distance the TOF and the corresponding normalized intensity were determined (Fig. II.8). It can be seen that the standard error of the correction function increases with increasing defocus. Thus, only the *TOF* range, where the uncertainty results in a relative error of the impedance estimation of less than 1% (for an average impedance of Z = 8 Mrayl in bone tissue), was accepted for a defocus correction. For echoes measured within the accepted range the *TOF* was used to estimate the confocal reflection

amplitude. After defocus correction the echo amplitudes were converted into corresponding acoustic impedance values using Eq. (II.1). The above mentioned impedance estimation procedure was performed for both femur cross sectional and cylindrical samples.

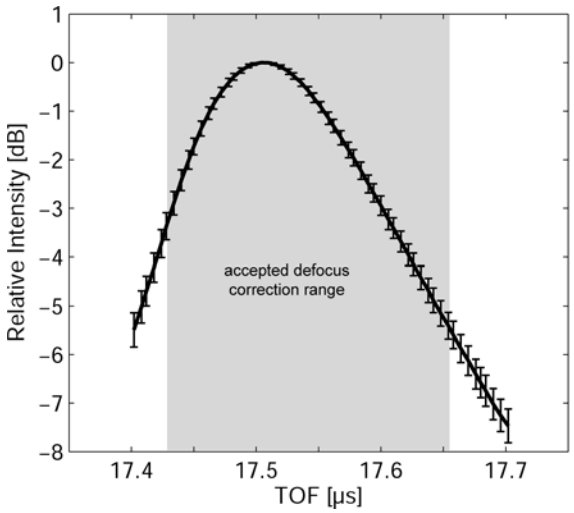

Figure II.8 *Defocus correction function (mean and standard error in dB). The gray area corresponds to the range, for which the uncertainty of the defocus correction results in relative error of the impedance estimation of less than 1% [36].*

II.3.2.3 Image segmentation

To evaluate the impedance of the bone tissue, all voids filled with the embedding material, e.g., Haversian canals had to be excluded from further analysis. Theoretically, the best segmentation using thresholds is obtained if the threshold value $Z_{threshold}$ is:

$$Z_{threshold} = \frac{Z_A + Z_B}{2}, \tag{II.6}$$

where Z_A and Z_B are the impedance values of the materials to be included and excluded, respectively. The segmentation is achieved by considering only pixels with impedance values larger than $Z_{threshold}$. In bone the impedance values vary with respect to the probing angle θ, while the impedance of PMMA is independent of θ [27]. Moreover, the impedance values of osteonal tissue are considerably smaller than those of interstitial tissue [4]. A typical impedance value measured in cortical bone shows a narrow distribution of the impedance measured in the voids (Z_{PMMA}) and a broad distribution (Z_B) that is composed of the

impedance values measured in osteonal and in interstitial tissue (Fig. II.9). As an approximation of the impedance value of osteonal tissue needed to calculate the threshold, we used:

$$Z_{threshold} = \frac{\bar{Z}_{PMMA} + (\bar{Z}_B - SD(Z_B))}{2}, \tag{II.7}$$

where $\bar{Z}_{PMMA}$ and $\bar{Z}_B$ are the mean impedance values inside the cavities (which are filled with the embedding material PMMA) and in the bone matrix, respectively. $(\bar{Z}_B - SD(Z_B))$ is the approximated mean impedance value of the osteonal tissue, and $SD(Z_B)$ is the standard deviation of the impedance distribution measured in the entire bone matrix, i.e. osteonal and interstitial tissue. $Z_{threshold}$ was calculated by an iterative procedure. First, a fixed threshold of 4.0 Mrayl was used for a coarse segmentation. The mean impedance value of the voids $\bar{Z}_{PMMA}$ was calculated from all pixels with impedance values below the threshold. The mean $\bar{Z}_B$ and standard deviation $SD(Z_B)$ of bone tissue were calculated from all pixels with impedance values above the threshold. From these values the threshold value $Z_{threshold}$ for the final segmentation was calculated using Eq. (II.7).

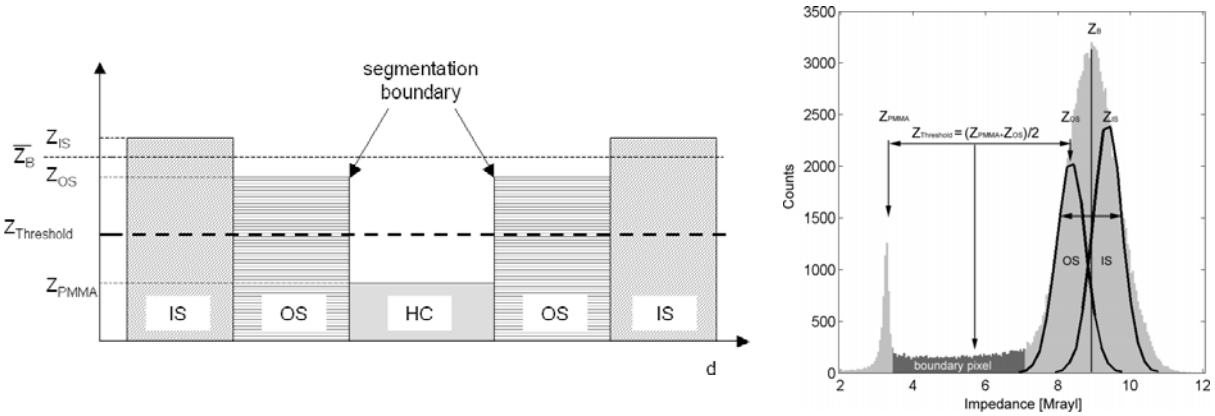

a) *b)*

Figure II.9 *The threshold estimation draft shows the impedance along a line trough a typical structural unit in cortical bone (a). An osteon (OS) with a central Haversian canal (HC) is surrounded by interstitial tissue (IS). An impedance histogram (b) shows a sharp peak corresponding to the impedance of the embedding material and a broad distribution for the values measured in the bone matrix, i.e. osteonal and interstitial tissue. The impedance of osteonal tissue needed for the segmentation was approximated as* $\bar{Z}_{os} \approx \bar{Z}_B - SD(Z_B)$. *Moreover, boundary pixels with artificially altered impedance values (indicated in dark gray) were removed from the impedance estimation by eroding the segmentation mask [36].*

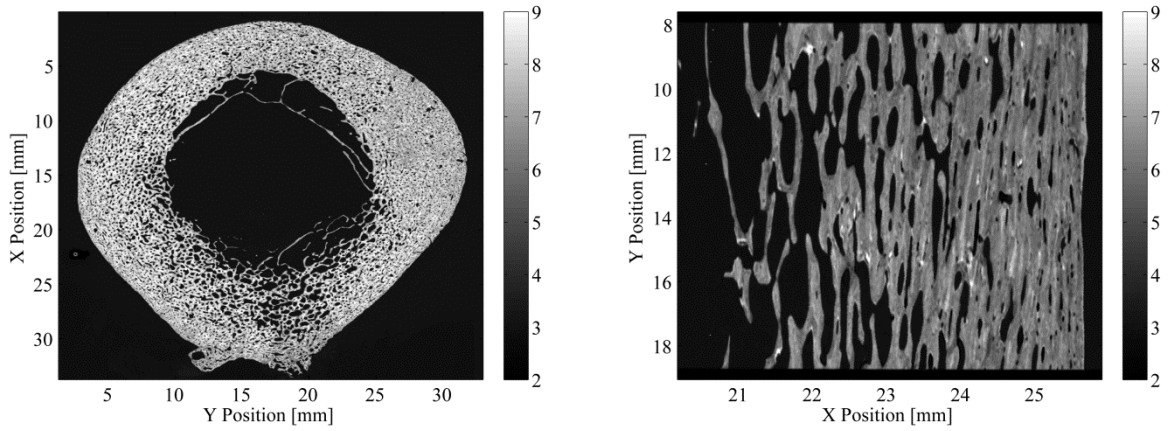

a) *b)*

Figure II.10 *Acoustic impedance maps of a) cross section sample from 29.7% of femur length and b) transverse section from posterior quadrant region.*

To further minimize the influence of the transducer's limited lateral resolution, the transient area between the cavities and bone were excluded by eroding the threshold binary masks with a disk of radius 2 pixels [37]. An example of the surface impedance map for cross and transverse sectional sample is shown in Fig. II.10.

To evaluate the angular dependence of the impedance of the bone tissue from the cylindrical sample, $Z_{threshold}$ (θ) were estimated and applied in the impedance image for each probing angle by an iterative procedure:

$$Z_{threshold}(\theta) = \frac{\overline{Z}_{PMMA} + \left(\overline{Z}_B(\theta)\right) - SD\left(Z_B(\theta)\right)}{2}. \quad \text{(II.8)}$$

Finally, the threshold binary masks were eroded with a disk of radius 2 pixels. The remaining pixels were averaged for each probing angle θ. An example of the surface impedance map after segmentation is shown in Fig. II.11.

With the assumption of orthotropy or transverse isotropy the elastic symmetry axes of the bone tissue are parallel and perpendicular to the femoral long axis and the angular dependent acoustic impedance values $\bar{Z}_B(\theta)$ are symmetric about the symmetry axes. In order to determine the orientation parallel to the femoral long axis, $\bar{Z}_B(\theta)$ was divided into two adjacent 180°-sections $x = \bar{Z}_B(\theta^*)$ and $y = \bar{Z}_B(\theta^{**})$, where $\theta^* = \theta_0,\ldots,\theta_0°+180°$,

$\theta^{**} = \theta_0+180°,\ldots,\theta_0°+360°$, and θ_0 is an arbitrary angle. The maximum of the cross correlation function $R_{xy}(m)$ between x and the flipped version of y is:

$$m_{max} = \arg max_m R_{xy}(m). \tag{II.9}$$

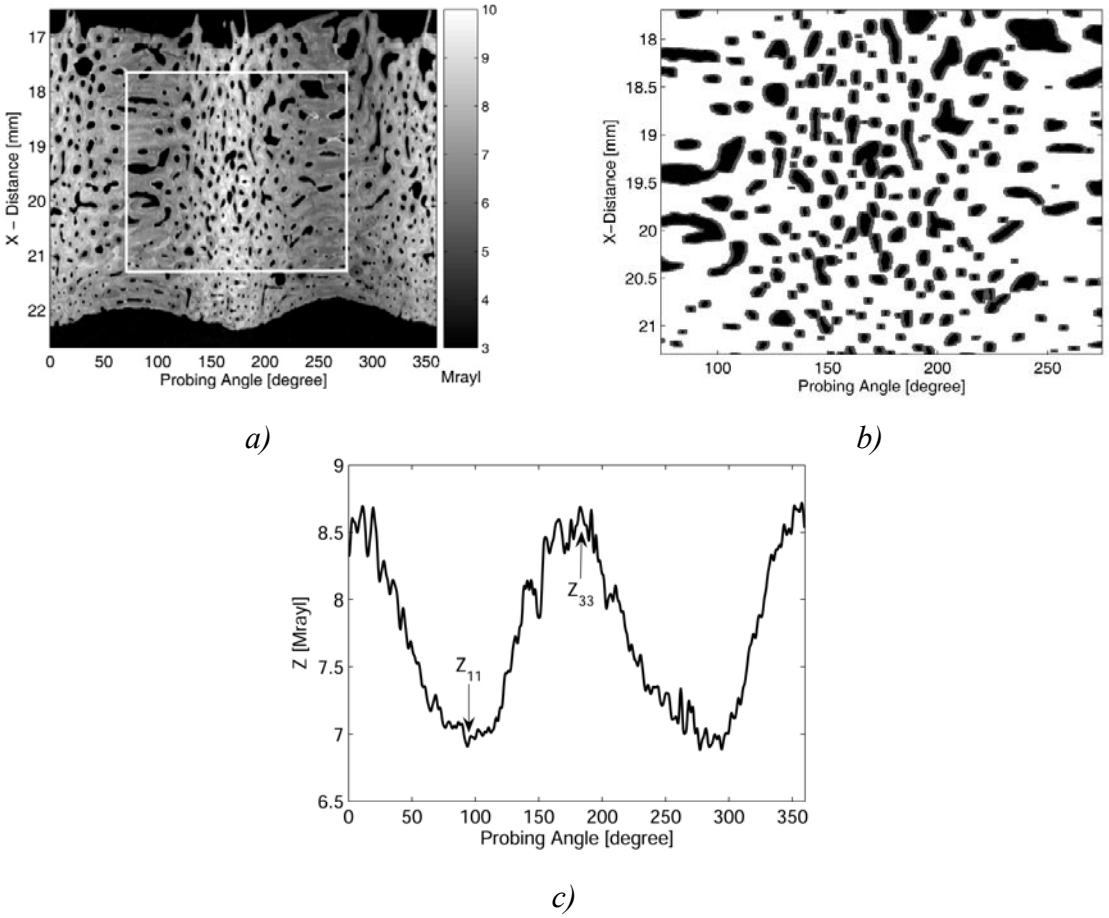

Figure II.11 *Unwrapped acoustic impedance from the surface of the cylindrical sample a). Black and gray regions in b) correspond to the voids excluded by the segmentation procedure. The Z(θ) plot c) shows the mean tissue impedance as a function of the probing angle θ. Z_{33} and Z_{11} are impedances along the long axis and radial axis of the femur shaft, respectively [36].*

m_{max} was calculated for $\theta_0°= 0°,\ldots,180°$. The locations of the maxima of $m_{max}(\theta_0)$ coincide with the orientations of the elastic symmetry axes (Fig. II.12). The maximum position, where the osteon were cut perpendicular with respect to their long axes, was set to $\theta = 0$ (probing orientation parallel to the femoral long axis) [36]. It should be noted that this estimation of the sample orientation is solely based on the anisotropic impedance values of the bone matrix.

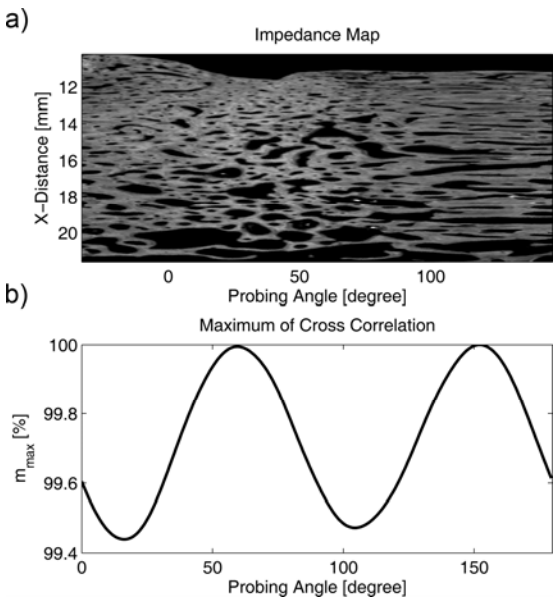

Figure II.12 *Unwrapped impedance image a) and maximum values of the cross-correlation function m_{max} of adjacent flipped 180°-sections of $\bar{Z}_B(\theta)$, shown in percent b). The maxima of m_{max} correspond to the orientations of the elastic symmetry axes of the bone matrix, i.e. at the first and second maxima the osteons were cut perpendicular and parallel to the osteon long axes, respectively [36].*

II.3.2.4 Elastic coefficients estimation

Preininger et al. [151] have shown that the acoustic impedance is highly correlated with the elastic coefficient which was determined by site–matched analysis of acoustic impedance and tissue degree of mineralization (DMB = $v f_{HA} \rho_{HA}$) maps for mature human radius and mice femur samples. The same procedure was applied for this human femur sample. The mass density of the tissue was determined from DMB (Eq. (II.10)) using the relation between the individual volume fractions [25] and the constraint that the volume fractions of hydroxyapatite, collagen and water added to unity. The elastic coefficient was calculated from the relation between acoustic impedance and density by site-matched analysis (Sec. II.A.5) of acoustic impedance map assessed using scanning acoustic microscope and degree of a mineralization map assessed by synchrotron micro-computed tomography. The relations of mass density and acostic impedance with elastic coefficient are shown in Fig. III.3. All impedance values from acoustic maps were converted into corresponding elastic coefficient using the relation (Eq. (II.11)):

$$\rho_{tissue} = vf_{HA}\rho_{HA} + vf_{col}\rho_{col} + vf_{H_2O}\rho_{H_2O} \quad \text{(II.10)}$$

$$c(\theta) = 0.610(\bar{Z}_B(\theta))^{1.934} \quad \text{(II.11)}$$

The off-axis elastic coefficient $c(\theta)$ for a transverse isotropic material is obtained from Eq. (II.1). $c(\theta)$ depends on four out of five independent elastic coefficients of the transverse isotropic stiffness matrix [C]. c_{33} and c_{11} are elastic coefficients parallel and perpendicular to the femur long axis, respectively. Therefore a fit of Eq. (I.26) to $c(\theta)$ gives c_{33}, c_{11}, and c^* (Fig. III.2) with:

$$c^* = c_{13} + 2c_{44} \quad \text{(II.12)}$$

c_{12} and c_{13} were extracted using continuum micro-mechanical model constraints. Hellmich et al. [152] proposed that the ultrastructure of bone, i.e. the bone tissue matrix without pores, can be modeled as an open mineral foam matrix reinforced by collagen inclusions. With an *a-priori* knowledge of the stiffness properties c_{HA}, c_{coll}, and c_{H2O} (Table II.2) the stiffness matrix [C] is predicted by experimental determination of the volume fractions of hydroxyapatite vf_{HA} and collagen vf_{col}. According to Hellmich *et al.* [153], vf_{HA} is highly correlated ($R^2 = 0.86$) with c_{33}. Raum *et al.* [25] have shown that the relation between the individual volume fractions is:

$$\frac{vf_{col}}{vf_{H_2O}} = 0.36 + 0.084e^{6.7vf_{HA}}, \quad \text{(II.13)}$$

with an adjusted $R^2 = 0.996$. With the constraint that the volume fractions of hydroxyapatite, collagen and water add to unity, f_{HA} and collagen f_{col} and finally [C] can be estimated using Eq. (II.13). However, a drawback of the reinforced open-foam model is that only the off-diagonal stiffness coefficients c_{12} and c_{13} are predicted with a reasonable accuracy, while the diagonal coefficients are considerably overestimated. Thus only c_{12} and c_{13} were estimated from the model and c_{44} was assessed from Eq. (II.12).

Table II.2 *Stiffness values for the elementary components of tissue (From Hellmich et al. [154]).*

Phase	Bulk modulus k [GPa]	Shear modulus μ [GPa]	Experimental source
Hydroxyapatite	$k_{HA} = 82.6$	$\mu_{HA} = 44.9$	Katz and Ukraincik [155]
Water	$k_{H_2O} = 2.3$	$\mu_{H_2O} = 0$	
Collagen	$c_{3333} = 17.9$	$c_{1133} = 7.1$	Cusack and Miller [156]
	$c_{1111} = 11.7$	$c_{1122} = 5.1$	
		$c_{1313} = 3.3$	

II.3.3 Structural parameters estimation

Structural parameters are extracted from the cross sectional samples. Tissue was separated from the pores (Haversian canals and resorption cavities) which are filled with PMMA by using the threshold value $Z_{threshold}$ (Sec. II.A.2.3) without erosion [37]. From these binary images, the structural parameter, canal density (number of detected canals within the selected cortical bone area , 1/mm^2), porosity (ratio between the area covered by the canals to the total selected bone area, %), median canal diameter (the equivalent diameter was determined from the area of the individual canals, μm) and cortical thickness (mm) were extracted [37].

II.3.4 Homogenized mesoscopic elastic coefficients estimation

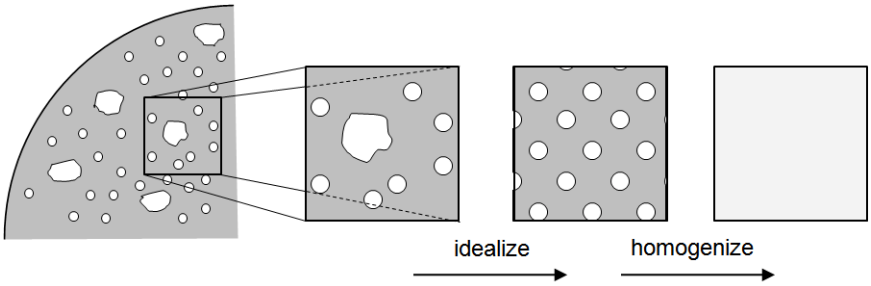

Figure II.13 *The mesoscopic elastic property determination. Here, local region in the cortical bone the cross section is homogenized by considering the medium as periodic and infinite extent along the long axis. The resulting effective properties then define the mesoscopic elastic behavior of this local region. [110;115;157](adapted from [115]).*

W.J. Parnell et al. [115] have been developed a new model of cortical bone elasticity and used to assess the influence of porosity on the induced anisotropic elastic property of the material. Here, cortical bone was described as two-phase composite material: a soft phase, i.e. pores, resorption cavities and Haversian canals containing soft tissues such as cells, blood vessels and nerves distributed inside a complex dense matrix phase. The mesoscale porosity is embedded in a bony matrix. In this model, pores in the local region are assumed to be periodically distributed within the matrix material, specifically on a hexagonal lattice, which leads to a transversely isotropic material for pores with circular cross section (Fig. II.13). The input parameters of the model are microscopic elastic properties of bone matrix and mesoscale porosity derived from SAM data. The asymptotic homogenization method is used to predict the local effective elastic properties by modeling the low-frequency elastic wave propagation through an idealized material that gives the local mesostructure. A novel solution of the cell problem developed by Parnell & Abrahams [158;159] is used. The five effective properties are defined as

$$
\begin{aligned}
c_{33}^{*} &= (1-\phi)(p_0+2m_0)+\phi(p_1+2m_1)+(p_1-p_0)M_3 \\
c_{11}^{*} &= (1-\phi)(p_0+2m_0)+\phi(p_1+2m_1)+[(p_1-p_0)+2(m_1-m_0)]M_1+(p_1-p_0)M_2 \\
c_{12}^{*} &= (1-\phi)p_0+\phi p_1+(p_1-p_0)M_1+[(p_1-p_0)+2(m_1-m_0)]M_2 \\
c_{13}^{*} &= (1-\phi)p_0+\phi p_1+(p_1-p_0)(M_1+M_2) \\
c_{44}^{*} &= (1-\phi)(p_0+2m_0)+\phi(p_1+2m_1)+(p_1-p_0)M_3
\end{aligned}
\qquad \text{(II.14)}
$$

where ϕ is the mesocopic porosity of the bone and,

$$m(x) = \begin{cases} m_1 = \mu_1/\mu_0\,, & x \in D_1 \\ m_0 = 1, & x \in D_0 \end{cases}$$
$$p(x) = \begin{cases} p_1 = \lambda_1/\mu_0\,, & x \in D_1 \\ p_1 = \lambda_0/\mu_0\,, & x \in D_0 \end{cases}$$
$$d(x) = \begin{cases} d_1 = \rho_1/\rho_0\,, & x \in D_1 \\ d_0 = 1, & x \in D_0 \end{cases} \qquad \text{(II.15)}$$

μ_0, λ_0 and μ_1, λ_1 are Lame′ constants of bone matrix and pore respectively. D_0 and D_1 are domain of matrix and pore respectively.

This solution is stable for the physiological range of porosity and elasticity variations found in bone. The bone tissue matrix which is transverse isotropic is represented by hexagonal [157] and pore is modeled as a cylinder of infinite extent in the long axis direction filled with water. The influences of the mesoscale porosity range from 0% to 20% on the bone tissue transverse isotropic elastic coefficients are given in Fig. II.14. 0% corresponds to microscopic elastic coefficients (without pore inclusion). Using this asymptotical homogenization model, the effective elastic coefficients by the combination of tissue elastic coefficients and porosity estimated in this study were analyzed along femur longitudinal, circumferential and radial directions.

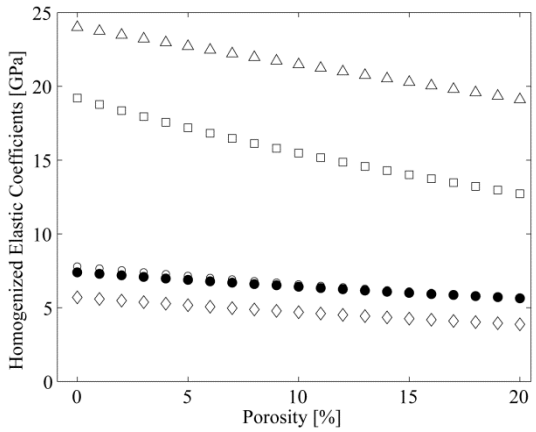

Figure II.14 *Homogenized mesoscopic elastic coefficients c_{33}(Δ), c_{11}(□), c_{12}(•), c_{13}(o) and c_{44}(◊) with inclusion of pore volume fraction from 0 to 20%.*

II.3.5 Degree of mineralization estimation

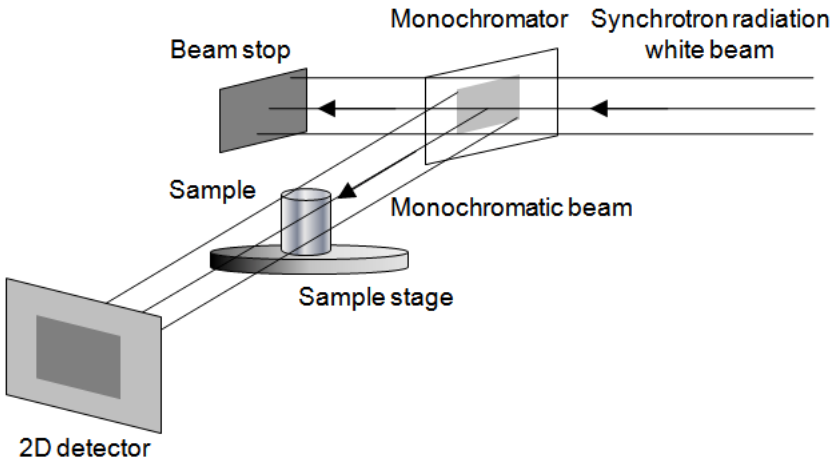

Figure II.15 *Schematic of the SR-µCT acquisition setup [160].*

For bone degree of mineralization (DMB) estimation (Sec. II.1.1), the samples were imaged using synchrotron radiation microtomography (SR-µCT) at the European Synchrotron Radiation Facility (ESRF, Grenoble, France). The experiments were done on beamline ID19, where a 3D parallel beam µCT setup has been developed [140]. A schematic of the acquisition instrumentation is show in Fig. II.15. A Si(1 1 1) single crystal or double crystal monochromator, set to diffract in the symmetrical Bragg reflection geometry, selects the appropriate energy from the white SR beam emerging from the storage ring. The sample is mounted on a goniometer including high resolution translations and rotations to position the sample and to rotate it in the beam. A two dimensional detector records the beam transmitted through the sample.

The energy was set at 26 keV. For each sample 1500 radiographic images fewer than 1400 angels of view were recorded. A 3D volume of (600 x 600 x 650) voxels was then obtained by applying an exact tomographic reconstruction algorithm, based on filtered back projection [160]. The voxel size in the image was 10.1 µm. Gray levels of these 3D data were converted to their corresponding volumetric degree of mineralization values expressed as g/cm^3 of hydroxyapatite crystals by the calibration method [140;160] (Fig. II.16). Prior to further processing the outer cylinder surface was detected and then the data were transformed by translation and rotation operations to align the long axis of the cylinders with the z axis of the Cartesian coordinate system. The site matched acoustic impedance determined from SAM

measurement and DMB determined from SR-µCT measured is shown in Fig. II.18. The DMB of bone tissue were evaluated by excluding all voids filled with the embedding material using 3D imaging segmentation procedure as show in Sec. II.A.2.3 for impedance evaluation only from bone tissue (Fig. II.17). All post processing was done using custom made MATLAB software.

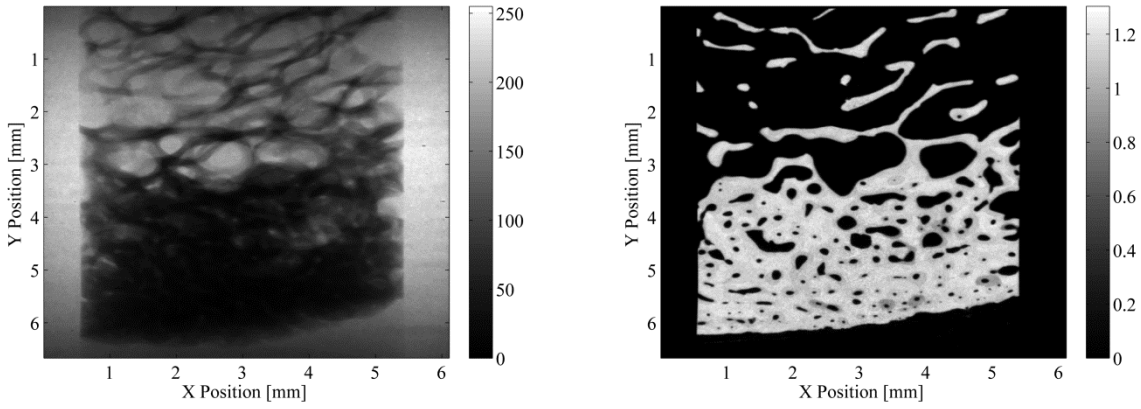

Figure II.16 *a) A 2-D slice extracted from a 3-D gray scale image and the b) corresponding DMB image (g/cm³).*

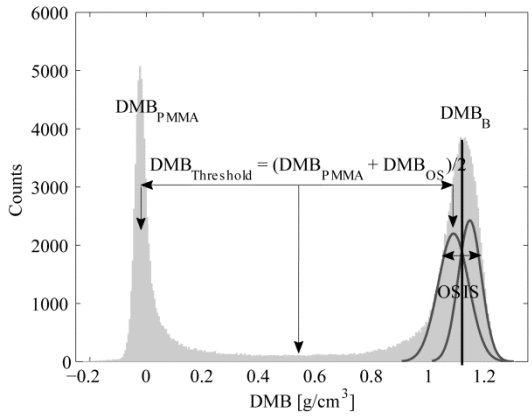

Figure II.17 *DMB histogram shows a sharp peak corresponding to the DMB of the embedding material and a broad distribution for the values measured in the bone matrix image segmentation for DMB estimation from bone matrix, i.e. osteonal and interstitial tissues.*

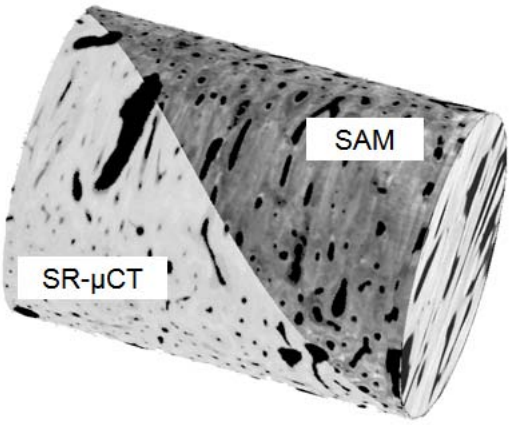

Figure II.18 *Site matched SAM and Synchrotron µCT data [161].*

II.3.6 Statistical Methods

To investigate the variation of elastic coefficients, structural parameters and degree of mineralization with respect to anatomical locations, analysis of variance (ANOVA) test followed by post-hoc Tukey–Kramer multiple comparison tests were performed. The confidence level was set to $p = 0.05$. The strength of significant effects is provided by means of F values. Linear regression and Pearson correlation coefficients were used to study the association between elastic coefficients, degree of mineralization and structural parameters. All statistical computations were carried out using the MATLAB Statistics Toolbox (The Mathworks Inc., Natick, MA, USA).

II.4 Skeletal muscle

II.4.1 Sample preparation

83 pig carcasses of highly varying intramuscular fat content (IMF) (0.63 – 3.16%) were selected at a commercial slaughter plant according to carcass weight and fat to lean ratio [89]. Mean carcass weight was 95.0 ± 7.1 kg. The animals were stunned with CO_2, exsanguinated and scalded at approximately 62 °C. For non-destructive investigation of muscle characteristics, the ultrasonic measurements (Quantative ultrasonic device, Ultrafom300, Sec. II.B.5) were made at suspended carcasses from left half including skin and subcutaneous fat layers. Scanning localization was chosen with respect to the official site of carcass classification at $2^{nd}/3^{rd}$ rib, 7 cm off the carcass split line. Per carcass three replicate scans were performed parallel to the split line using ultrasound contact gel. Muscle (MW)

and back fat width (BW) were determined with a carcass grading probe (Fat-O-Meat'er, SFK Technology, Denmark) and pH values (Knick portamess 913 with SE 104 glass type probe) was recorded at $2^{nd}/3^{rd}$ last rib. Average muscle temperature was 38°C.

Out of 83 pigs, 27 samples were used for further analysis. Approximately 24 h p.m., after chilling of the carcasses over night, three adjacent chops were excised from the *longissimus* muscle at the $3^{rd}/4^{th}$ and $2^{nd}/3^{rd}$ last rib for subsequent laboratory analyses. To analyze the acoustic properties at intact carcass (Sec. II.B.4), a cylindrical muscle sample (about 10g each) per chop was obtained 24 h p.m. at the $2^{nd}/3^{rd}$ last rib and stored in plastic containers for 48 hours at 4 °C. Samples for ultrasound data acquisitions (SAM 10 MHz, Sec. II.B.4) were prepared approximately 24 h p.m.

For muscle's acoustic property analysis at fiber level (Sec. II.B.3), the samples excised from *longissimus* muscle at the $3^{rd}/4^{th}$ last rib were snap-frizzed in liquid nitrogen and stored at 60°C until use. The frozen samples were sectioned parallel and perpendicular to muscle fiber direction approximately 50 µm and 10 µm in thickness for ultrasonic measurement (SAM 100 MHz, Sec. II.B.3) and histology respectively. They were placed on glass slides (Roth; SuperFrost; Nr. 1879; Karlsruhe, Germany) without cover slips.

II.4.2 Chemical and structural properties determination

The muscle pH value (Knick portamess 913 with SE 104 glass type probe) and electrical conductivity (EC; Matthäus LF-Star) were recorded 45 min p.m. at the $2^{nd}/3^{rd}$ last rib. The pH meter was calibrated using 3 buffer solutions at pH 4, 6 and 7 (Carl Roth GmbH, Karlsruhe, Germany) and adjusted for temperature. The pH values were recorded 45 min p.m. as the relationships to compositional parameters (e.g., water content) are expected to be higher at this time compared to 24 hrs p.m.. Drip loss (EZ) was measured using the EZ drip-loss method [144]. Briefly, two cylindrical muscle samples (about 10g each) per chop were obtained 24 hrs p.m. at the $2^{nd}/3^{rd}$ last rib and stored in plastic containers for 48 hrs at 4° C. The chemical and histology analysis were performed at Department of Animal Sciences, in Prof. Michael Wicke's animal products quality lab at Georg-August-University of Göttingen. The intramuscular fat content (IMF), dry matter (DM), and protein (all related to fresh matter) were determined from homogenized muscle samples from the $2^{nd}/3^{rd}$ last rib after removal of the subcutaneous fat. The homogenization was done in a Potter S (Braun Biotech Int. GmbH; Melsungen, Germany) homogenizer at 1500 rpm for 30 seconds. IMF was

determined with petroleum ether using a Soxtherm-apparatus after HCl pre-treatment according to German Food Legislation [89;143]. The determination of dry matter was performed at small samples (~5 g) dried in sea sand at 103°C until equilibrium weight was reached. Protein content was determined automatically after oxidative digestion (Elementar GmbH, Hanau, Germany).

Histology samples were obtained 24 hrs p.m. from the samples of the $2^{nd}/3^{rd}$ last rib. The muscle samples were frozen in liquid nitrogen and stored at -60 °C until use. A modified ATPase/NADH-TR staining [142] was performed on 10 µm cross cryosections (CM 1900; Leica Microsystems GmbH; Wetzlar, Germany). For determination of fiber type proportions, slow-twitch oxidative (STO), fast-twitch glycolytic (FTG), and fast-twitch oxidative (FTO) fibers were counted and the fiber diameters were determined manually. At least 2 field of view and 300 fibers per sample were examined on digital light micrographics (100 x magnification; NIS-Elements; Nikon GmbH, Düsseldorf, Germany).

II.4.3 Evaluation of fiber level acoustic properties of muscle

Most of the previous studies on skeletal muscle [162-164] have been done at the macromolecular level with a low megahertz frequency range from 1 – 20 MHz. But, it is not clear to what degree the oriented structures of the muscle contribute to ultrasonic propagation properties. Only a few studies have been conducted to find variations of acoustic parameters at tissue level, e.g., within single muscle fibers. Tervola [165] has analyzed the change in acoustic properties with respect to fat concentration in rat liver. Smith NB and O'Brien [87] investigated ultrasonic propagation properties of bovine psoas major, *longissimus* dorsi and lobster extensor muscles. The scanning laser acoustic microscope (SLAM) of central frequency 100 MHz was used in those studies. The SLAM operates in through transmission technique and has a comparatively lower resolution than scanning acoustic microscope.

II.4.3.1 Ultrasonic data acquisition

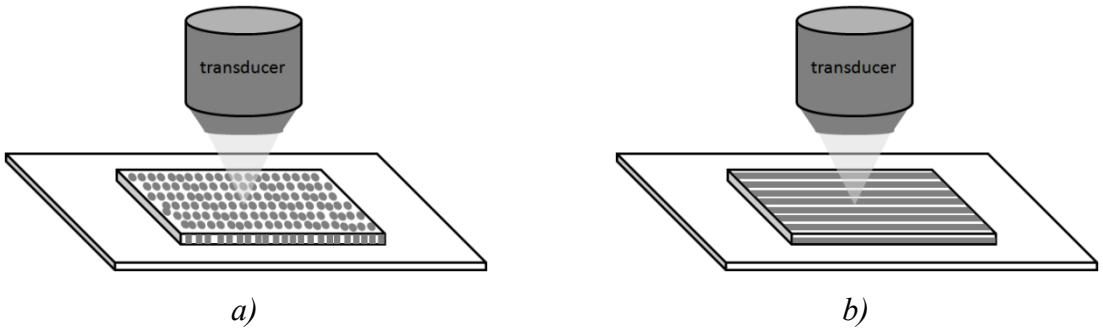

Figure II.19 *Schematic of muscle fiber level acoustic parameters measurement setup along the a) fiber parallel and b) perpendicular to sound propagation direction.*

For the estimation of microscopic acoustic properties of muscle, a 100 MHz central frequency transducer (V611, Valpey Fisher, Hopkinton, MA) was equipped with SAM (Sec. II.2). The sound field characteristics of the transducer are summarized in Table II.***1***. The received echo signals were digitized at 400 MS/s with a 12-bit analogue-to-digital converter (CS12400, Gage Applied Technologies, Inc., Lachine, Mon, Canada). Distilled and degassed phosphate-buffered saline at 38°C was used as a coupling fluid.

Two RF data sets were acquired for each measurement. First, a C – scan was acquired from the muscle region by placing the transducer's focal plane between the front and back side reflections of the section and the entire pulse-echo signal was stored. The scan increment between two sampled points was set to 16 µm in both scan directions. Second, a B(z)-scan was acquired from the substrate region with the scan increment 4 µm along the z axis for defocus correction and impedance calibration [27]. The Hilbert transformed amplitude distribution from muscle fiber parallel (sound propagation along the fiber orientation) and muscle fiber perpendicular (sound propagation perpendicular to fiber orientation) samples are given in Fig. II.20. It shows the arrangement of muscle fibers in *longissimus* muscle along the parallel and perpendicular to the long axis. Each of the muscle fibers (dark) are distinguishable, they are surrounded by the connective tissue endomysium (white). Even muscle bundles are visible, surrounded by perimysium.

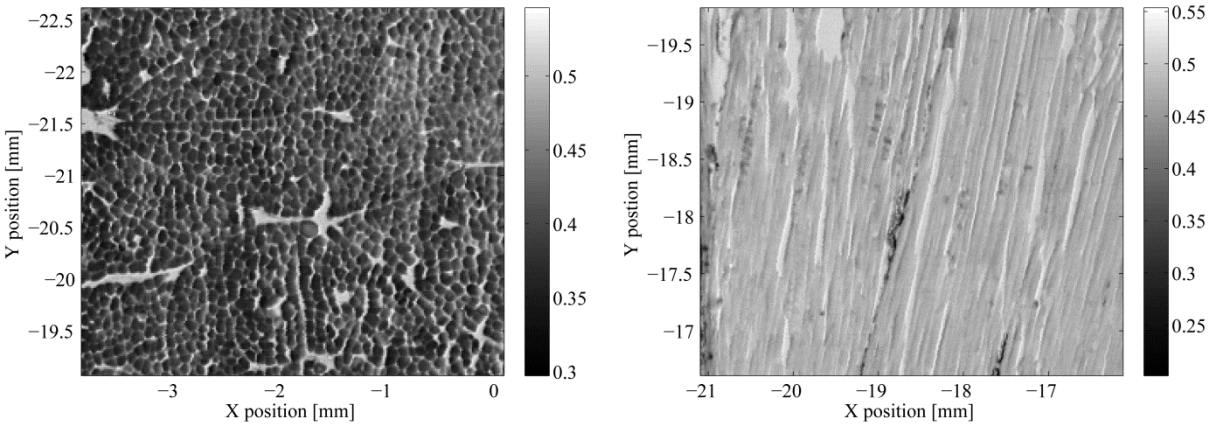

a) *b)*

Figure II.20 *Hilbert transformed amplitude distribution from a) muscle fiber parallel and b) muscle fiber perpendicular samples. The fibers (dark) are surrounded by the connective tissues (white)***.**

II.4.3.2 Ultrasonic data analysis

The front echo coming from the sample surface was very small compared to the back echo from the interface sample/substrate (Fig. II.21a). In order to separate these two echoes, a cepstral method was used [84]. Briefly, the power spectrum was calculated from the entire RF signal $\langle S_m(f,z)\rangle$ and normalized to the corresponding reference spectrum $\langle S_{ref}(f,z)\rangle$ from the glass substrate as shown in Eq. (II.16):

$$\langle S_{cor}(f,z)\rangle = \frac{\langle S_m(f,z)\rangle}{\langle S_{ref}(f,z)\rangle} \tag{II.16}$$

The cepstrum was calculated by taking the Fast Fourier Transformation (FFT) of the normalized power spectrum within the frequency bandwidth of the transducer [84]. The cepstrum's maximum peak position τ_{max} (Fig. II.21b) represents the time of flight difference ($T_{mb} - T_{mf}$) between the front and back echoes (Fig. II.21a).

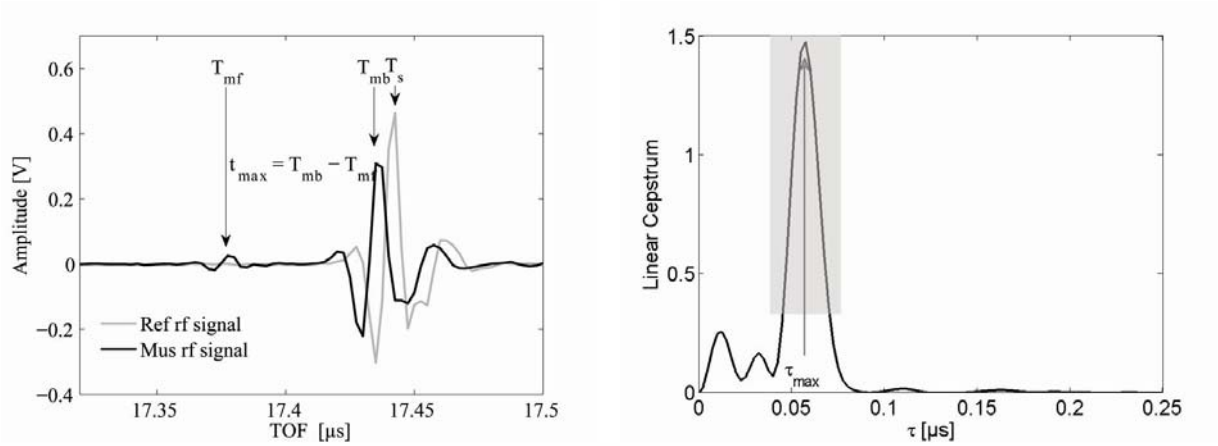

a) *b)*

Figure II.21 *a) Exemplary radio frequency signals for a single scan position with and without a sample. The cepstrum τ_{max} value corresponds to time of flight difference between front and back echoes of the muscle sample. b) Cepstrum method used to separate two echoes .The threshold range is marked in gray to exclude the connective tissue and sample detached region from the substrate.*

The signal amplitudes from the connective tissue regions between the muscle fibers were too small to be detected. Therefore, connective tissue regions were excluded by a threshold in the cepstral amplitude. Moreover, a τ_{max} range was defined to exclude regions with unlikely high pulse separations, e.g., caused by a detachment of the sample from the substrate. Thickness d and speed of sound v were calculated from travel time differences with and without a sample as shown in Eqs. (II.17) and (II.18) [166;167].

$$d = \frac{v_o(T_s - T_{mf})}{2} \tag{II.17}$$

$$v = \frac{v_o(T_s - T_{mf})}{(T_{mb} - T_{mf})} \tag{II.18}$$

where v and v_o (1540 m/s at 38 ^oC) are speed of sound of muscle and coupling fluid (PBS) respectively. The ultrasound velocity of the PBS (v_0) was determined from B(z)-scan acquired from the substrate region using the definition that the rate of change of distance with time. The RF data taken into account for acoustic parameters estimation were further restricted from the mean and standard deviation of thickness estimated from its histogram distribution. Especially in the perpendicular samples, the cutting place may be at the center of the muscle fiber, the fiber edge or the connective tissue region.

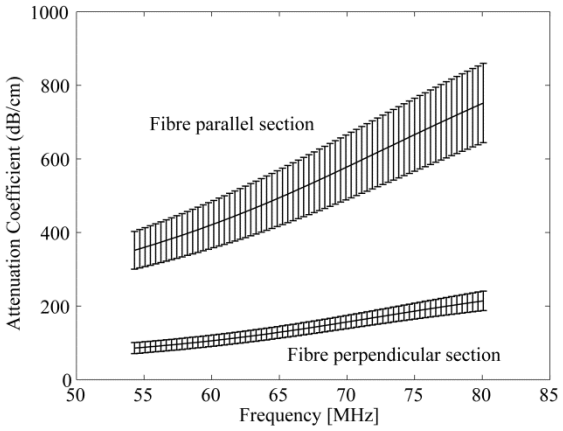

Figure II.22 *Example of attenuation coefficient in a single muscle along the fiber in parallel and perpendicular directions.*

For acoustic attenuation, the power spectrum $\langle \boldsymbol{S_{mb}(f,z)} \rangle$ was calculated from gated muscle back echo signal (gate length: 2 times pulse length) and subtracted to the corresponding reference spectrum $\langle \boldsymbol{S_{ref}(f,z)} \rangle$ as shown in Eq. (II.16). Then, the spectral difference was normalized to the sample thickness. Linear regression was performed on normalized power spectrum within the frequency bandwidth (Fig. II.22). The slope of the linear fit provided the attenuation coefficient α in $dBMHz^{-1}cm^{-1}$. The PBS solution density was measured using a pycnometer at 38 °C. Then, the PBS impedance $\boldsymbol{Z_0}$ was estimated using its density and sound speed (Eq. (II.19)). A defocus correction and impedance calibration were obtained from the B(z)-scan data measured in the substrate regions according to [27]. With this calibration the front echo voltage values could be converted into acoustic impedance values as shown in Eq. (II.19).

The measured impedance and speed of sound were used to estimate density ρ and elastic coefficient c from the relations [25]:

$$Z = \rho v \tag{II.19}$$

$$c = \rho v^2 \tag{II.20}$$

respectively. The processing of the pulse echo data for each scanned position yielded parametric maps of sound velocity, acoustic impedance, attenuation and mass density (Fig. II.23).

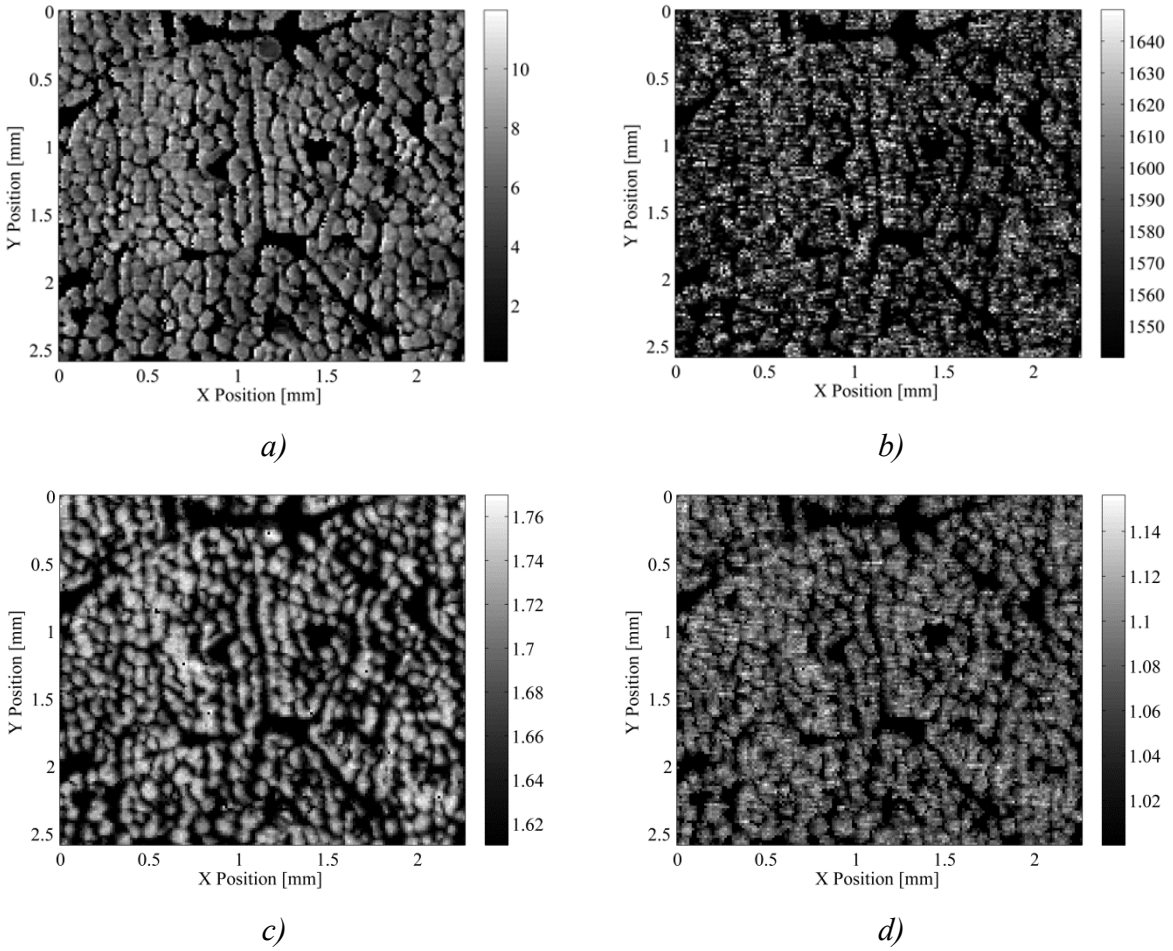

Figure II.23 *Acoustic parameters from one of the fiber parallel samples. a) attenuation (dB/MHz/cm), b) speed of sound (m/s), c) impedance (Mrayl) and d) density (g/cm^3).*

II.4.3.3 Histology comparison

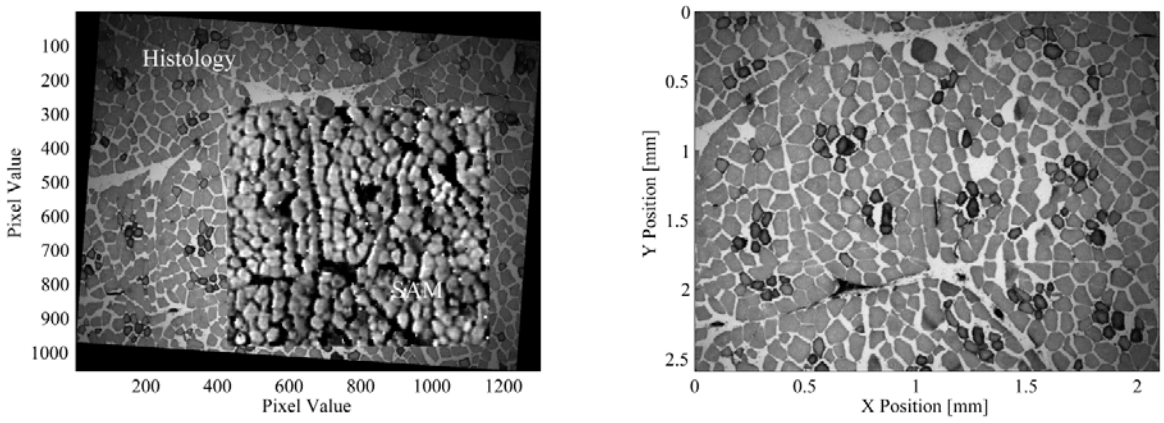

a) *b)*

Figure II.24 *a) A site matched SAM and histology data. b) ATPase/NADH-TR stained histology for fiber type differentiation.*

A modified ATPase/NADH-TR staining [142] to differentiate the muscle fiber type's histology is show in Fig. II.24b. The dark gray corresponds to slow twitch oxidative (STO), intermediate gray to fast twitch oxidative (FTO) and light gray to fast twitch glycolytic (FTG). A site-matched analysis of the acoustic parameters with histology sections was performed to evaluate acoustic differences between the muscle fiber types. For that, the acoustic parameter images were registered with the histology images (Fig. II.24a). The acoustic parameters of each fiber type were extracted by applying gray scale threshold values to the histology data. Due to the difficulty in fixing the gray boundary value between FTO and FTG, fiber types are differentiated as STO and FTO+FTG in this study. The histology and acoustic maps estimated from the fiber perpendicular sections are not comparable because sample thickness is close to fiber diameter. Therefore, acoustic parameters of fiber types were analyzed only from fiber parallel sections.

II.4.4 Estimation of macroscopic acoustic parameters of porcine muscle and back fat compound

For intermediate medium attenuation and refraction correction for backscatter data acquisition anticipated to improve non-invasive ultrasound based muscle characteristic estimation (Sec. II.B.5), the calculations of reference acoustic parameters from muscle and back fat compound are shown in this section.

The chops taken from the 2nd/3rd rib last rib were used for skin and back fat acoustic parameter estimation (Sec. II.B.1). All samples were kept in the refrigerator at 4 °C until ultrasound measurements were performed within 72 to 96 hrs post mortem. Prior to measurement 2 adjacent samples were prepared from each chops as follows: both samples were cut to a side length of about 1.5 cm. The first sample was measured as a complete back fat block including skin (compound sample). The second sample was dissected, and the fat layers and the skin were measured individually. For muscle, subsample with an edge length of about 1.5 cm was prepared from the excised chops. This subsample was prepared from the standard ultrasound scanning localization at *M.longissimus* which is official site of carcass classification at slaughter to predict meat quality using a B mode device. That is, at 7cm from the middle line of the pig back towards the ventral at 2nd/3rd rib [89]. In this location, muscle fiber orientation is 30° to 45° relative to the sound propagation direction. Care was taken to ensure that sample orientation was similar. Prior to ultrasonic measurement the all the samples were allowed to equilibrate by keeping them in phosphate buffered saline (PBS) at 38 °C as an isotonic medium.

II.4.4.1 Ultrasonic data acquisition

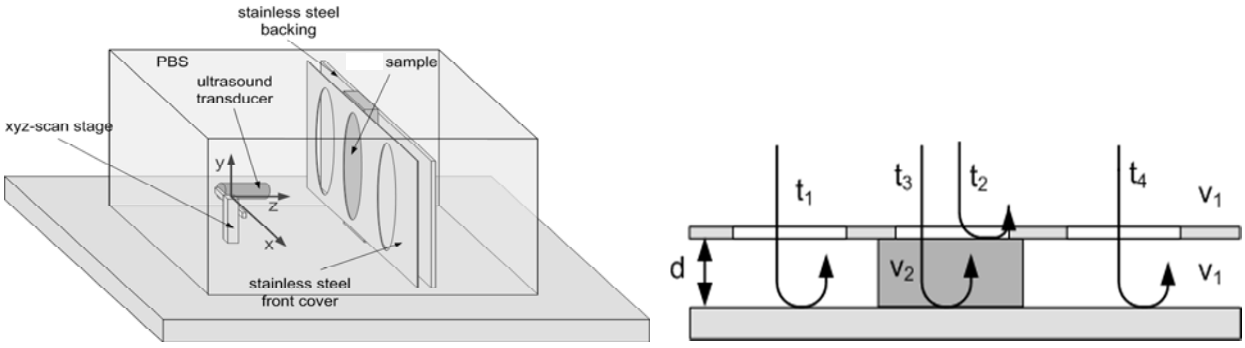

a) *b)*

Figure II.25 *a) 10MHz SAM scan set-up. Samples are fixed in the middle chamber and 150 A-scans are performed. b) Recorded echo positions used for calculations of the sound velocity. t_1, t_4: travel times in PBS; t_2: pulse position of the front echo; t_3: travel time with sample; v_1: PBS sound velocity; v_2: sample sound velocity[168].*

For acoustic reference data collection of porcine muscle and back fat compound, a 10 MHz transducer (V311, PANAMETRICS, Waltham, USA) was equipped with SAM (Sec. II.2). The sound field characteristics of the transducer are summarized in Table II.1.. The received echo signals were digitized at 50 MS/s with a 12-bit analogue-to-digital converter (CS12400, Gage Applied Technologies, Inc., Lachine, Mon, Canada) and input range was set to ±500 mV. Distilled and degassed phosphate-buffered saline at 38°C was used as a coupling fluid.

II.4.4.2 Ultrasonic data analysis

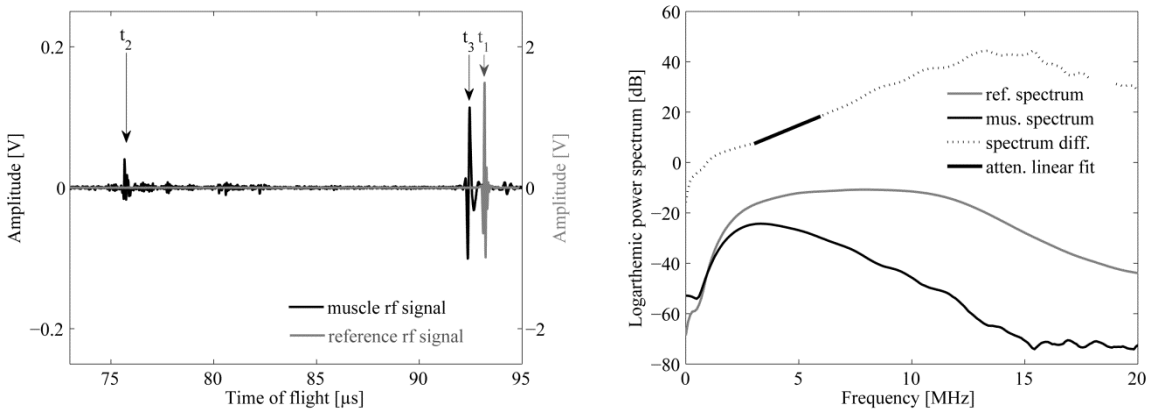

a) *b)*

Figure II.26 *a) Recorded RF signal echo positions used for calculation of the speed of sound and b) corresponding power spectrum used for calculation of attenuation.*

The sample was placed in a custom made multi-chamber-holder (Fig. II.25a). This chamber holder allowed the acquisition of the echoes from a plane steel reflector with and without sample, as well as tight attachment of the sample without compression. The scans were performed with a step width of 0.4 by 1 mm, resulting in approximately 150 radio frequency (RF) lines per chamber. For coupling of the acoustic waves the sample and the transducer were submerged in degassed phosphate-buffered-saline (PBS, 0.9 % in water v/v) as an isotonic medium. The ultrasound velocity of the PBS (v_{PBS}) was measured prior to every sample measurement and this specific velocity values were used in further calculations. The temperature was kept at $38.0° \pm 0.1°C$. Prior to each measurement the samples were equilibrated in PBS.

Ultrasound velocity and acoustic attenuation were analyzed using a custom made MATLAB (The Mathworks, Natick, USA) based software package. Briefly, this software allows a semi-automatic detection of the front and backside reflections within the sample area and the detection of the steel plate reflection in the adjacent reference chambers (Fig. II.25b). From these echoes the travel times t_i were determined from the position of the maximum of the Hilbert-transformed envelope signal [36]. Thickness and sound velocity were calculated from travel time differences with and without the sample (Fig. II.26a) using a substitution method [167] (Sec. II.B.3.2).

Acoustic attenuation was estimated by comparing the logarithmic power spectra of pulses obtained at the tissue-backplate reflector to the spectra measured in the reference chambers (Fig. II.27b). The spectrum difference were normalized to the sample thickness and a linear fit was performed within the frequency band for which sufficient signal amplitudes were obtained in the attenuated signals (3 to 6 MHz). The slope of the linear fit provided the attenuation coefficient in $dBMHz^{-1}cm^{-1}$.

Prior to signal analysis, a region of interest (ROI) in the sample chamber (skin or fat or muscle) was manually selected, resulting in approximately 75 A-lines per sample (after excluding outliers). Each data set was analyzed by two independent trained users to estimate the effects in terms of software handling. The mean differences between both users were less than 0.1% for sound velocity and less than 2.5% for attenuation. Therefore, the data processing was considered as not being affected by insufficient handling of the software if performed by trained users. Subsequently, the mean values of both users were used for further statistical analyses.

II.4.5 Non-destructive estimation of porcine *longissimus* muscle characteristics

II.4.5.1 Ultrasonic data acquisition by quantitative ultrasonic device

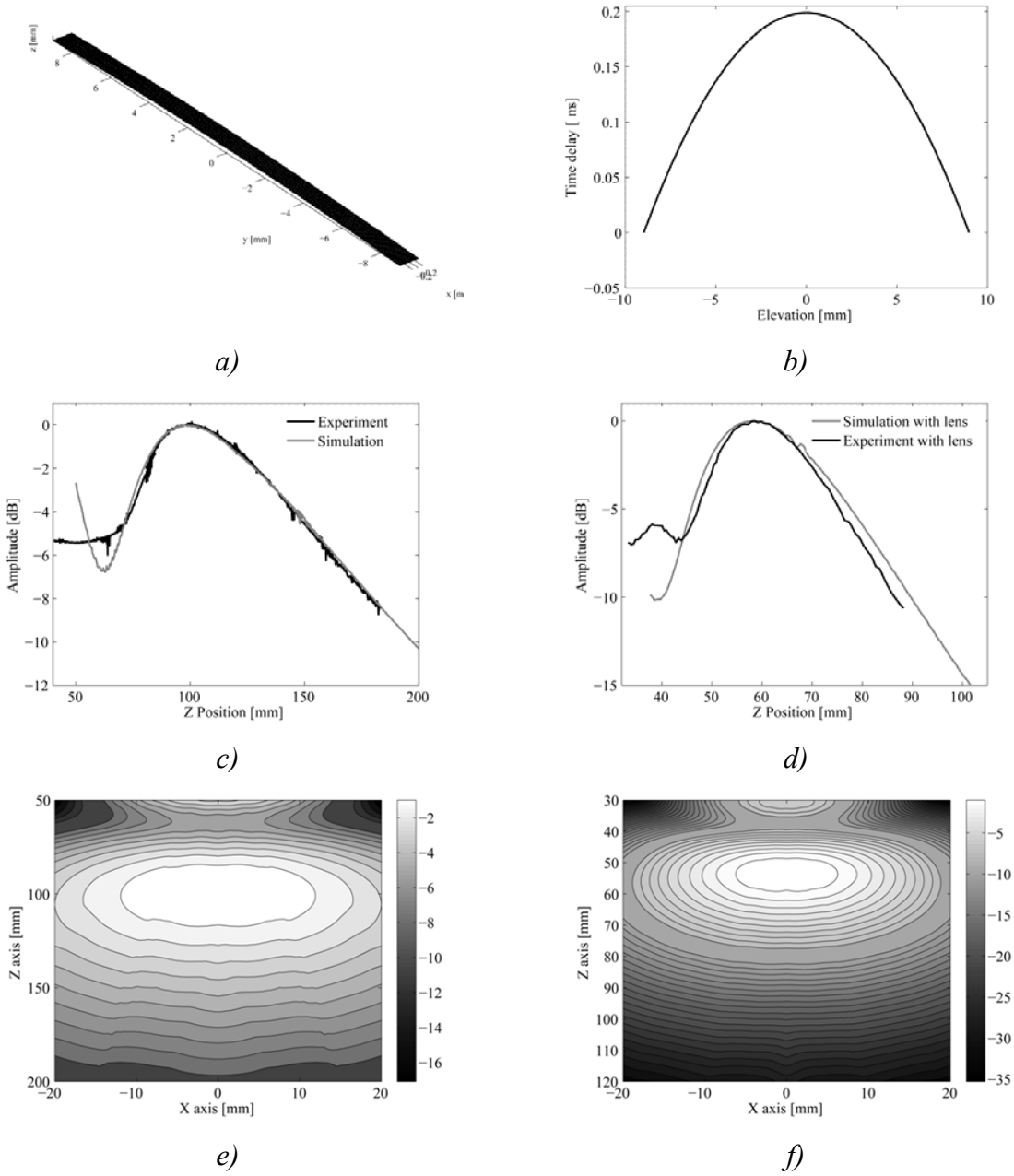

a) *b)* *c)* *d)* *e)* *f)*

Figure II.27 *a) Stimulated UF300 transducer, b) estimated necessary time delay to get the focus inside the muscle region, Sound field function of UF300 estimated from simulation and experiment without (c) and with acoustic lens (d). Contour plot of spatial intensity distribution (in dB) of UF300 with (e) and without (f) acoustic lens.*

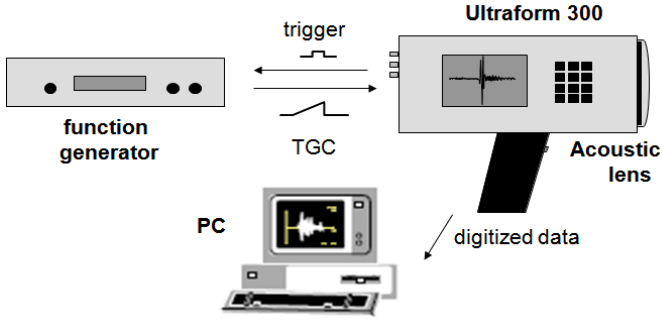

Figure II.28 *Block diagram of modified Ultrafom 300 ultrasonic measurement system.*

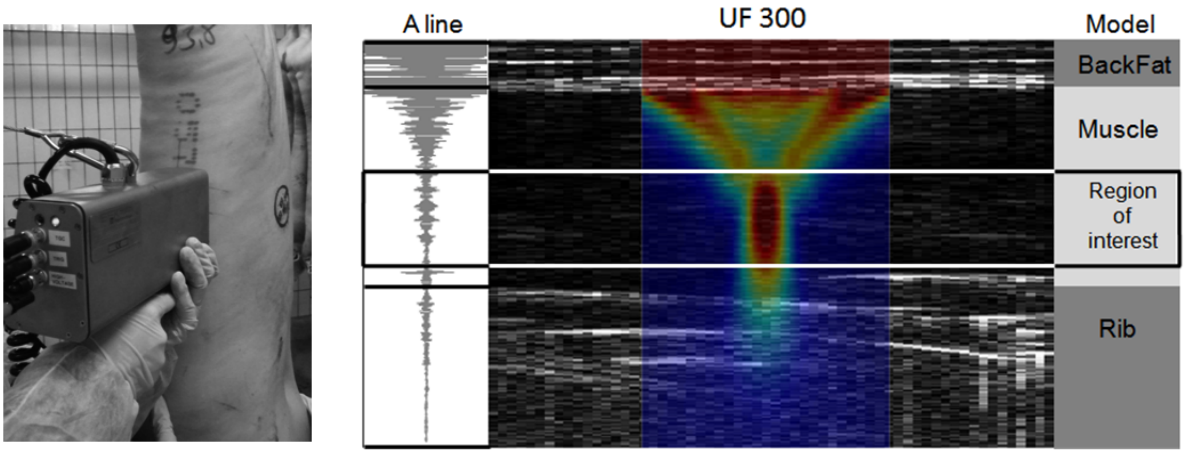

Figure II.29 *Ultrasound data acquisition on hanging pig carcasses at slaughter (a). B-mode image of porcine muscle and acoustic focus (b). One of the attenuated RF signals while passing through the medium is illustrated.*

For ultrasound RF data acquisition, a modified Ultrafom300 (SFK Technology A/S, Denmark) was used. The original device consists of a linear array of 64 unfocused transducer elements aligned along the *y*-axis. The nominal center frequency of the elements is 3.2 MHz. Each element is excited separately and produces an elliptically shaped sound field with focus at a distance of approximately 100 mm. The beam in the focal plane has -6-dB extensions of 2.5 mm and 50 mm in the *x*- and *y*- directions respectively. This configuration has been optimized to measure the acoustic reflections at the muscle rib interface over an area of approximately 2.5 mm x 100 mm (with the long dimension parallel to *y*-axis and the carcass split line). It should be noted that this system was not developed for imaging. The near field, i.e. the range from the transducer surface to the focal plane, is characterized by an inhomogeneous pressure distribution, rendering a quantitative backscatter analysis

impossible. Therefore, an acoustic lens was designed to shifts the focus of the sound field towards the muscle region and produces smooth spatial and spectral characteristics within the muscle region of interest. The necessary radius of curvature *ROC* of the lens was computed using the Field II simulation software [169]. The lens was designed using silicone rubber (Elasosil M4641, Wacker Chemie AG, Munich, Germany) mixed with aluminium oxide particles (30 wt%; mean diameter: 5 µm). A time dependent amplification (time gain compensation, TGC) of the pulse echo signal was realized by an external function generator (HM 8150, HAMEG Instruments GmbH, Mainhausen, Germany) (Fig. II.28). A linearly increasing ramp function ensured a good signal-to-noise ratio over the entire depth down to the muscle/rib boundary. With these hardware modifications, the measured center frequency of a pulse reflected at a plane reflector in the focal plane was 2.7 MHz. The other spatial, temporal and spectral sound field characteristics with and without the lens are summarized in Fig. II.27 and Table II.3.

Ultrasound data acquisition was performed about 45 min post-mortem after carcass classification. The mean carcass temperature was 38°C. Scanning localization at M.*longissimus* was chosen with respect to the official site of carcass classification at slaughter ($2^{nd}/3^{rd}$ last rib) (Fig. II.29a) [89]. The UF300 transducer was placed about 7 cm from the middle line of the pig back towards the ventral. As for ultrasonic scanning direction, the transducer was positioned perpendicular to the muscle fiber direction. But, in the intact carcass, muscle fibers are not aligned exactly parallel to skin surface at M.*longissimus*. So the sound propagation direction can consider 30° to 45° relative to fiber orientation. Three scans per carcass were performed and the corresponding data were stored separately. Sonogel was used as a coupling medium.

The pulse-echoes of all 64 elements were digitized with a sampling frequency of 10 MHz and 8 bit resolution in a pulse echo time interval of 153 µs and stored on a computer for offline processing. All subsequent data processing steps were performed with custom functions using MATLAB R2008a® software (Mathworks Inc., Natick, MA).

Table II.3 *Sound field characteristics of Ultrafom 300 with and without acoustic lens.*

Physical Parameters		Beam Parameters		
Type	Linear Array	UF300	*Without lens*	*With lens*
No. of elements	64	Pulse duration ($\tau_{(-20\ dB)}$)	0.96 μs	1.5 μs
Pitch	0.80 mm	Center frequency	3.2 MHz	2.7 MHz
Kerf	0.051 mm	Frequency bandwidth Range f_1 - f_2 (-6 dB)	2.4 – 4.0 MHz	2.1 – 3.5 MHz
Elevation	18 mm	Focus position	95.8 mm	60.8 mm
Elevation ROC	100 mm	Depth of focus (-6 dB)	96.5 mm	35.2 mm
		Elevation Beam width, ΔY (-6 dB)	2.5 mm	1.2 mm
		Lateral Beam width, ΔX (-6 dB)	53.6 mm	28.8 mm

II.4.5.2 Ultrasonic data pre-processing

The system specific correction and muscle acoustic parameter estimations were carried out off-line. The muscle region of interest (ROI) was selected from B-mode images containing raw data. The correction steps applied to the time-gated pulse-echo signals prior to the spectral and cepstral parameter estimations are described in the following sections. The time-dependent amplification (TGC) was compensated to ensure a uniform amplification within the entire focus range [170].

II.4.5.3 Sound field correction (SFC)

The signal amplitude of reflected and backscattered waves varies with respect to the distance from the focal plane. A time-of-flight based defocus correction was used to calibrate the system in water at 37 °C [27;171;172]. Briefly, the reflections of a plane 4-wt% agar reflector were recorded at successively increasing distances to the transducer. Mass density and sound velocity in the agar phantom were $\rho_{agar} = 1.003$ gcm^{-3} and $v_{agar} = 1542$ ms^{-1}, respectively. The measured confocal reflection amplitude was estimated to be -35 dB smaller than that of a perfect reflector.

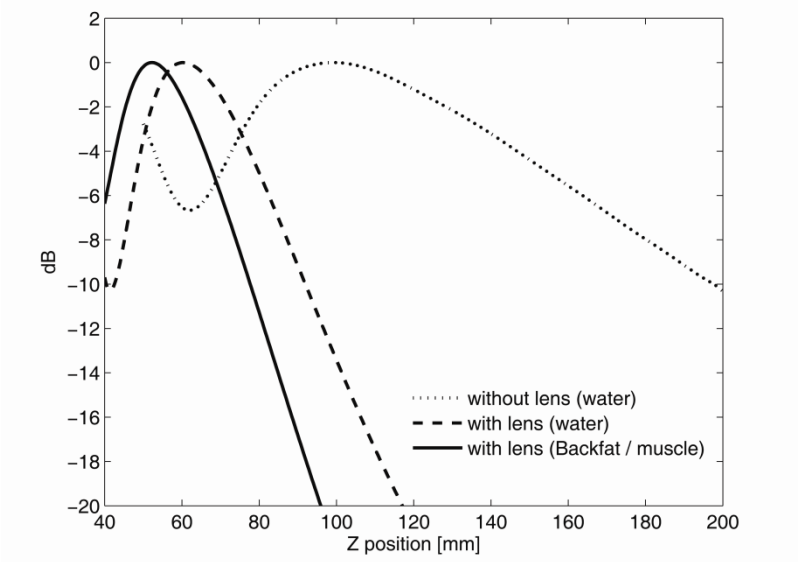

Figure II.30 *Sound field plots along the depth with and without acoustic lens.*

Because the sound velocities in skin, back fat and muscle are different compared to those in water, the focus position is shifted in the carcass (Fig. II.30). To compensate for this effect, a refraction correction based on the average sound velocities and thicknesses in the skin-back fat compound and in muscle has been applied [173]. The back fat compound thickness, $d_{BFcompound}$ and speed of sound, v_{BFcomd} were estimated using their relation (Eq. (II.21)) found *in vitro* study (Sec.II.B.4) from the automatically detected time of flight to the back fat-muscle boundary, TOF_{BFcomd} using an iteration method.

$$v_{BFcomd} = 1555m/s - 3.94\, mm^{-1}ms^{-1}d_{BFcomd} \quad \text{(II.21)}$$

Briefly, d_{BFcomd} is calculated using initial v_{BFcomd} = 1491 m/s [Mean v_{BF} from all 54 samples] with back fat time of flight ($TOF_{BFcomd} = TOF_{skin} + TOF_{outer\ fat} + TOF_{middle\ fat} + TOF_{inner\ fat}$). This result d_{BF} is used in the above relation (Eq. (II.21)) to predict v_{BFcomd}. This procedure is repeated until the differences between consecutive back fat SOS ($v_{BFcomd}^{k+1} - v_{BFcomd}^{k}$) are less than 0.1 m/s. Finally, v_{BFcomd} and d_{BFcomd} were determined from TOF_{BFcomd} using this iteration method.

The average sound velocity in muscle v_{muscle} has been found to be 1620.5 ± 4.6 ms^{-1} within the evaluated carcasses [120]. A weak correlation with IMF (R^2 = .13; RMSE = 4.33 ms^{-1}) was also found in that study. This variation had no remarkable effect on the refraction correction. Therefore, only the mean velocity was included in our correction model.

The distance z from the transducer of a gated signal within the muscle region was estimated using the relation:

$$z_{muscle} = d_{BFcomd} + \left(TOF_{Gateposition} - TOF_{BFcomd/Muscle}\right) . \frac{v_{muscle}}{2} \qquad \text{(II.22)}$$

It can be seen in Fig. II.30 that the axial intensity distribution in the back fat muscle compound is shifted towards the transducer compared to that in water. The Field II simulations were used to estimate the axial shift. Then the pulse echo measured in water at z_{ref} that exhibits the same decrease of intensity (relative to the focal plane) as that estimated for z_{muscle} was used as a reference signal at $TOF_{Gateposition}$ for further calculations.

II.4.5.4 Wave front curve compensation (WFCC)

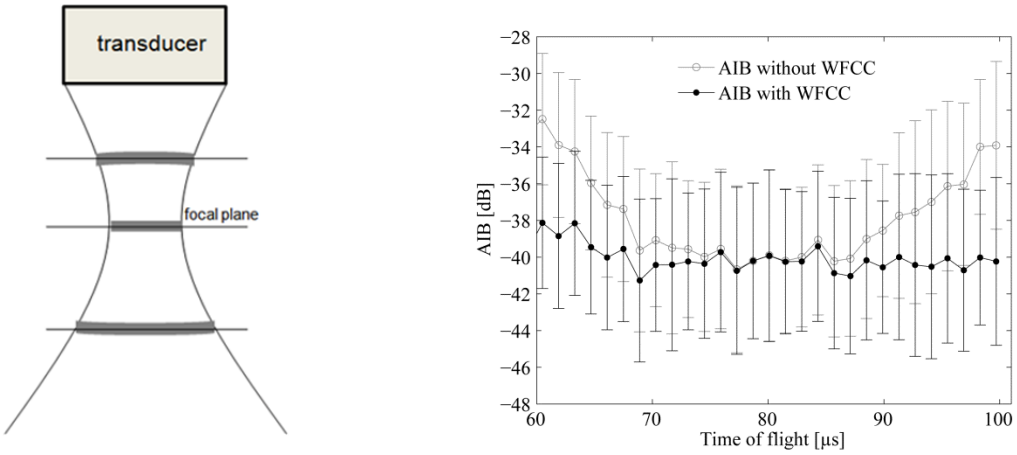

a) *b)*

Figure II.31 *a) Focused beam projection along propagation direction and b) AIB in phantom with and without wavefront curve compensation.*

Due to the curvature of the wave front of the focused sound field, reflections of a plane reflector exhibit a further phase cancellation with increasing distance from the focal plane. Therefore, the decrease of the measured amplitude of a plane reflector, with respect to the defocus distance, is larger than that measured from backscattered signals collected at the corresponding time gates. This amplitude deviation between signals reflected from a plane agar reflector after SFC correction and those backscattered within the corresponding time gate $TOF_{Gateposition}$ was assessed by measurements in a tissue mimicking agar phantom. This phantom was made of graphite powder immersed in agar as described by [166]. The phantom was measured using the same device settings as for the muscle measurements and it was attached directly to the transducer surface. Fig. II.31b shows the apparent integrated backscatter amplitude *AIB* as a function of the defocus distance with sound field and intermediate medium attenuation compensations. For a proper sound field correction, *AIB* is supposed to decrease linearly with increasing depth. Due to the curvature of the focused beam (Fig. II.31a) before and after the focal plane, the estimated *AIBs* increased with increasing distance from the focal plane (Fig. II.31b). This wavefront curve deviation was corrected from this known phantom's normalized AIBS deviation along the depth (Fig. II.31b).

II.4.5.5 Attenuation compensation

The sound waves are attenuated on the two-way travel from the transducer surface to the muscle region of interest. Further losses arose from partial reflections at tissue boundaries. Refraction of the sound field and attenuation after propagation through skin and back fat were estimated using sound velocity and attenuation values assessed in a previous study [168]. The muscle attenuation α_{muscle} within the ROI was estimated using a sliding window technique as proposed by [174;175]. For this, all 64 spectra were averaged for each $TOF_{Gateposition}$ and the slope of the frequency dependent attenuation was assessed by linear regression. Finally, the attenuation of the overlaying back fat tissue α_{BF} was compensated. For this, the mean value of α_{BFcomd} = 2.1 dBMHz^{-1}cm^{-1}, assessed in a previous study, was used [168].

II.4.5.6 Spectral parameter estimation

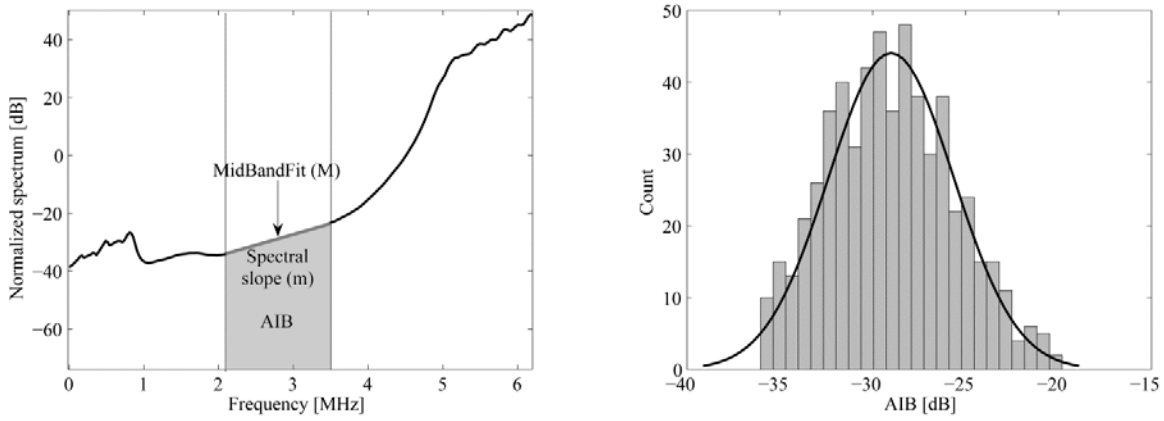

Figure II.32 *a) Estimation of spectral parameters from the normalized power spectrum. b) AIB histogram distribution within the evaluated muscle region of interest.*

Backscatter properties of muscle tissue were assessed within a ROI 54 mm x 15 mm (i.e. the axial -6dB range from 45 to 59 mm). The normalized power spectra *S(f)* were calculated after the above mentioned corrections, as follows.

First, a part of the signal was gated using a sliding Hanning window. The positions of the first and last windows were placed 10 mm above and 7 mm below the estimated focus position respectively. The gate width was equivalent to the 2-fold pulse duration (3 µs), which corresponds to a depth range of ~ 15 mm assuming a sound velocity of 1620 m/s in muscle. The overlap between adjacent sliding gate windows was set to 50%. The logarithmic power

spectrum was normalized to the reference spectrum obtained from the plane agar reflector, after SFC, WFCC and AC correction. Spectra intensity within the frequency bandwidth below -40 dB (close to noise level) was excluded. The excluded RF signal percent was stored as one of the parameters. The normalized spectra determined from remaining RF signals were averaged within the entire ROI. *AIB* was calculated in the frequency range between 2.1 MHz and 3.5 MHz (Fig. II.31):

$$AIB = \frac{1}{\Delta f}\int S(f,z)\,df \tag{II.23}$$

Midband fit *M* and spectral slope *m* were calculated as described elsewhere [75] and illustrated in Fig. II.31a.

II.4.5.7 Cepstral parameter estimation

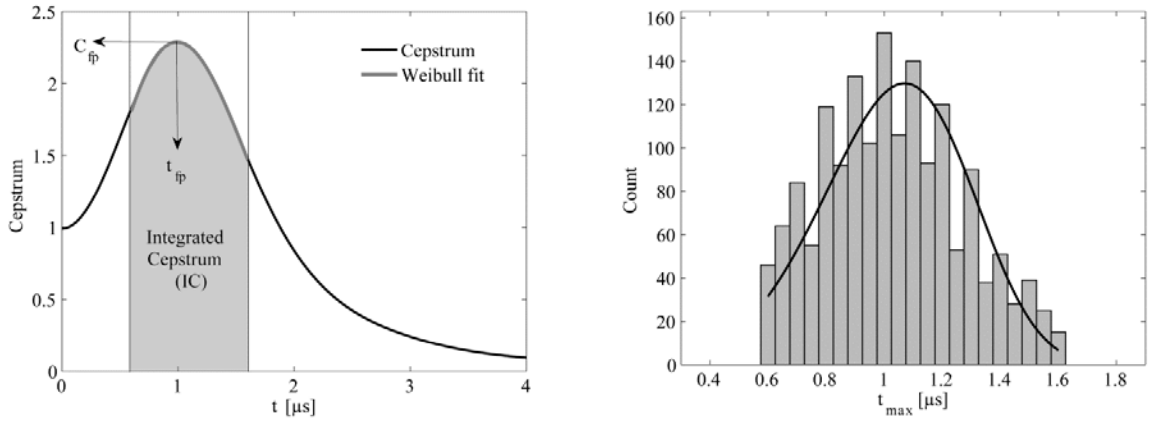

a) *b)*

Figure II.33 *a) Cepstral parameters estimation. b) Cepstral parameter, τ_p distribution within region of interest with Weibull fit.*

The power cepstral data analysis can be described as the Fourier transform of the power spectral density of a time signal [84]:

$$C(\tau) = \left|FT\left((log_{10}|S_{muscle}(f)|^2) - \left(log_{10}\left|S_{ref}(f)\right|^2\right)\right)\right|^2 \tag{II.24}$$

where $S_{muscle}(f)$ and $S_{ref}(f)$ are the Fourier transforms of the time-gated backscatter signals of the muscle and the reference respectively. Cepstral peaks correspond to the occurrence and time delay of several echoes within the time gate. Further restrictions are that the time delay should be larger than the pulse length, and the analysis is only meaningful within the spectral bandwidth of the ultrasound system [176]. The window length was 5 times the pulse width and the overlap was set to 90%. Only the SFC and WFCC corrections were applied for the cepstral analysis. Prior to the FT the difference spectrum was preconditioned by removing DC and linear components. Similarly to the spectral analysis, signals with cepstral amplitudes below -40 dB were excluded. The cepstral first peak intensity value $C_{fp}(\tau_{fp})$, the corresponding time-delay τ_{fp} and its standard deviation were calculated by fitting averaged cepstrum by Weibull function (Fig. II.33a). The integrated cepstrum *IC*:

$$IC = \frac{1}{\Delta\tau}\int C(\tau)\, d\tau \tag{II.25}$$

within the interval $\Delta\tau$ from 0.6 – 1.6 were calculated from the averaged cepstra (Fig. II.33a).

II.4.6 Statistical Methods

In muscle studies, the normality of the distribution was tested with the Lilliefors test. Linear regression and Pearson correlation coefficients were used to study the association between muscle composition, structural parameters and estimated acoustic parameters. To investigate the variation of acoustic parameters of muscle function of fiber orientations, Two-way ANOVA followed by *post hoc* multiple comparison Tukey tests were performed. The Bland and Altman method [177], linear regression and Pearson correlation coefficients were used to compare tissue composition and structural parameters from the ultrasonic measurement and chemical analysis. Optimal combination of estimated spectral and cepstral parameters for predicting the intramuscular fat percentage were evaluated using multifactorial linear and nonlinear regression. All the statistical computations were made using the MATLAB Statistics Toolbox (The Mathworks Inc., Natick, MA, USA).

III Results

III.1 Cortical Bone

III.1.1 Accuracy of elastic coefficient estimation

In order to verify that the curved surface of a cylindrically shaped sample does not have an effect on the measured reflection amplitude, the defocus dependent reflection amplitude of a homogenous reference material (PMMA) was compared for flat and cylindrically shaped samples (Fig. III.1). Within the accepted defocus range no significant difference of the TOF-dependent reflection amplitude was observed.

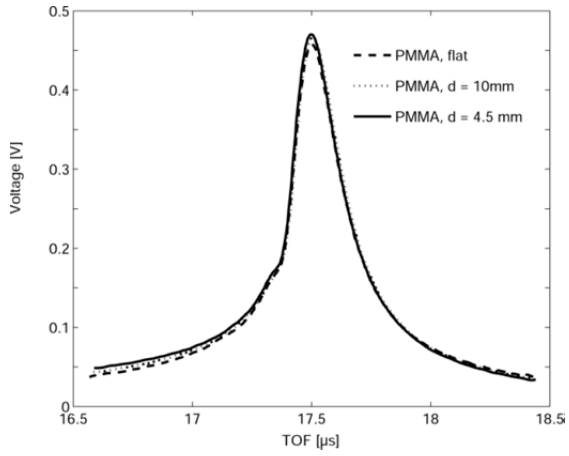

Figure III.1 *Comparison of the defocus – dependent reflection amplitude of PMMA for flat and cylindrically shaped samples.*

Accuracy and reproducibility of the impedance estimation was estimated by measuring 6 bone samples 2 times on different days. The average relative reproducibility error of the estimated mean impedances given by the root mean square average of the 6 relative standard deviations was 0.95%. The accuracy of the estimation of the angle θ_0 was in the order of ± 0.48°. The correlation coefficients R^2 for the fit of the transverse isotropic model to $C(\theta)$ was between 0.97 and 0.99 (Fig. III.2).

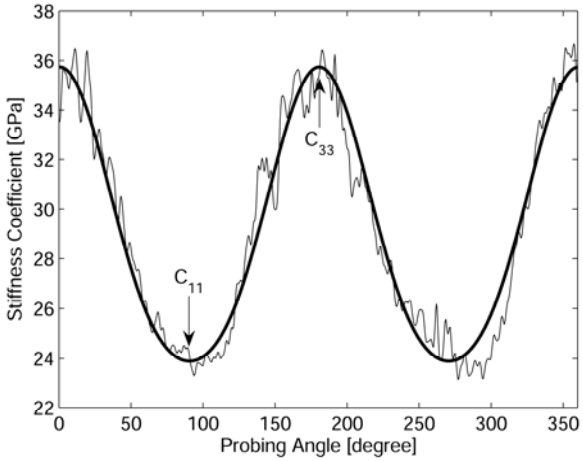

Figure III.2 *Example of a fit of the measured data to a transverse isotropic model. The correlation coefficient was $R^2 = 0.979$ [36].*

The impedance values measured from flat and cylindrical femur samples were also compared. The average impedance values for flat and cylindrical samples were $Z_{cross} = 7.96 \pm 0.32$ Mrayl and $Z_{33} = 8.02 \pm 0.37$ Mrayl (impedance at 0°) for the longitudinal direction, $Z_{trans} = 6.69 \pm 0.18$ Mrayl and $Z_{11} = 6.69 \pm 0.22$ Mrayl (impedance at 90°) for the circumferential direction respectively. The average relative difference for the longitudinal and circumferential direction impedance values were (6.3 ± 21.4) % and (0.5 ± 16.9) %, but these differences were not significant (paired t-test for 0°, $p = 0.19$ and for 90°, $p = 0.76$).

III.1.2 Relation between acoustic impedance, mass density and elastic coefficients

Fig. III.3 shows the relation of Z and ρ with elastic coefficients *c* for site-matched data obtained from cylindrical human femur cortical bone samples. It can be seen that Z is generally a better predictor for the elastic properties of material than mass density. While the correlation coefficient of a power fit of mass density with elastic coefficients was weak ($R^2 = 0.19$ *(with* c_{33}*)*, $R^2 = 0.03$ *(with* c_{11}*)*, the acoustic impedance correlates almost perfectly with elastic coefficients ($R2 > 0.99$, $p < 0.0001$). This is consistent with the fact that the correlation between DMB and *Z* was also moderate ($R^2 = 0.39$) which indicates that *Z* yields elastic information independent of DMB.

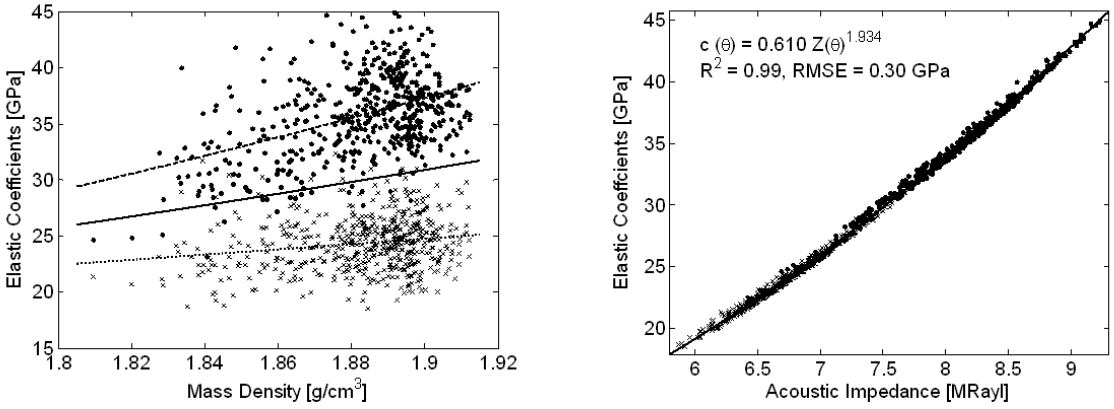

Figure III.3 *Relations between acoustic impedance, mass density and elastic stiffness for human femoral cortical bone (dashed line: fit for axial elastic coefficients c_{33} (•), dotted line: fit for radial elastic coefficient c_{11} (x), solid line: fit for combined data).*

III.1.3 Spatial distribution of microscopic elastic properties

Fig. III.4 shows the unwrapped impedance images of the evaluated samples taken from the four anatomical quadrants of the cross section at 44.5% of femur length. All the impedance images are aligned like the periosteal surface was always at the bottom of the images. The highest impedance values always occur around 0° and 180°. At these angles the Haversian canals are predominantly cut perpendicular to their long axes. Hence, they appear as circular or elliptical structures. At 90° and 270° the impedance values are low and the Haversian canals appear as elongated structures. It can be seen that osteonal tissue surrounding the Haversian canals has lower impedance values compared to interstitial tissue. Moreover, the absolute impedance values and also microstructural features vary considerably between the four samples.

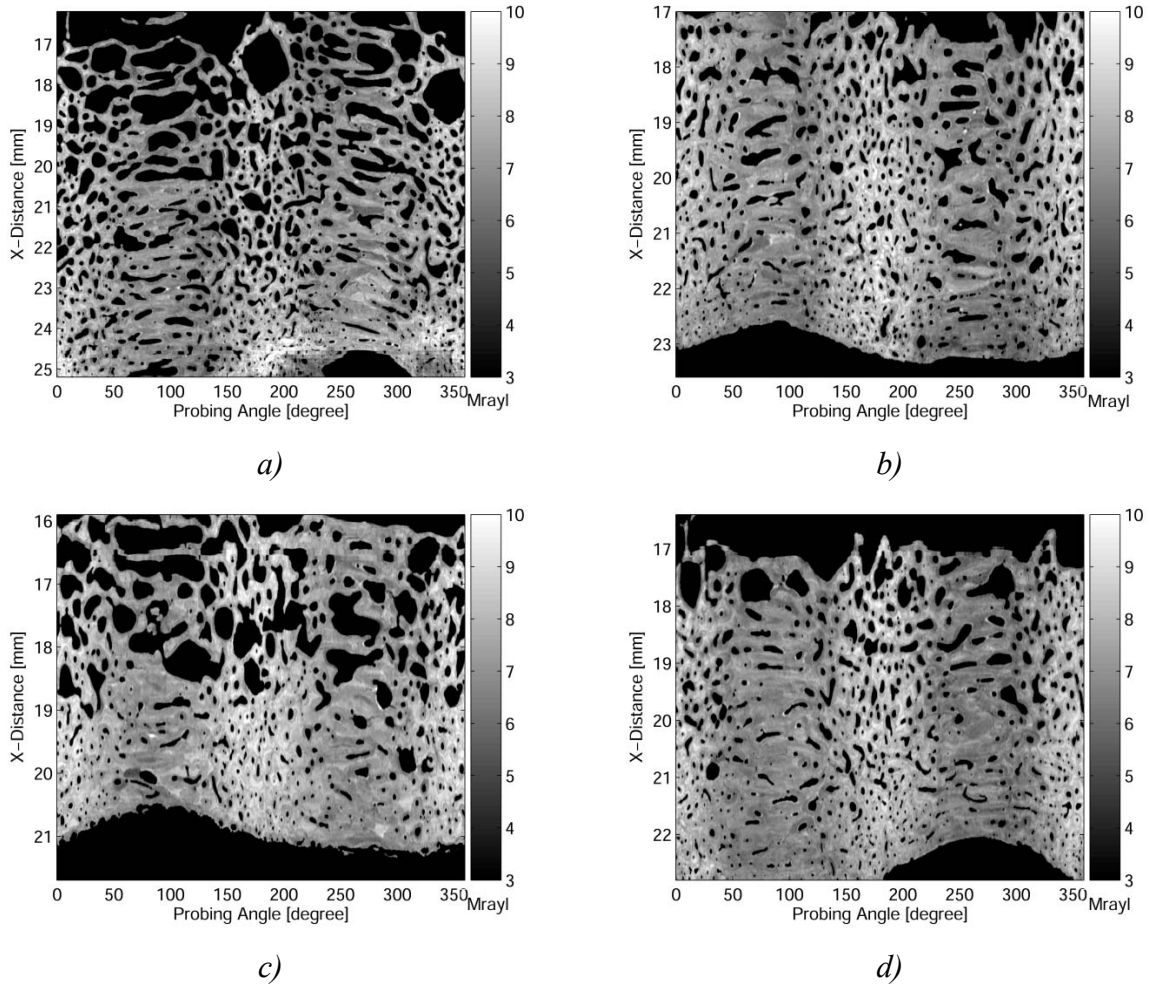

Figure III.4 *Unwrapped acoustic impedance images of the cylinder surfaces taken from four anatomical quadrants: a) posterior, b) medial, c) anterior and d) lateral of cross section at 44.5% of femur length after the segmentation process (all excluded pixels are black). The periosteal surface is always at the bottom of the images.*

The transverse isotropic elastic coefficients were determined for 56 (14 x 4) cylindrical samples. The spatially averaged values of bone tissue matrix coefficients and technical constants from an entire human femur are listed in Table II.2.

Table III.1 *Mean and standard deviation of all microscopic elastic coefficients and technical constants.*

Average elastic coefficients		Average technical constants	
c_{33}	34.6 ± 3.6 GPa	E_3	27.4 ± 3.0 GPa
c_{11}	24.1 ± 2.0 GPa	G_{13}	7.0 ± 1.1 GPa
c_{12}	10.2 ± 0.8 GPa	γ_{12}	0.324 ± 0.024
c_{13}	11.1 ± 0.8 GPa	γ_{13}	0.219 ± 0.012
c_{44}	7.0 ± 1.2 GPa	γ_{31}	0.323 ± 0.013

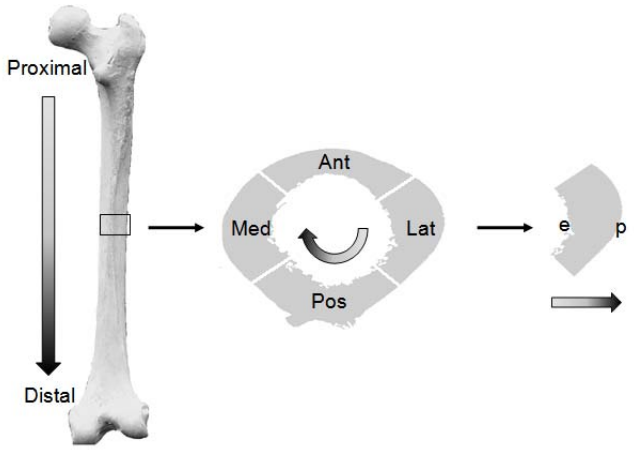

a) *b)* *c)*

Figure III.5 *The elastic properties of human femoral shaft were analyzed in three positional directions: a) along the longitudinal direction (from proximal to distal), b) along the circumferential direction (in the order: posterior, medial, anterior and lateral) and c) along the radial direction (from endosteum to periosteum).*

The elastic properties of the human femoral shaft were analyzed in four ways (Fig. III.5): 1) mean elastic coefficients along longitudinal positions (along femur length, from proximal to distal); 2) variation of elastic coefficients along longitudinal positions for each anatomical quadrants: 3) mean elastic coefficients along circumferential directions (posterior, medial, anterior and lateral); and 4) variation of elastic coefficients along radial directional positions (along cortical width, from endosteum to periosteum).

Table III.2 *Three-way ANOVA for microscopic elastic coefficients (F – statistic). Categorical factors are: Long axis position (Long – Proximal to Distal), Circumferential position (Circ – posterior, medial, anterior and lateral) and Radial position (Radi – endosteal to periosteal).*

	c_{33}	c_{11}	c_{12}	c_{13}	c_{44}
Long	10.42 *	11.76 *	10.42 *	10.42 *	9.09 *
Circ	14.53 *	6.04 *	14.49 *	14.44 *	7.39 *
Radi	10.42 *	8.12 *	10.41 *	10.38 *	2.83
Long x Circ	13.70 *	7.83 *	13.71 *	13.72 *	8.27 *
Long x Radi	0.22	0.62	0.22	0.22	0.47
Circ x Radi	0.32	0.44	0.32	0.32	0.66

*represents the significant difference at the level 0.05

Three-way ANOVA of elastic constants with the long axis, anatomical and radial positions as categorical factors showed that all directional positions contribute significantly to the variances of all elastic coefficients (Table II.2). Moreover, the second-order interaction terms between the long axis position and the circumferential position suggest that the all elastic coefficients along anatomical positions are also dependent on the femoral long axis position. The interaction terms long*Radi and Circ*Radi are not significant for all elastic constants.

III.1.3.1 Microscopic elastic coefficients along the longitudinal direction

The mean microscopic elastic coefficients variations along the femur long axis positions are given in Fig. III.6. The strongest dependence on the axial position was found for c_{33}, c_{12} and c_{13}. Linear increase of the coefficients ($R^2 = 0.73$, $p < 0.05$) from section 25.7% to 80.7% of the femur length were observed. The other coefficients showed lower values in the mid- shaft region (40 – 60%) than in the sections close to the distal, and had a lower correlation with axial positions ($R^2 \approx 0.23$). The c* values increased along the femur long axis ($R^2 = 0.35$).

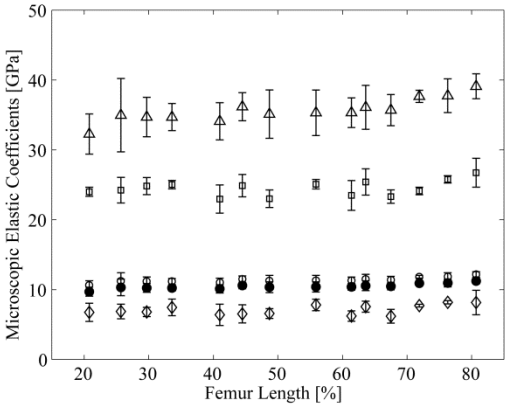

Figure III.6 *Mean tissue elastic coefficients c_{33}(Δ), c_{11}(□), c_{12}(•),c_{13}(o) and c_{44}(◊) along the femur long axis.*

The variations of all elastic coefficients for four anatomical quadrants along the femur long axis are shown in Fig. III.7. In the posterior quadrant, all the elastic coefficients, c_{33}, c_{11}, c_{12} and c_{13} (R^2 = 0.49 - 0.73), except for $c_{44,}$ showed linear increase along the long axis from proximal to distal sections. In the anterior quadrant, all elastic coefficients except c_{44} showed similar variation along the longitudinal direction, those values are higher below the mid shaft than the regions above the mid shaft region. The significant changes in the medial region along the femur long axis were observed only in elastic coefficients c_{33}, c_{12} and c_{13}. In the lateral quadrant, the coefficients c_{33}, c_{12} and c_{13} increased linearly along the long axis and were higher in the sections close to the distal. The coefficient c_{11} was lower in the middle region than the sections close to proximal and distal. Proceedings distally, the axial elastic coefficient, (c_{33}) values of the four quadrants appears to converge. It is interesting to note that the c_{33} of the anterior quadrant was significantly higher in the most proximal section and lower in the most distal section than the three other quadrants. In contrast to this, the c_{11} of the posterior quadrant was significantly lower in the most proximal section and higher in the most distal section than the three other quadrants. The ranges of all elastic coefficients for the four anatomical quadrants along the femur long axis are listed in Table II.3. The experimentally predicted c^* has moderate correlation with the femur long axis position in both posterior (R^2 = 0.39) and lateral (R^2 = 0.37) quadrants. In posterior and medial, there were not significant changes of c^* from proximal to 65% and then increasing to distal.

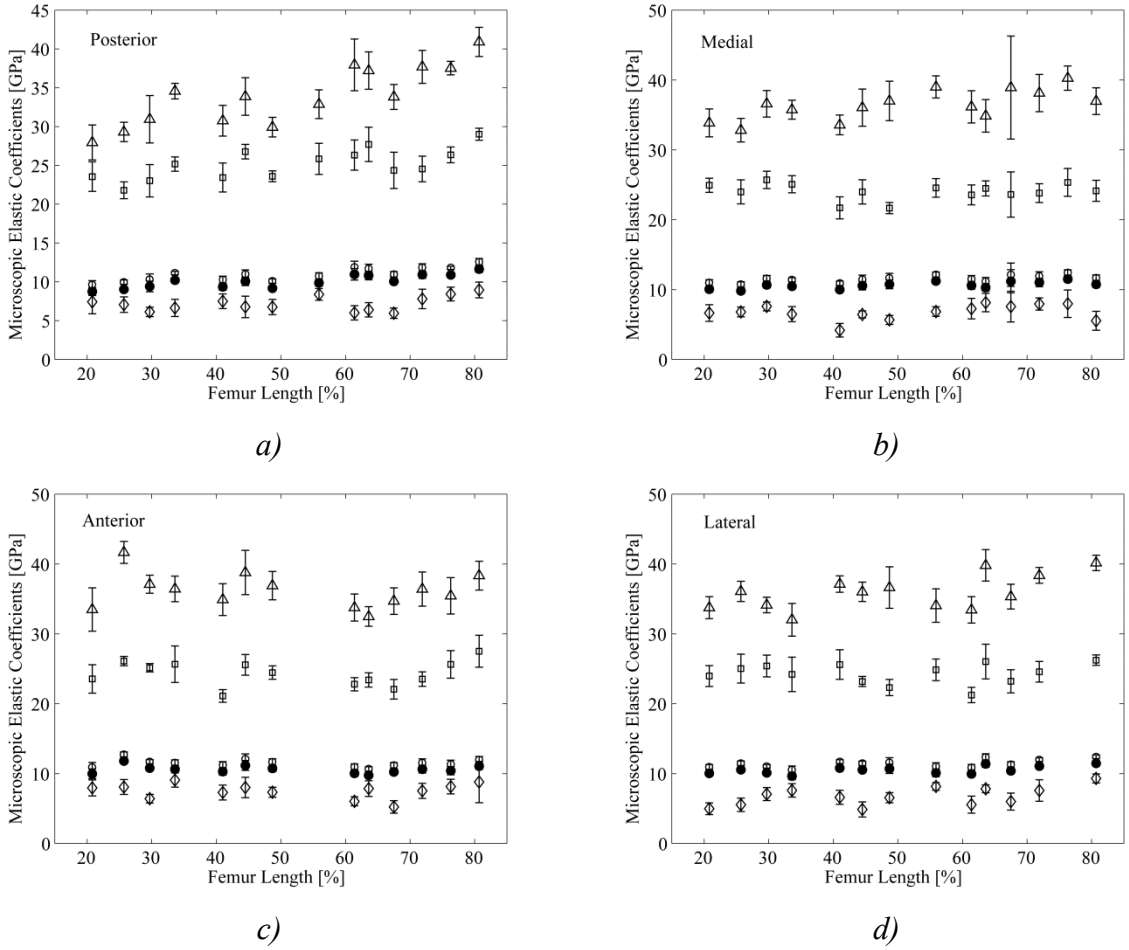

Figure III.7 *Mean microscopic elastic coefficients c_{33}(Δ), c_{11}(□), c_{12}(●), c_{13}(o) and c_{44}(◊) for four quadrants: a) posterior, b) medial, c) anterior and d) lateral along femur length.*

Table III.3 *The ranges of microscopic elastic coefficients in anatomical positions along the long axis of femur cortical bone.*

Anatomical position	c_{33} (GPa)	c_{11} (GPa)	c_{12} (GPa)	c_{13} (GPa)	c_{44} (GPa)
Posterior	27.95 – 40.91	21.79 – 29.01	8.73 – 11.64	9.64 – 12.57	5.96 – 8.95
Medial	32.81 – 40.26	21.66 – 25.69	9.82 – 11.49	10.74 – 12.43	4.17 – 8.13
Anterior	32.48 – 41.66	21.11 – 27.51	9.75 – 11.81	10.66 – 12.74	5.21 – 9.08
Lateral	32.01 – 40.15	21.24 – 26.23	9.64 – 11.47	10.56 – 12.39	4.86 – 9.30

III.1.3.2 Microscopic elastic coefficients along the circumferential direction

Figure graphically represents the mean elastic constants for four anatomical quadrants. Tukey's multiple comparison test at the 0.05 significant level shows that the posterior quadrant has lower axial coefficient, (c_{33}) than the other four quadrants. It has higher c_{11}, c_{12} and c_{13} values than the other quadrants. Anterior has higher c_{44} and c^* values than the other three quadrants.

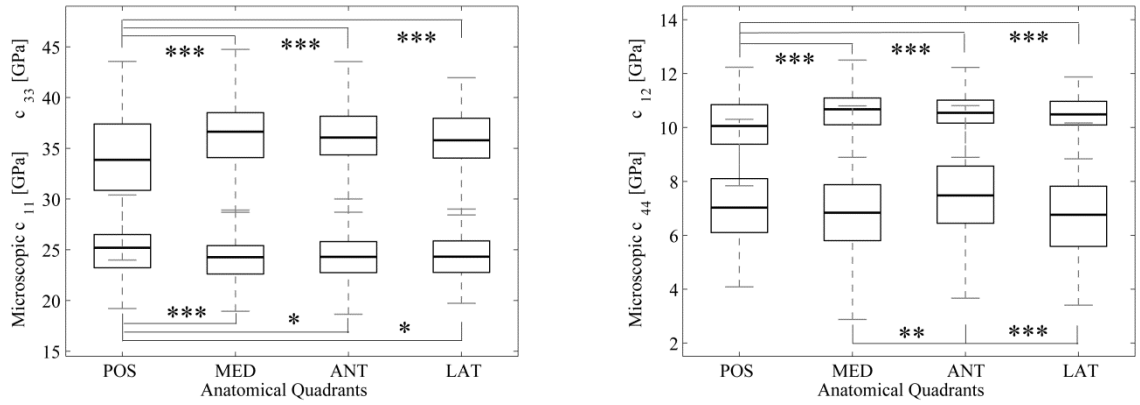

Figure III.8 *Graphical representations of the mean microscopic elastic coefficient, a) c_{33} and c_{11} and b) c_{12} and c_{44} for anatomical quadrants(* p<0.05, ** p<0.001 and *** p<0.0001).*

III.1.3.3 Microscopic elastic coefficients along the radial direction

The variations of elastic coefficients were also considered with respect to the radial position (Fig. III.9). For this, the acoustic impedance data of all anatomical quadrants were divided into 10 sections from endosteum to periosteum and the elastic coefficients were estimated separately for each section. The mean elastic coefficients along the radial position are given in (Fig. III.9). Here, 10% corresponds to the section close to the endosteum and 100% to the section close to the periosteal. c_{33}, c_{12} and c_{13} increased from the endosteum towards the central part of the cortex. The maximum is reached between 50 and 70% of the cortical width. Between 70% and the periosteum the values decreased again. However, c_{11} c_{44} and c^* did not vary from the endosteum until the central region (~ 60%) and decreased from the central region towards the periosteum.

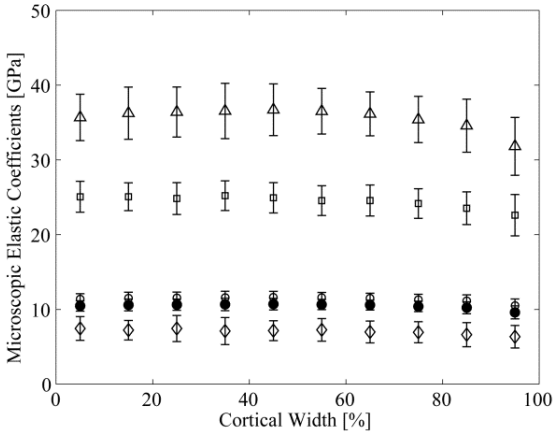

Figure III.9 *Mean and standard deviation of microscopic elastic coefficients c_{33} (Δ), c_{11}(□),c_{12}(●),c_{13}(○) and c_{44}(◊) along the radial direction (5% and 95% correspond to the sections adjacent to the endosteum and the periosteum, respectively).*

III.1.3.4 Microscopic anisotropy ratio

The anisotropy ratio ($AR = c_{33}/c_{11}$) varied with respect to the long axis and anatomical positions (Fig. III.10a and Fig. III.10b). Along the long axis position, the mean anisotropy ratio increased linearly from proximal to distal sections and has moderate correlation (R^2 = 0.38, $p < 0.05$). The mean and range of the microscopic anisotropy ratio are 1.46 ± 0.14 and 1.35 – 1.57. There were moderate correlations between the microscopic anisotropy ratio and the femur long axis position for posterior, medial and lateral quadrants. Within the anatomical quadrants, the anterior has higher values of AR close to the proximal sections and the medial has higher values of AR close to the distal sections than other quadrants. The mean ARs were lower in the posterior quadrant than in the other quadrants (Fig. III.10b). The mean microscopic AR values for anatomical quadrants; posterior, medial, anterior and lateral are 1.35 ± 0.09, 1.52 ± 0.11, 1.49 ± 0.09 and 1.48 ± 0.09. Significant difference in AR along the radial direction was found. However, the plot (Fig. III.10c) shows that the radial direction AR increased from the endosteum to 55% of the cortical width and then decreased towards the periosteum, and also the values are higher at the region close to the endosteum than the periosteum.

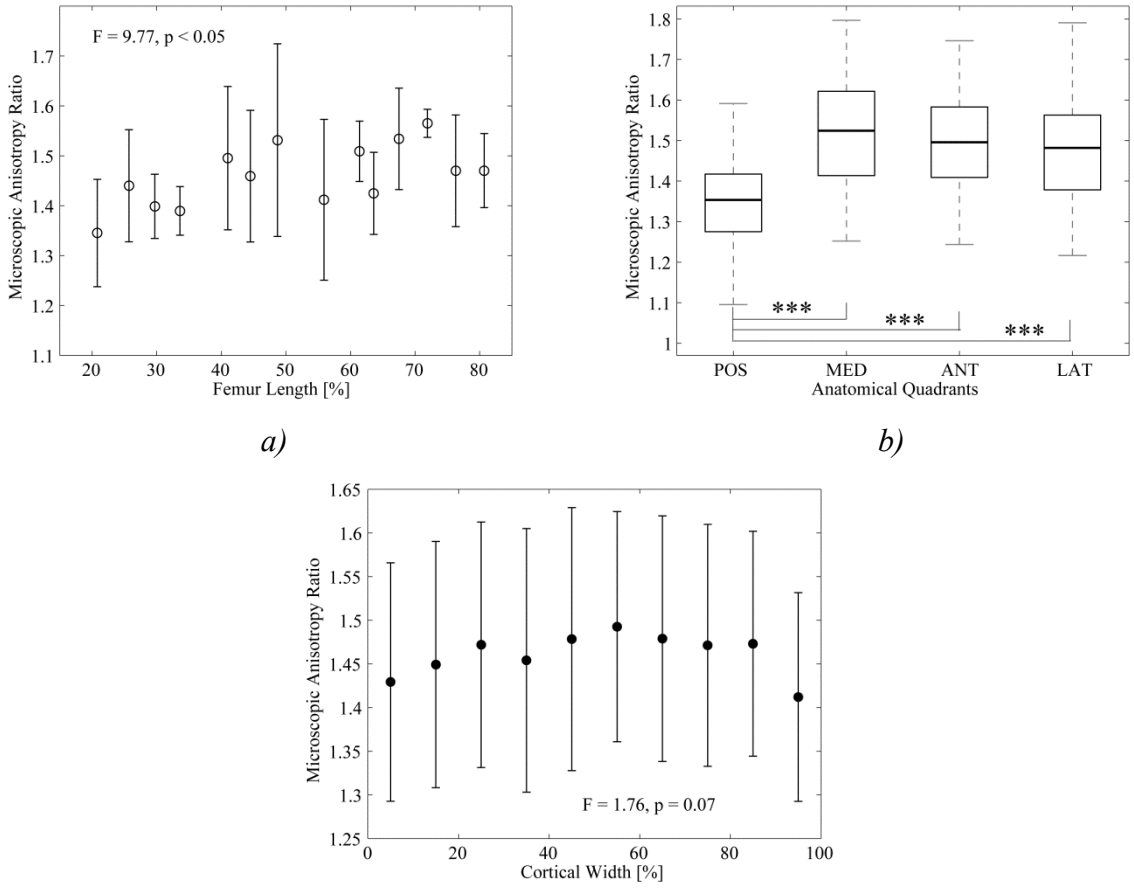

Figure III.10 *Variation of tissue level anisotropy ratio of human femur along a) longitudinal, b) circumferential and c) radial directions* **(* p<0.05, ** p<0.001 and *** p<0.0001).**

III.1.4 Spatial distribution of structural properties

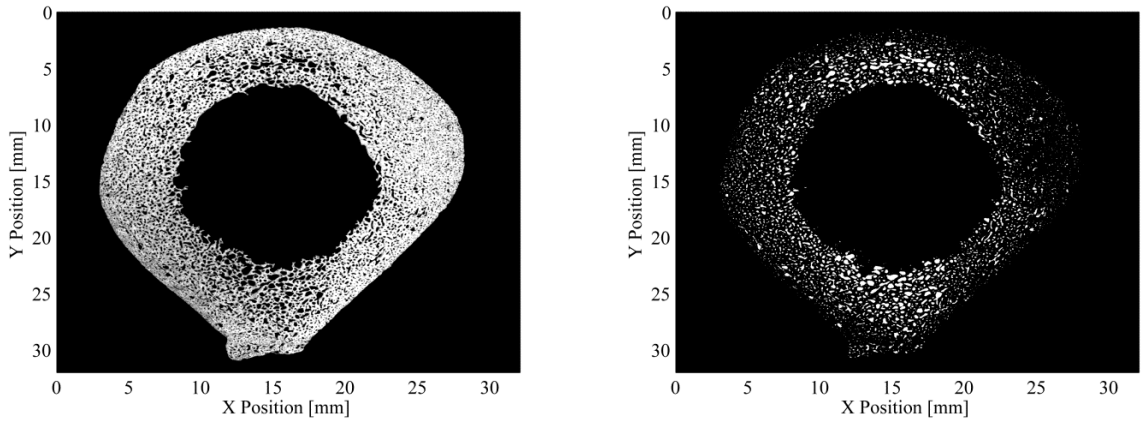

a) *b)*

Figure III.11 *a) Acoustic impedance image and b) pore distribution of femur cross section sample from 33.6% of femur.*

The structural parameters of the human femoral shaft were analyzed in three ways: 1) mean structural parameters variation along the long axis direction from proximal to distal; 2) variation of structural parameters along the long axis position for each anatomical quadrant; and 3) mean structural parameters variation along anatomical quadrants (posterior, medial, anterior and lateral).

Table III.4 *Two–way ANOVA for structural parameters (F – statistic). Categorical factors are: Long axis position (Long) and Circumferential direction position (Circ).*

	Cortical Width	Porosity	Canal Diameter	Canal Density
Long	14.8 *	0.51	0.83	5.91 *
Circ	1.72	5.23 *	6.28 *	2.04
Long x Circ	1.36	3.44 *	2.99 *	0.47

*represents the significant different at the level 0.05

Two–way ANOVA of structural parameters: porosity, canal diameter and canal density with long axis and anatomical position as categorical factors are shown in Table III.4. The cortical width and canal density have a significant difference along the long axis position and both porosity and canal diameter varied with respect to anatomical quadrants. There was also

significant interaction presented in porosity and pore diameter between quadrants and femur along axis positions.

III.1.4.1 Variation of structural parameters along the longitudinal direction

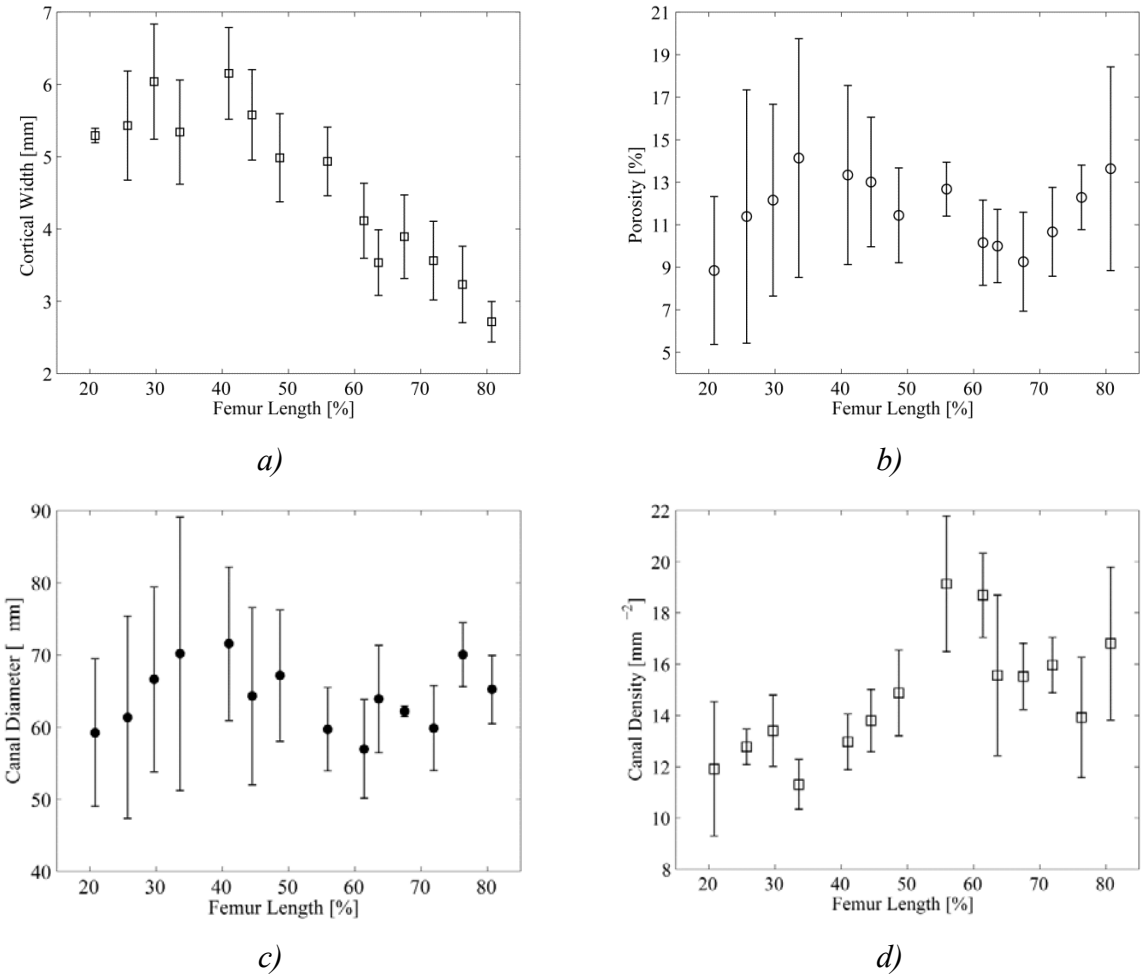

Figure III.12 *Mean structural parameters along the longitudinal direction a) cortical width, b) porosity, c) canal diameter and d) canal density.*

Variations of structural parameters along the femur long axis are shown in Fig. III.12. The cortical thickness reached a maximum at sections 40% of femur length and decreased to very low values proceeding distally. ANOVA did not show any significant difference of porosity and canal diameter along the long axis. However, the Fig. III.12 shows that the variations of porosity and canal diameter are similar along the long axis and have partial linear correlation (R^2=0.36). Both the values increased from the proximal region and reached a maximum at 30-40%, decreased to 60-70% and then increased to proximal region. The mean pore density increased linearly from 25% and attained a maximum at 55%, then

decreased in the distal region. This canal density has a partially negative linear correlation with canal diameter (R^2=0.29).

The structural parameters variations for all anatomical quadrants along the long axis were also analyzed. Variations of cortical thickness were similar for all anatomical quadrants along the long axis direction. In the posterior quadrant, porosity decreased linearly from proximal to distal (R^2=0.94, p<0.0001). There were no changes in porosity in the medial region. In the lateral, porosity has a moderate increasing correlation with the long position (R^2=0.44, p<0.05). Posterior has a lower canal diameter (≈ 53 μm) in the sections below 40% than above 40% of femur length (≈ 63 μm). But in the medial quadrant, the variation is the reverse; the cross section below 50% femur length has higher canal diameter (≈ 80 μm) than above 50% (≈ 65 μm). Most distal sections (60–80%) had similar diameter values for all quadrants. The canal density increased linearly in both posterior (R^2=0.69) and lateral (R^2=0.36) quadrants along the long axis. The variations of canal density were similar for medial and anterior quadrants along the long axis and have the maximum values in the cross section for 61.4 % of femur length. The ranges of structural parameters along the long axis for all anatomical quadrants are listed in Table II.5.

Table III.5 *The ranges of structural parameters in anatomical quadrants along the long axis of femur cortical bone.*

Anatomical Quadrant	Cortical Width (mm)	Porosity (%)	Canal Diameter (μm)	Canal Density (mm^{-2})
Posterior	3.02 – 5.52	9.25 – 19.15	51.06 – 70.24	8.01 – 18.94
Medial	2.75 – 7.16	9.20 – 12.94	57.45 – 90.83	10.90 – 17.84
Anterior	2.35 – 5.81	5.72 – 18.33	51.06 – 81.24	10.19 – 21.15
Lateral	2.75 – 6.77	6.89 – 19.94	51.06 – 72.23	12.39 – 21.91

III.1.4.2 Variation of structural parameters along the circumferential direction

ANOVA test shows that only porosity and canal diameter have a significant difference along the anatomical positions. The graphical representations of porosity and pore diameter for anatomical quadrants are shown in Fig. III.13. Posterior has a higher porosity than the anterior and lateral quadrants. Canal diameters are higher in the medial quadrants than the posterior and lateral quadrants.

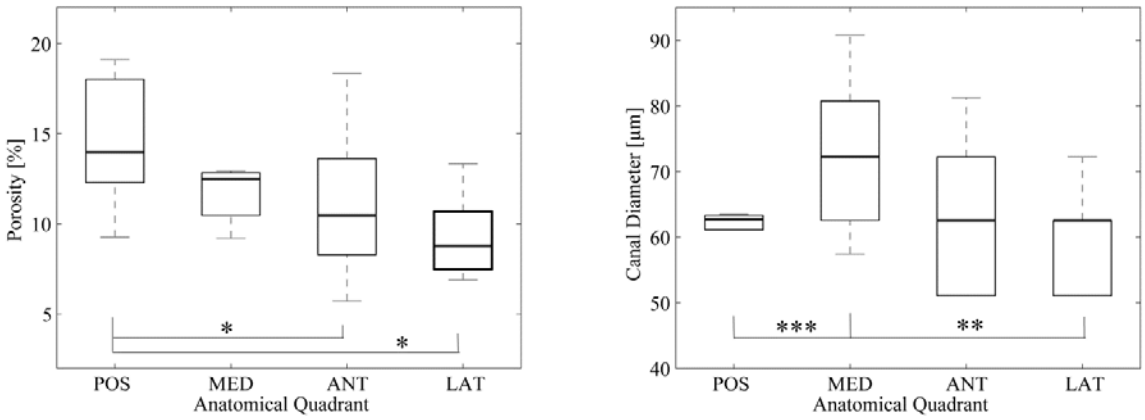

a) *b)*

Figure III.13 *Graphical representations of structural parameters, a) porosity and b) canal diameter along the circumferential direction (* p<0.05, ** p<0.001 and *** p<0.0001).*

Along the radial positions, all the cross section samples showed higher porosity and pore diameter to regions close the endosteum than the regions close to the periosteum (Fig. III.11b).

III.1.5 Spatial distribution of homogenized mesoscopic elastic properties

Using the asymptotical homogenization model explained in Sec .II.A.4, mesoscopic elastic coefficients by the combination of mesoscopic porosity (Sec. III.A.4) and bone matrix elastic coefficients (Sec. III.A.3) were analyzed along the femur long axis positions and anatomical quadrants. The spatially averaged values of mesoscopic elastic coefficients and technical constants from the entire human femur are listed in Table III.6.

Table III.6 *Mean and standard deviation of all mesoscopic elastic coefficients and technical constants.*

Average elastic coefficients		Average technical constants	
c_{33}	29.5 ± 4.1 GPa	E_3	23.8 ± 3.4 GPa
c_{11}	18.0 ± 2.5 GPa	G_{13}	5.5 ± 1.1 GPa
c_{12}	8.0 ± 1.0 GPa	γ_{12}	0.357 ± 0.021
c_{13}	8.6 ± 1.1 GPa	γ_{13}	0.189 ± 0.011
c_{44}	5.5 ± 1.1 GPa	γ_{31}	0.332 ± 0.012

Three-way ANOVA showed that all directional positions contribute significantly to the variations of all mesoscopic elastic coefficients (Table III.7). The second order interaction terms between the long axis position and the circumferential position suggest that all mesoscopic elastic coefficients along the anatomical positions are also dependent upon the femoral long axis position.

Table III.7 *Three-way ANOVA for mesoscopic elastic coefficients (F – statistic). Categorical factors are: Long axis position (Long – Proximal to Distal), Circumferential position (Circ – posterior, medial, anterior and lateral) and Radial position (Radi – endosteal to periosteal).*

	c_{33}	c_{11}	c_{12}	c_{13}	c_{44}
Long	9.42 *	8.95 *	9.82 *	9.88 *	8.08 *
Circ	27.05 *	8.21 *	23.79 *	27.13 *	13.08 *
Radi	4.44 *	2.01 *	2.45 *	2.02 *	1.84
Long x Circ	15.10 *	8.40 *	10.36 *	10.78 *	9.66 *
Long x Radi	0.68	1.66	1.34	1.28	0.66
Circ x Radi	0.13	0.41	0.17	0.18	0.54

*represents the significant difference at the level 0.05

III.1.5.1 Mesoscopic elastic properties along the longitudinal direction

The mean mesoscopic elastic coefficients variations along the femur long axis positions were shown in Fig. III.14. All the coefficients showed significant change along the longitudinal direction. The strongest linear dependence on the axial position was found for mesoscopic c_{33} (R^2 = 0.56). The other mesoscopic elastic coefficients, c_{12} and c_{13} and c_{44} showed weak correlation with long axis positions (R^2 = 0.29 - 34). There were no changes of the homogenized elastic coefficients c_{11} from proximal to 45% and then increased linearly to section close to distal.

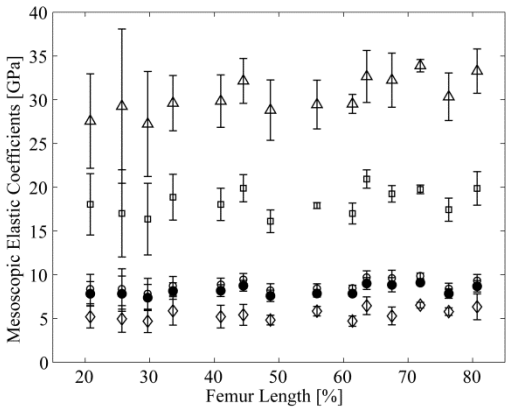

Figure III.14 *Mesoscopic elastic coefficients c_{33}(Δ), c_{11}(□), c_{12}(•), c_{13}(o) and c_{44}(◊) along the femur longitudinal direction.*

The variations of all homogenized elastic coefficients for the four anatomical quadrants along the femur long axis are shown in Fig. III.15. In the posterior quadrant, all the homogenized elastic coefficients increased linearly along the long axis from proximal to distal. There were no significant changes found in the anterior quadrant. In the medial, the mesoscopic elastic coefficients c_{33}, c_{12} and c_{13} showed significant differences and an increase along femur long axis. All coefficients reached a maximum value at 65% of femur length in these quadrants. In the lateral quadrant, the homogenized elastic coefficients c_{11} moderately decreased along the femur long axis. c_{11} has higher values below the mid shaft region than the above sections. The sections from the mid shaft to the distal region (55–80%) had similar mesoscopic c_{33}, c_{11}, c_{12} *and* c_{13} values in all anatomical quadrants. The ranges of all homogenized elastic coefficients for the four anatomical quadrants along the femur long axis are listed in Table III.8.

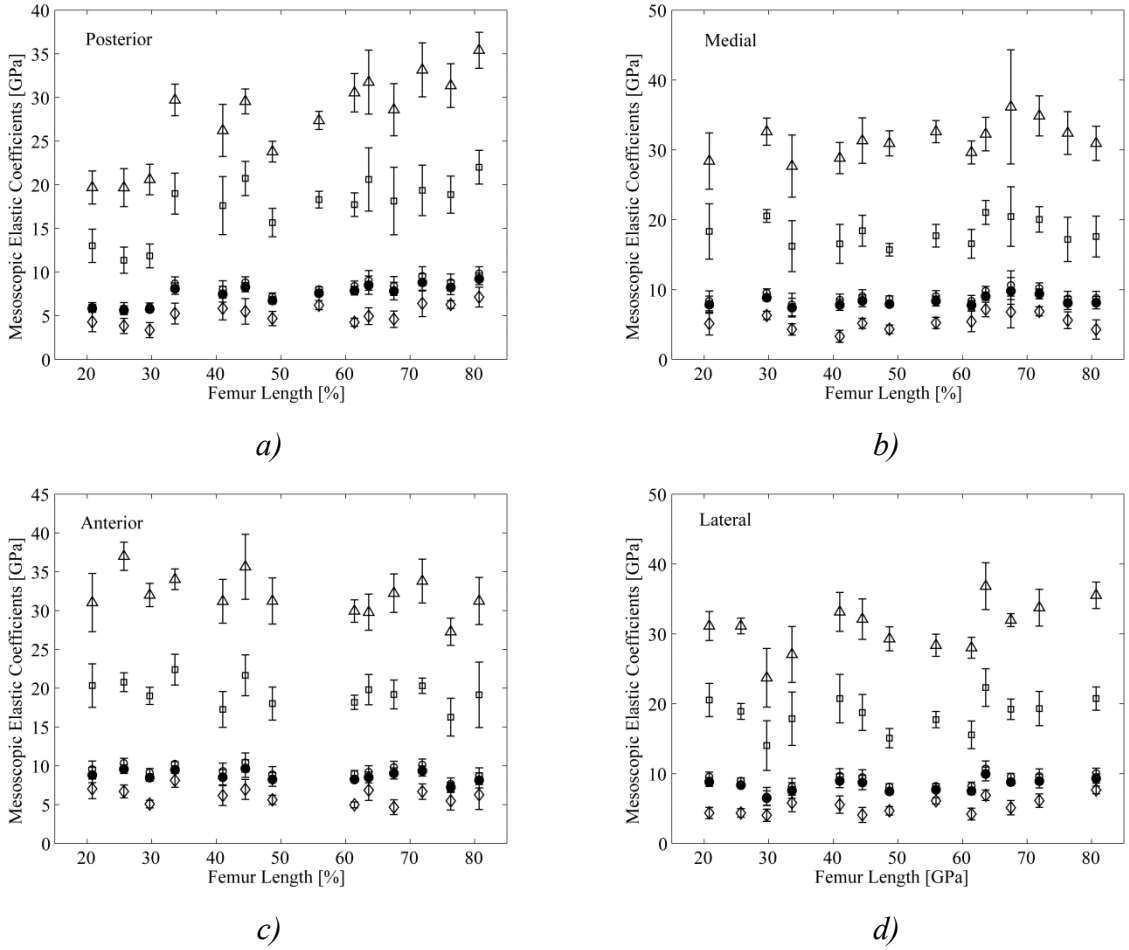

Figure III.15 *Mesoscopic elastic coefficients c_{33}(Δ), c_{11}(□), c_{12}(•), c_{13}(o) and c_{44}(◊) for four quadrants: a) posterior, b)medial, c) anterior and d)lateral along femur longitudinal direction.*

Table III.8 *The range of mesoscopic elastic coefficients in anatomical positions along the long axis of the femur.*

Anatomical position	c_{33} (GPa)	c_{11} (GPa)	c_{12} (GPa)	c_{13} (GPa)	c_{44} (GPa)
Posterior	19.67 – 35.40	11.37 – 22.00	5.62 – 9.22	5.84 – 9.84	3.36 – 7.13
Medial	27.67 – 36.15	15.07 – 21.04	7.41 – 9.81	7.85 – 10.63	3.30 – 7.15
Anterior	27.27 – 36.99	16.27 – 22.39	7.23 – 9.65	7.65 – 10.42	4.67 – 8.13
Lateral	23.71– 36.82	14.01– 22.31	6.49 – 9.95	6.71 – 10.73	4.03 – 7.65

III.1.5.2 Mesoscopic elastic properties along circumferential direction

Fig. III.16 shows the graphical representation of variation in mesoscopic elastic coefficients within the anatomical quadrants. Tukey's multiple comparison test at the 0.05 significant level shows that posterior has a lower value of mesoscopic elastic coefficients c_{33}, c_{12} and c_{13} than other quadrants. The elastic coefficients c_{11} and c_{44} were higher in the anterior than in the posterior and medial. The lateral has higher mesoscopic c_{11} value than the posterior quadrant.

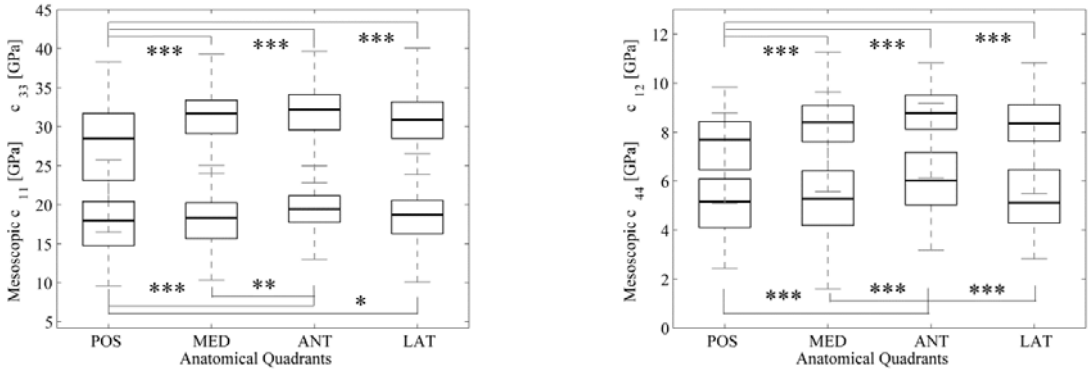

a) *b)*

Figure III.16 *Graphical representations of mean mesoscopic elastic coefficients along circumferential direction (* p<0.05, ** p<0.001 and *** p<0.0001).*

III.1.5.3 Mesoscopic elastic properties along the radial direction

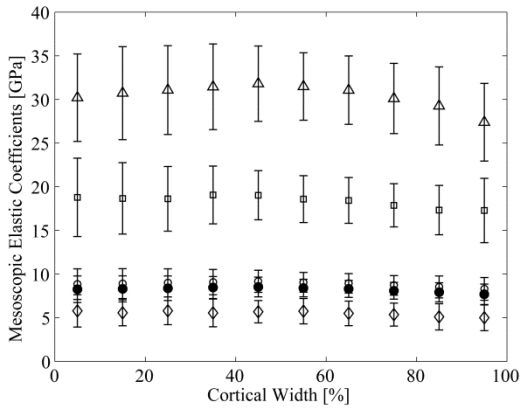

Figure III.17 *Mean and standard deviation of mesoscopic elastic coefficients c_{33} (Δ), c_{11}(□), c_{12}(●), c_{13}(○) and c_{44}(◊) along the radial direction (5% and 95% correspond to the sections adjacent to the endosteum and periosteum respectively).*

The variations of mesoscopic elastic coefficients along the radial position are given in Fig. III.17. Here, 10% corresponds to the section close to endosteum and 100% section close to periosteal. None of the mesoscopic elastic coefficients showed any significant changes along radial direction. Only the last section, close to the periosteal had lower values of c_{33}, c_{12} and c_{13} compared to central region (40 – 50%) of cortex.

III.1.5.4 Mesoscopic anisotropy ratio

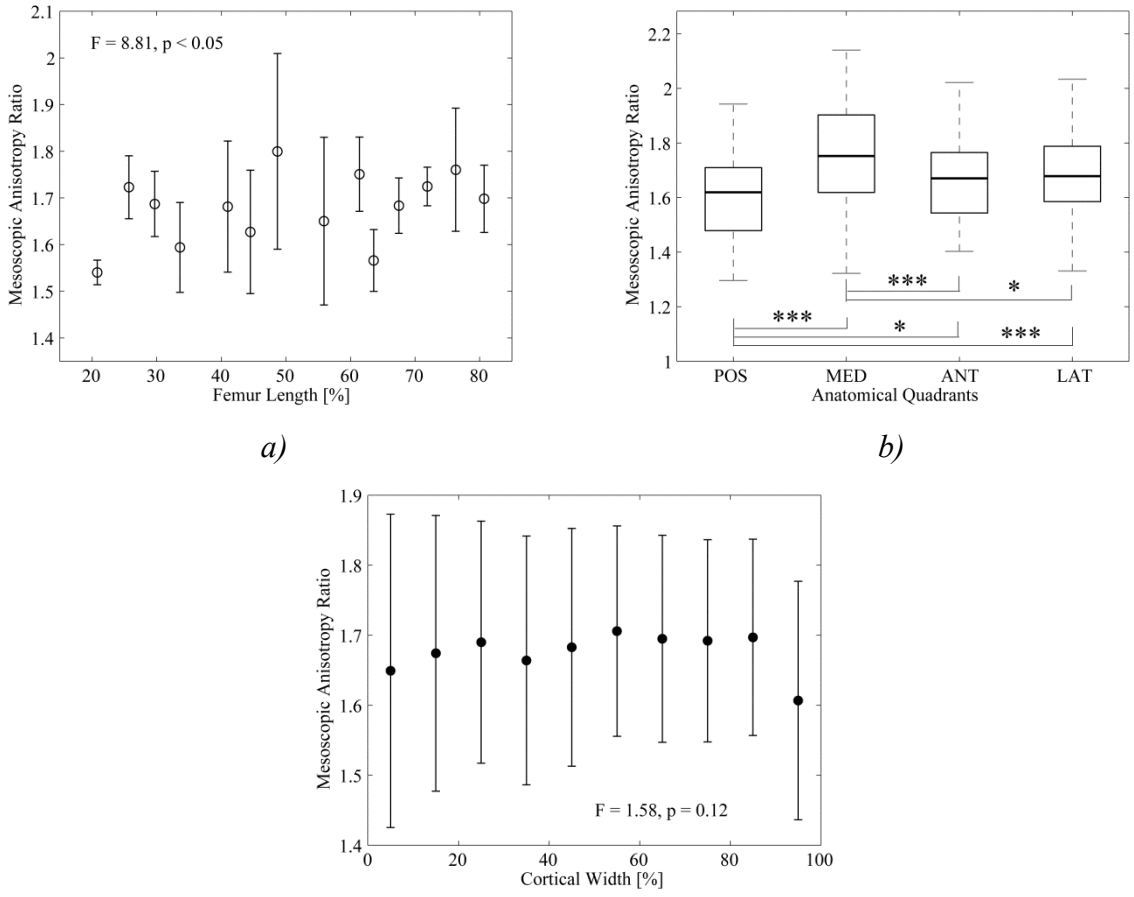

Figure III.18 *Variation of mesoscopic anisotropy ratio along a) longitudinal, b) circumferential and c) radial directions (* p<0.05, ** p<0.001 and *** p<0.0001).*

The mesoscopic anisotropy ratio varied with respect to the long axis and anatomical positions (Fig. III.18). The mean and range of the mesoscopic anisotropy ratio are 1.67 ± 0.17 and 1.54 – 1.79. For all anatomical quadrants, no significant changes in mesoscopic anisotropy ratio were found in sections close to proximal and distal along the femur long axis.

There were only changes in the middle region from 40 to 60 % of femur length. The medial and lateral had higher anisotropy ratios than the posterior in this region. Along the circumferential direction, the posterior has a lower anisotropy ratio than the other quadrants. The medial has a higher value than the anterior and lateral (Fig. III.18b). The mean mesoscopic AR for anatomical quadrants; posterior, medial, anterior and lateral are 1.61 ± 0.09, 1.75 ± 0.13, 1.66 ± 0.09 and 1.69 ± 0.11. There were no significant changes of mesoscopic anisotropy ratio along the radial direction (Fig. III.18c).

III.1.6 Spatial distribution of degree of mineralization

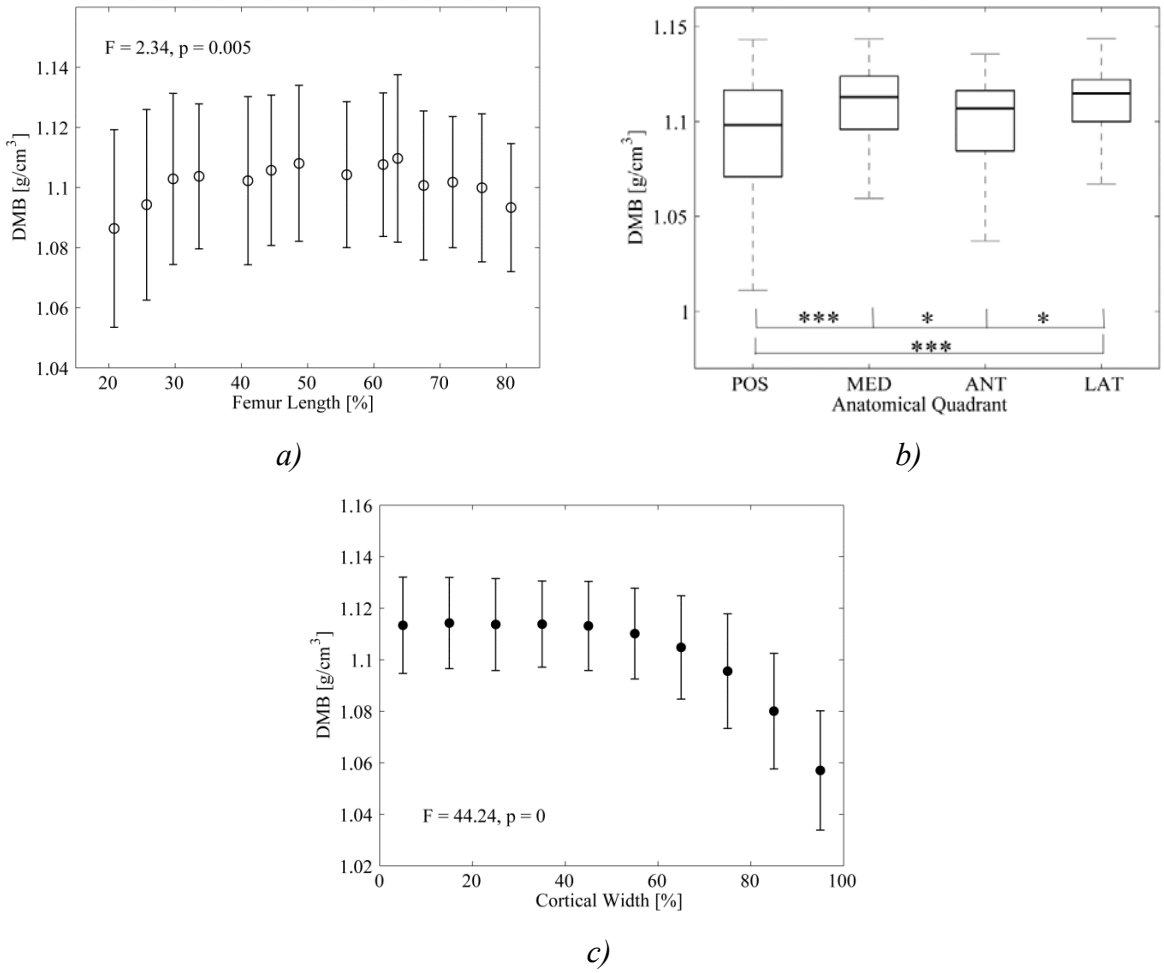

Figure III.19 *Variation of DMB of human femur along a) longitudinal, b) circumferential and c) radial directions* (* $p<0.05$ and *** $p<0.0001$).

The variations in degree of mineralization along three directions are shown in Fig. III.19. The DMB values did not show a significant variation along the long axis. Only the most proximal position at 20.8% had significantly smaller values compared to the central

regions (around 34% to 74% of the femur length). The mean and the range of DMB along the long axis are 1.102 ± 0.006 and 1.086 – 1.110 g/cm^3. Along the anatomical direction, DMB has significantly lower values in the posterior and anterior quadrants than in the medial and lateral quadrants. The mean DMB values for anatomical quadrants; posterior, medial, anterior and lateral are 1.091 ± 0.022, 1.108 ± 0.013, 1.099 ± 0.016 and 1.109 ± 0.010 g/cm^3. Along the radial direction there was not significant difference from the endosteum upto 65% of cortical width, and they decreased up to the periosteal. The mean and range of DMB along the radial direction are 1.102 ± 0.019 and 1.057 – 1.114 g/cm^3.

III.1.7 Correlation of elastic parameters with structural properties and DMB

Table III.9 *Correction coefficients between the structural parameters and microscopic elastic coefficients of human cortical bone.*

r	Cortical Width	Porosity	Canal Diameter	Canal Density	DMB
			Microscopic elastic coefficients		
c_{33}	-0.32*	-0.21	0.13	0.26	0.54*
c_{11}	-0.22	0.09	0.05	0.10	0.29*
c_{12}	-0.32*	-0.21	0.13	0.26	0.53*
c_{13}	-0.32*	-0.21	0.13	0.26	0.53*
c_{44}	-0.33*	0.23	-0.02	0.06	0.10
c_{33}/c_{11}	-0.15	-0.30*	0.11	0.20	0.32*
			Mesoscopic elastic coefficients		
c_{33}	-0.27*	-0.62*	-0.09	0.19	0.44*
c_{11}	-0.15	-0.72*	-0.22	0.16	0.22
c_{12}	-0.20	-0.82*	-0.21	0.19	0.40*
c_{13}	-0.19	-0.85*	-0.21	0.19	0.42*
c_{44}	-0.34*	-0.19	-0.14	0.13	0.03
c_{33}/c_{11}	-0.14	0.11	0.19	0.04	0.32*

* represents the significant correlation at the 0.05 level

The influence of structural properties and DMB on microscopic and homogenized elastic coefficients, estimated from four anatomical quadrants for all cross sections, was

analyzed using linear regression and is shown in Table III.9. Some of the microscopic and homogenized elastic coefficients were partially correlated with cortical thickness and decreased with respect to thickness. None of the other structural parameters showed any dependency on bone matrix elastic coefficients. All homogenized elastic coefficients except c_{44} have strong correlations and decreased with respect to mesoscopic porosity.

The elastic coefficients c_{33}, c_{12} and c_{13} have a moderate correlation and increased with the degree of mineralization in both bone matrix and homogenized cases. The highest correlation between tissue level axial elastic coefficient and degree of mineralization is shown in Fig. III.20.

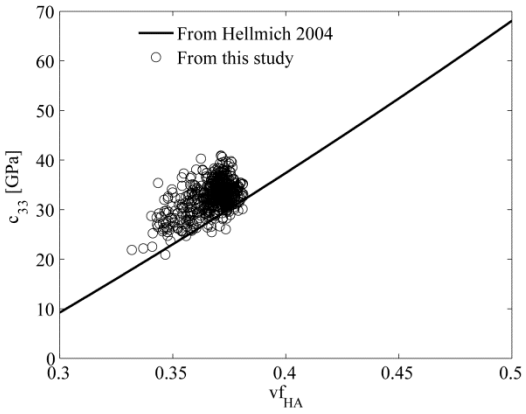

Figure III.20 *Relation between bone tissue axial elastic coefficient, c_{33} and volume fraction of hydroxyapatite, vf_{HA} from Hellmich et al. [21] and this study.*

The bone tissue elastic coefficient and volume of fraction of hydroxyapatite relation was not exactly similar to how it is shown in Hellmich et all [21]. This could be due to different fibril orientations, embedding, or other differences in the collagenous organic matrix.

III.2 Skeletal muscle

III.2.1 Chemical and structural parameters of muscle

The mean and range of the structural and chemical parameters of *longissimus* muscle are given in Table II.10.

Table III.10 *Mean, coefficient of variance and range of chemical parameters and structural parameters of M. longissimus are listed.*

	Mean ± STD	CV [%]	Minimum	Maximum
Chemical Parameters				
Intramuscular fat [%]	1.3 ± 0.6	45.7	0.63	3.16
pH 45	6.4 ± 0.2	2.8	6.08	6.74
EZ drip loss [%]	5.7 ± 2.9	51.9	1.29	13.36
Protein [%]	24.0 ± 0.8	3.5	21.82	25.42
Dry matter [%]	25.5 ± 0.7	2.7	24.36	27.00
Structural Parameters				
Bundle Ø [µm]	806 ± 115	14.3	532.48	1103.29
Fiber Ø [µm]	81 ± 7	9.7	68.30	94.90
FTG Ø [µm]	85 ± 8	9.9	68.49	102.49
FTO Ø [µm]	65 ± 10	14.6	45.34	95.61
STO Ø [µm]	70 ± 7	10.3	54.78	81.37
FTG [%]	78 ± 4	4.9	70.82	84.21
FTO [%]	12 ± 3	28.8	6.46	19.28
STO [%]	10 ± 3	29.2	5.88	17.93

FTG – fast twitch glykolytic; FTO – fast twitch oxidative; STO – slow twitch oxidative

The highest coefficients of variation were reached for IMF and the amount of drip loss. The CV of the other compositional parameters was rather low, ranging between 2.5 and 4%. Histological parameters showed mediocre standard deviations with a CV between 5 and 14%.

III.2.2 Acoustic parameters of muscle at fiber level

The acoustic parameters estimated at fiber level using 100 MHz scanning acoustic microscope (Sec. II.B.3) are discussed in this section.

III.2.2.1 Anisotropy of muscle acoustic parameters at fiber level

The maps acoustic propagation parameters (e.g., attenuation and speed of sound) and the material parameters (e.g., impedance and density), estimated from one of the fiber parallel muscle samples are shown in Fig. II.23. The figure contains the parameters only from the muscle fibers and all the connective tissue is excluded as mentioned in the section (Sec. II.B.3.2). The mean and range of acoustic propagation parameters (e.g., speed of sound, attenuation) and material parameters (e.g., impedance, density and elastic coefficient) for both fiber orientations of muscle samples are given in Table II.11.

Table III.11 *Mean and range of acoustic propagation parameters and material parameters along fiber parallel and perpendicular orientations are listed.*

	Parallel		Perpendicular	
	Mean ±std	Range	Mean ±std	Range
Speed of Sound v [m/s]	1599 ± 14	1573 – 1630	1573 ± 13	1552 – 1596
Attenuation α [$dB/MHz/cm$]	6.23 ± 0.69	5.08 – 7.85	1.90 ± 0.51	1.00 – 3.25
Impedance Z [$MRayl$]	1.69 ± 0.01	1.67 – 1.72	1.67 ± 0.01	1.65 – 1.68
Density ρ [g/cm^3]	1.06 ± 0.01	1.04 – 1.07	1.06 ± 0.01	1.04 – 1.09
Elastic coefficient c [GPa]	2.69 ± 0.03	2.65 – 2.77	2.62 ± 0.02	2.58 – 2.67

The attenuation coefficient and speed of sound in each muscle showed a distinct difference between measurements of parallel and perpendicular orientation (F = 644 and F = 43). For all muscle samples, those parameters were higher along the fiber direction than the perpendicular to fiber orientation. The attenuation plot $\alpha(f)$ for a single #1 sample is shown in (Fig. III.22). In all muscle samples measured, the error bars of the two orientations were well separated like this. The anisotropy ratios, i.e. the ratios of the values measured in the parallel direction to the values measured in the perpendicular direction, for the attenuation coefficients and speed of sound for porcine *longissimus* were 3.47 ± 0.86 and 1.02 ± 0.01 respectively. The higher anisotropic index for attenuation indicates its higher direction dependency compared to speed of sound.

The elastic coefficients c_{33} and c_{11} estimated from acoustic impedance and density for the parallel and perpendicular directions are 2.69 ± 0.03 and 2.62 ± 0.02 GPa respectively. The mechanical parameters (impedance and elastic coefficients) are significantly higher in the parallel direction compared to the perpendicular direction, as in ultrasonic propagation parameters (F = 60 and F = 92 respectively). The significant differences in elastic coefficients between both sections are shown in Fig. III.21a. The anisotropy ratios for impedance and elastic coefficient were 1.01 ± 0.01 and 1.03 ± 0.01 respectively. As expected, the mass density was not affected by the direction of measurement.

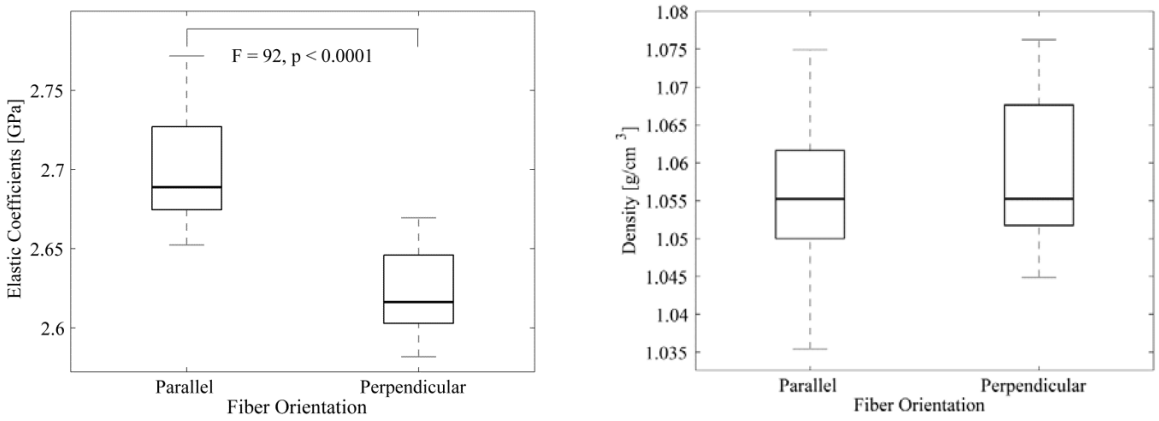

Figure III.21 *Variation of elastic coefficients and density with respect to muscle fiber orientation.*

III.2.2.2 Acoustic parameters for different fiber types

As mentioned in the Sec. II.B.3.3 in this study muscle fibers are differentiated into two types as STO and FTO+FTG, and their acoustic parameters are compared. The mean values of acoustic parameters of fiber types STO and FTG+FTO along the fiber direction were ν = 1581 ms^{-1}; Z = 1.66 Mrayl; α = 5.59 dB cm^{-1} MHz^{-1} and ν = 1589 ms^{-1}; Z = 1.68 Mrayl; α = 6.19 dB cm^{-1} MHz^{-1} respectively. No significant differences in speed of sound and attenuation within the fiber types could be stated. However, the acoustic impedance values in STO fibers were slightly lower than in FTO+FTG fibers ($F = 4.99$, $p = 0.04$).

III.2.2.3 Correlation of microscopic muscle acoustic parameters with compositions

The linear correlation coefficients of acoustic parameters along the fiber parallel and perpendicular orientations and their corresponding anisotropic ratio with muscle composition and structural properties are given in Table III.12.

The IMF content was not correlated with any of the acoustic properties. Sound velocity and attenuation coefficient values increased significantly with increasing drip loss, while inverse relations were found with dry matter. Attenuation of porcine muscle behaves similarly in both fiber orientation cases, while the anisotropy of attenuation increased with respect to dry matter. The protein content showed a slight positive relationship with the attenuation coefficient and impedance values. However, none of them were significant. No significant correlation could be found comparing structural parameters from histology (e.g., fiber type distribution or diameter) with any of the acoustic parameters (data not shown).

Table III.12 *Linear correlation coefficient (r) of acoustic parameters of fiber orientation parallel and perpendicular to sound propagation with tissue compositions and structural parameters.*

r		IMF	Drip loss	Protein %	Dry matter	Glykolytic fibers [%]
Parallel	ν	-0.20	0.35	-0.14	-0.26	0.22
	α	-0.34	0.29	0.27	-0.08	-0.03
	Z	-0.15	0.00	0.16	-0.06	-0.14
	ρ	0.09	-0.33	0.23	0.21	-0.29
Perpendicular	ν	0.08	0.11	0.12	0.14	-0.05
	α	-0.25	0.25	-0.09	-0.42*	0.21
	Z	-0.30	0.37	0.30	-0.11	0.20
	ρ	-0.20	0.10	0.05	-0.16	0.14
Anisotropy index	ν	-0.20	0.18	-0.19	-0.29	0.21
	α	0.13	-0.07	0.15	0.44*	-0.12
	Z	0.13	-0.34	-0.11	0.04	-0.32

*represents significant correlation at the 0.05 level

III.2.3 Macroscopic acoustic reference data of porcine muscle and back fat compound

For intermediate medium attenuation and refraction correction for backscatter data acquisition, anticipated to improve non-invasive ultrasound based muscle characteristic estimation, reference acoustic parameters from muscle and back fat compound were determined using 10 MHz scanning acoustic microscope (Sec. II.B.4). Those results are discussed in this section.

III.2.3.1 Acoustic properties of back fat compound

The mean and rang of individual fat layers acoustic parameters (sound speed, attenuation and thickness) are given in Table III.13. The skin and complete back fat compound (skin + all fatlayers) were also estimated. The mean attenuation and sound speed of skin were 2.6 ± 1.1 dB/MHz/cm and 1682 ± 23 m/s respectively. Thickness of skin remained more or less constant for all samples, 2.7 ± 0.4 mm. And, the mean attenuation and sound speed of back fat compound were 2.5 ± 0.6 dB/MHz/cm and 1502 ± 20 m/s respectively.

Table III.13 *Mean and range of acoustic parameters of individual fat layers: subcutaneous fat layer (n =20), intermediate fat layer (n = 17) and inner fat layer (n = 14).*

	Subcutaneous fat layer		Intermediate fat layer		Inner fat layer	
	Mean	Range	Mean	Range	Mean	Range
Thickness [mm]	4.7 ± 1.5	2.7 – 7.5	4.8 ± 2.0	2.0 – 8.9	3.8 ± 1.0	2.1 – 5.3
Sound speed [m/s]	1435 ± 9	1425 – 1476	1450 ± 22	1426 – 1519	1469 ± 37	1441 – 1562
Attenuation [dB/MHz/cm]	1.6 ± 0.7	0.8 – 3.4	1.6 ± 0.7	0.6 – 4.0	2.7 ± 1.5	1.2 – 6.8

Skin and fat have a significant difference in thickness ($F = 28.9$, $p = 0$), sound speed ($F = 12.74$, $p < 0.001$) and attenuation ($F = 4.92$, $p < 0.05$). Within the fat layers, attenuation has significantly different values and no difference in thickness and sound speed. The inner fat layer has a higher attenuation than subcutaneous and intermediate fat layers and there is no difference between attenuation in the subcutaneous and inner fat layers. But, the data shown in Table III.13 represents that the subcutaneous fat layer has the lower sound speed and increases to inner fat layer. But the thickness is decreasing from the subcutaneous to the inner fat layer.

A strong correlation was found between the back fat compound's speed of sound and thickness ($R^2 = 0.73$, $p = 0$). The back fat compound's speed of sound decreased with increasing thickness (Fig. III.22). To a lesser extent, sound velocity also decreased with increasing thickness of the individual fat layers. However, attenuation was less affected by

total back fat thickness and thickness of the individual layers respectively, except for the intermediate fat layer.

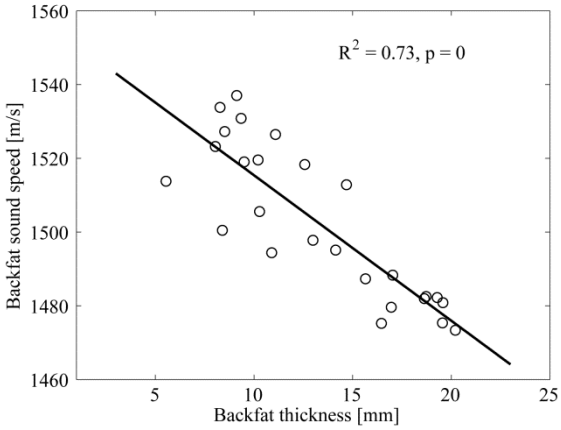

Figure III.22 *Linear regression analysis of back fat compound (skin + three fat layers) sound speed versus thickness.*

III.2.3.2 Macroscopic acoustic properties of muscle

The acoustic parameters were measured with the same fiber orientation as for the intact carcass, i.e. the muscle fiber orientation was 30° to 45° relative to the sound propagation direction. The mean sound speed was 1620 ± 4 m/s and varied from 1610 to 1628 m/s. The mean attenuation was 1.02 ± 0.26 dB/MHz/cm and varied from 0.54 to 1.55 dB/MHz/cm.

The Pearson correlation coefficients of associations between macroscopic acoustic parameters and compositions are summarized in Table III.14.. The acoustic parameters, speed of sound and attenuation showed inverse relations with all muscle compositions. The meat quality parameter IMF was moderately correlated with acoustic properties. Relations between the attenuation and histological traits (data not shown) have been found for the amount of FTG (r = -0.31) and STO fibers (r = 0.29). Speed of sound significantly decreased with IMF, while an inverse relation was found with protein %.

Table III.14 *Linear correlation coefficient (r) of macroscopic acoustic parameters with tissue compositions.*

Acoustic parameters	IMF	pH	Drip loss	Protein	Dry matter
Sound speed	–0.50 *	–0.04	0.17	0.41 *	–0.06
Attenution	0.66 *	0.33	–0.43 *	–0.15	0.35

*represents significant correlation at the 0.05 level

III.2.4 Non-destructive muscle characteristics investigation

The abbreviations and a short description of acoustic parameters calculated from the muscle region of interest using quantitative ultrasonic device RF data (Sec. II.B.5) are given in Table III.15.

III.2.4.1 Estimated parameters from the muscle region of interest

Table III.15 *The acoustic spectral and cepstral parameters extracted from the quantitative ultrasonic device RF data are listed.*

Parameters	Units	Description
TOF_{BF}	µs	Back fat compound time of flight
d_{BF}	mm	Back fat compound thickness
SOS_{BF}	m/s	Back fat compound speed of sound
α_{muscle}	dB/MHz/cm	Muscle attenuation coefficient
AIB	dB	Mean of apparent integrated backscatter amplitude
M	dB	Midbandfit
m	dB/MHz	Backscatter power spectral slope
RF_{excl}	%	Percent of rf signals correspond to spectral intensity below -40 dB excluded
IC		Integrated cepstrum
$C_{fp}(\tau_{fp})$		Cepstrum first peak amplitude
τ_{fp}	µs	Cepstrum first peak amplitude position

Prior to statistical analysis all ultrasound measurements were checked for reliability. Out of 218 performed measurement (54 x 3 and 28 x 2), 83 measurements (38%) had to be excluded. The reason for excluding the data were focus area and corresponding ROI at the muscle/rib interface, very weak scattering amplitudes resulting in an insufficient SNR, multiple reflections of the back fat interfaces in the muscle ROI due to bad coupling and spectrum amplitude > 20 dB higher than the remaining distribution. For 20 out of 82 carcasses all three ultrasound measurements had to be excluded. To investigate the relation between the acoustic parameters and muscle compositions and structural properties, acoustic parameters of three replicate measurements per animal from the remaining carcasses were averaged. The mean and range of all extracted parameters from US data are summarized in Table III.16.

Table III.16 *Mean, standard deviation, coefficients of variance (CV), minimum and maximum of extracted acoustic parameters are listed.*

Parameters	Mean ± STD	CV [%]	Minimum	Maximum
TOF_{BF} [µs]	20.1 ± 4.5	22.2	11.9	30.4
d_{BF} [mm]	15.0 ± 3.1	20.5	8.8	20.7
SOS_{BF} [µs]	1491 ± 14	0.95	1467	1520
α_{muscle} [dB $MHz^{-1}cm^{-1}$]	0.77 ± 0.15	19.3	0.54	1.17
AIB [dB]	-34.1 ± 4.6	13.5	-42.7	-22.3
M [dB]	-34.0 ± 4.4	13.0	-42.1	-22.8
m [dB MHz^{-1}]	4.07 ± 1.17	28.77	1.25	6.33
Excluded RF-signals [%]	24.5 ± 14.6	59.6	1.4	61.1
IC [dB]	2.01 ± 0.10	5.02	1.78	2.23
$C_{fp}(\tau_{fp})$ [dB]	2.33 ± 0.14	5.81	2.07	2.64
τ_{fp} [µs]	1.02 ± 0.01	1.33	0.99	1.05

No significant difference could be stated between back fat SOS (paired *t*-test, p = 0.22) and thickness (paired *t*-test, p = 0.15) measured from UF300 back fat TOF and SAM data with 10 MHz (Sec. III.B.3.1) [168]. Results of linear regressions analysis of acoustic parameters with muscle composition and structural parameters are given in Table III.17.

Table III.17 *Linear correlation coefficient (r) of frequency dependent acoustic parameters with tissue compositions and structural parameters.*

	Chemical Parameters				Structural Parameters	
Acoustic Parameters	IMF	Drip loss	Protein %	Dry matter	Fiber ∅	Bundle ∅
TOF_{BF}	**0.27 ***	-0.13	0.04	**0.29 ***	-0.11	0.02
d_{BF}	0.25	-0.13	0.06	**0.28 ***	-0.14	0.03
$SOSd_{BF}$	-0.25	0.13	-0.06	**-0.28 ***	0.14	-0.03
α_{muscle}	**0.61 ***	**-0.28 ***	**-0.35 ***	0.23	-0.19	0.24
AIB	**0.56***	-0.23	-0.24	**0.31 ***	**-0.30 ***	0.08
M	**0.56***	-0.24	-0.24	**0.31 ***	**-0.30 ***	0.09
m	0.04	0.09	0.07	0	-0.27	0.14
RF_{excl}	-0.17	0.06	-0.18	-0.10	**0.34 ***	0.20
IC	**0.26 ***	-0.09	-0.21	0.14	**-0.36 ***	-0.07
$C_{fp}(\tau_{fp})$	**0.29***	-0.10	-0.19	0.18	**-0.41 ***	-0.11
τ_{fp}	0.10	-0.13	-0.19	0.01	-0.15	-0.13
τ_{fp} (std)	-0.21	0.01	-0.04	-0.09	0.02	-0.28

*Represents the significant correlation at the 0.05 level

III.2.4.2 Correlation of spectral parameters with tissue compositions

Among the muscle composition parameters, only intramuscular fat content and dry matter showed reasonable correlation with acoustic parameters. The spectrum amplitude (AIB, M) showed significant positive correlation with those compositions. Weak correlations were also observed between cepstral amplitudes (IC, C_{fp}) and IMF. Highest positive correlation was observed between IMF and muscle attenuation, α_{muscle}.

III.2.4.3 IMF prediction using the multivariate method

Multiple regression analysis (MLR) was performed using a variety of estimated acoustic parameters. A highly significant model (R2 = 0.76, RMSE = 0.34%) could be obtained by the combination of back fat compound time of flight TOF_{BF}, muscle attenuation α_{muscle} and spectral slope. It should be mentioned that, even if α_{muscle} was the most important variable inside the model, removal of even one of the three variables tremendously increased the prediction error.

$$IMF^{US} = -2.416\,\% + (0.108\,\mu s^{-1} TOF_{BF})\% + (4.755 dB^{-1} MHz.cm\ \alpha_{muscle})\% - (0.457\,m\,dB^{-1} MHz)\% \quad \text{(III.1)}$$

The IMF predicted from multiple stepwise regression model was compared with IMF estimated from chemical analysis using Bland – Altman plot (Fig. III.23). The IMF determined from chemical analysis and prediction model were 1.53 ± 0.68% and 1.53 ± 0.61% respectively. The relative percent difference was (17.8 ± 15.7) % (mean and standard error), but this difference was not significant (paired *t*-test, p = 0.99). Furthermore, about half of the samples could be predicted with a RMSE of 0.2% IMF or less.

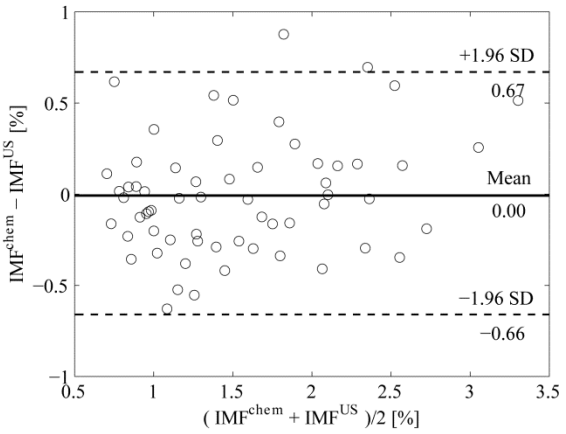

Figure III.23 *Bland-Altman plot shows the comparison of IMF predicted from chemical analysis and ultrasound.*

The results of the classification of the obtained IMF^{US} values into the for meat quality important threshold levels of < 1 % (LOW), 1-2 % (MID) and > 2 % IMF (HIGH) and the comparison with the IMF^{chem} values can be seen in Table III.17. Overall, about 73% of all samples were assigned to the correct IMF class. Furthermore, it should be mentioned that only 1 sample was falsely classified into the HIGH class. However, this sample had an IMF^{chem} value of 1.9% proving the practicability of ultrasound spectral analysis to classify HIGH IMF meat correctly.

Table III.18 *Grouping of IMF values into important meat quality threshold levels (LOW: <1 %, MID: 1 – 2 %, HIGH: > 2 %) using multiple linear regression analysis versus chemically determined IMF value (n=62).*

	Chem. LOW	Chem. MID	Chem. HIGH
US LOW	**10 (50 %)**	2 (8 %)	
US MID	10 (50 %)	**22 (88 %)**	4 (24 %)
US HIGH		1 (4 %)	**13 (76 %)**

III.2.4.4 Correlation of spectral parameters with structural properties

From structural parameters estimated from histology, fiber diameter showed the moderate correlations (up to r = -0.3) with spectral parameters (AIB and M). All those parameters decreased with increasing fiber diameter. In contrast to fiber diameter, no significant correlation could be found between the bundle diameter and any of the acoustic parameters. It has weak correlation with cepstrum parameter, τ_{fp}, but not significant. Generally, cepstral parameter τ_{fp} represents the scatter size and distances depending on the ultrasonic system axial resolution and frequency. The range of τ_{fp} = 0.99 – 1.05 µs corresponds to spatial distance range between 800 and 850 µm, which is in the order of the primary bundle diameter. But the average bundle diameter determined from histology is 689 ± 75 µm. In this quantitative ultrasonic measurement, bundles were oriented 30° - 45° to skin surface. In the histology for fiber and bundle diameter estimation, thin slices of muscle samples were prepared by cut perpendicular to fiber orientation. That difference in fiber orientation angle has to be correlated for comparison of histology and cepstrum. The averaged bundle diameter estimated from τ_{fp} after orientation angle correction (~ 30°) is 712 ± 10 µm. The average relative difference between the bundle diameter estimated from τ_{fp} and histology was (8.1 ± 7.2) % (mean and standard error). The histogram of bundle diameter estimated from τ_{fp} within the evaluated ROI is shown in Fig. III.24.

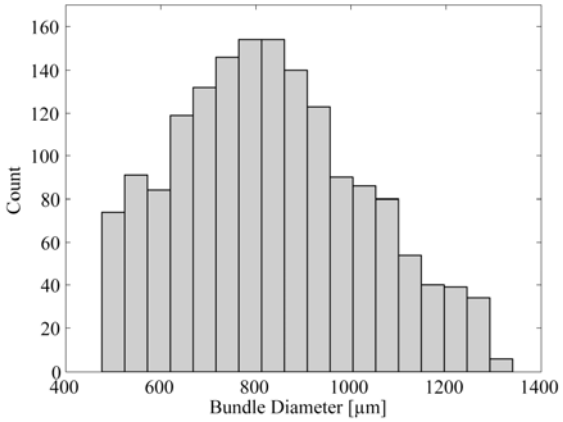

Figure III.24 *Muscle bundle diameter histogram distribution estimated from* τ_{fp} *within the evaluated muscle ROI.*

IV Discussion

IV.1 Cortical bone

Elastic constants of cortical bone are widely used nowadays in conjunction with numerical simulations, e.g., deformation or fracture analysis, fracture, or ultrasound wave propagation. For these models, accurate knowledge of elastic constants of compact bone especially femur which is common skeletal site of fracture in human is necessary. In previous studies, the elastic properties of the human femoral cortical bone was analyzed with limited number of specimens and bone range covered was between 40% and 70% of the femur length [48;49;178-180]. In those studies, samples were prepared by cutting bone sections in different directions relative to a principle axis of symmetry. This causes a high preparation and measurement effort. Even, those studies have been done with a frequency range of 2 – 5 MHz which determines the elastic properties by both bone matrix and porous structure. For a better understanding of the tissue alteration due to pathological conditions, tissue level elastic cortical bone is necessary.

IV.1.1 Estimation of elastic coefficients of cortical bone

In this study, a new procedure has been developed to assess the anisotropic elastic coefficients of cortical bone at tissue level. Previous studies have shown that a highly focused 50-MHz transducer has sufficient lateral resolution for a reliable segmentation of Haversian canals from the bone tissue and that the acoustic impedance derived from two-dimensional maps of the confocal reflection amplitude is sensitive to elastic tissue anisotropy [27;36;37]. In this study the anisotropy estimation was considerably improved by using cylindrically shaped samples as opposed to flat sections cut at different angles relative to the femoral long axis. This allowed us to assess a continuous angular spectrum of the acoustic impedance from a small sample volume with a single measurement, while for each probing angle a sufficient number of measurements were maintained. Therefore precise fits ($R^2 \geq 0.97$) to a transverse isotropic elastic model were obtained. The strong relation between elastic coefficient and acoustic impedance was also found ($R^2 = 0.99$) by site-matched analysis of acoustic impedance and tissue degree of mineralization maps as shown in previous studies [151]. This relation, determined from human femur was used to convert acoustic impedance values into stiffness coefficients. The inspected tissue volume of the cylinders contained a representative

ensemble of structural units (osteons and interstitial tissue). However, the volume was small enough to minimize influences due to anatomical variations of elastic tissue properties. The axial (c_{33}) and radial (c_{11}) elastic coefficients were accessed directly from the experimental data. The remaining elastic coefficients were predicted by the incorporation of composite and continuum mechanical model constraints of all elastic coefficients of the transverse isotropic tissue matrix. The microscopic level mechanical properties of bone depend on the properties of the collagen fibrils constituents, their microstructure, and orientation distribution, also mineral content and the shape of the mineral particles [100].

The diagonal components of the stiffness matrix predicted from the open-foam model are sometimes considerably larger compared to the values determined from the fit of $c(\theta)$ to the transverse isotropic model. This confirms the finding of Hellmich *et al.* [21] that only the off-diagonal components of the stiffness matrix predicted by this model agree well with experimentally derived values. The main drawbacks of this continuum micromechanical model were that the mineralized collagen fibril orientation did not included and also a less realistic spherical shape assumption for HA minerals was used. Several studies are going on to improve hierarchical modeling of the elastic properties of cortical bone at micron and submicron level as shown in the section [94;100;105]. But until now, there is no efficient model available to predict the ultrastructural elastic properties of bone accurately including collagen fibril orientation.

For the estimation of homogenized mesoscopic elastic coefficients of cortical bone, the asymptotic homogenization method was used by modeling the low-frequency elastic waves propagation through an idealized material that models the local mesostructure [115]. In this method, the bone tissue matrix is represented by hexagonal [157] and the pore is modeled as a cylinder of infinite extent in the long axis direction filled with water.

IV.1.2 Microscopic and mesoscopic elastic coefficients of human femur

The entire cross sectional measurements showed the Haversian tissue structure for a female femur aged 72 year. This study was the first to report explicitly anatomic variation in the elastic properties of human femoral cortical bone tissue, though the necessary data may have been available in the previous studies. Cortical thickness is typically higher in the mid-femur and proximal mid-diaphysis, making this region most convenient and practical for preparing specimens.

Table IV.1 *Comparison of stiffness coefficients of human cortical femur from this study and from selected references from the literature.*

Elastic Coefficients [GPa]	This study Microscopic	This study Mesoscopic	Ashman et al. [48]	Yoon and Katz [181]	Espinoza et al. [181]
c_{33}	34.6 ± 3.6	29.5 ± 4.1	27.6 ± 1.7	32.5 ± 0.4	27.3 ± 1.6
c_{11}	24.1 ± 2.0	18.0 ± 2.5	20.2 ± 1.8	23.4 ± 0.3	19.7 ± 2.1
c_{12}	10.2 ± 0.8	8.0 ± 1.0	10.0 ± 1.3	9.1 ± 0.4	10.7 ± 0.7
c_{13}	11.1 ± 0.8	8.6 ± 1.1	10.1 ± 1.7	9.1 ± 0.6	---
c_{44}	7.0 ± 1.2	5.5 ± 1.1	6.2 ± 0.7	8.7 ± 0.1	6.2 ± 0.5
Source	Dry Femur *(Age 72)*	Dry Femur *(Age 72)*	Wet Femur *(Age ---)*	Dry Femur *(Age 57)*	Wet Femur *(Age 78)*
Ultrasonic method	Pulse echo technique (50 MHz)	Pulse echo technique (50 MHz)	Continuous technique (2.25 MHz)	Transmission method (5 MHz)	Transmission method (2.25 MHz)

The comparison of elastic coefficients measured with this new procedure and previous macroscopic techniques is shown in Table IV.1. Note that, in those studies, samples were prepared from the mid diaphysis and the number of specimens was smaller. The mesoscopic elastic coefficients determined in this study are within the range of values shown in previous works. By comparing mesoscopic elastic coefficient with previous studies using the same

femur age range, the axial elastic coefficient was a bit higher in this study. Several investigations reported increased microhardness of the dry bone compared to fresh bone. They concluded the decreased water content in bone through the embedding procedure affects the elasticity and microhardness of bone sample substantially. Zimmerman [182] found a significant difference of about 4.2% between acoustic impedances measured from native and embedded samples. Turner et al. [24] got Young's moduli of human cortical bone measured using nanoindentation techniques 0 – 20 % higher than by Ashman. The embedding procedure and the cylindrical shaped transverse isotropic fiber of the circular cross section as pore inclusion in the homogenization procedure, affect the mesoscopic anisotropic ratio.

The variation of tissue elastic coefficients of femur diaphysis at 14 spaced locations along its length, in four anatomical positions as well as 10 sections along the radial directions was analyzed. All elastic coefficients varied significantly along all three directions. The variation of elastic properties was rather similar in both microscopic and mesoscopic levels.

Ashman et al. [48] observed that density and stiffness coefficients were greater at the 50, 60, 70 percent levels of the femur compared to the 30 and 40 percent level. Ashman et al. [48], Bensamoun et al. [30], Weiss et al. [33] and Espinosa et al. [50] also observed a statistically significant decrease in the stiffness coefficient and density of the posterior region relative to the other quadrants as shown in this study. Evans and Lebow [183] showed that the ultimate tensile strength and elastic modulus were greatest in the middle third and lowest in the proximal third of the femur shaft. Among the quadrants tested, they found the medial quadrant of the middle third have the greatest mechanical properties. In our case, the medial quadrant has a higher axial elastic coefficient and anisotropy ratio in the middle. They found the anterior quadrant of the proximal third have the lowest properties. Dissimilarities here are most likely due to the sectioning difference between the two studies.

There was no significant changes of the elastic properties from 60 to 80% along femur length in all quadrants of both microscopic and mesoscopic scale. The variations are only between 20 to 60% of femur length. These variations of elastic coefficients reflect the different mechanical loads and type of muscle attached affecting fibril orientation and elastic properties. Duda's mathematical model [184] showed that mechanical stress like, muscle force affects the elastic properties of bone. In the posterior–lateral region, the vastus lateralis is connected between 15% and 80% of femur length (Fig. IV.1b). Their mechanical force

effects the Haversian remodelling and that is represented by the variation of elastic coefficients along this long axis. It has been shown in our study that axial elastic coefficients and anisotropy ratio increase from proximal to distal in the posterior and lateral regions along femur length [33]. In the anterior region, vastus intermedius is connected between 10% and 60% of femur length (Fig. IV.1a). The elastic constants are higher in the anterior quadrant than other quadrants in this region. The elastic coefficient showed the significant change in the muscle attached region. Nearly constant elastic coefficients values occurs at more distal sections, where the muscle is connected only at the posterior/lateral region. The variation of DMB and elastic coefficients along the femoral length was slightly opposite to trends in maximum strains calculated by numerical models, with the maxima near section close to the proximal and increasing towards the distal [184;185].

Martin and Atkinson [186] found that in the femur diaphysis, corresponding to sections 40 – 60% in the present study, was stronger in medial-lateral bending than in anterior-posterior bending. Kimura and Amtmann [187] also observed reduced compression strength in the AP plane relative to the ML plane at the same approximate positions. This is reflected in our results where the medial, lateral anterior quadrants (sections 40 – 60%) had greater elastic coefficient and density values was higher in the medial and lateral quadrants.

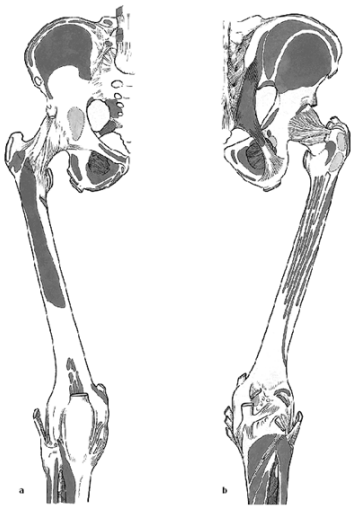

a) *b)*

Figure IV.1 *Muscle attachment on human femur. a) vastus intermedius is attached in anterior region and b) vastus lateralis is attached in posterior – lateral region [188].*

In the distal region, the extensor and flexor muscles produce large anterior-posterior bending moments. There is also an increase in the AP bending stress from proximal to distal

in the human femur. The femoral elastic properties change accordingly, and as shown in the present study the anisotropic ratio reached maximum at the midshaft region for all the anatomical quadrants except for the posterior. Local variations of elastic coefficients from the endosteal to the periosteal related to bone remodelling. But, for old femur used in our study, there was no significant variation of elastic properties along the radial direction, only the last section close to periosteum showed lower values.

The detailed locally-assessed data in this study may serve as a real-life input for the numerical 3-D FE simulation models instead of the commonly used assumption that bone tissue is homogeneous and isotropic. Moreover, assessment of changes of local tissue anisotropy may provide new insight in studies of bone remodelling, e.g., in the course of fracture healing, bone pathologies, aging, or adaptation to modified loading conditions at the bone-implant interface after endoprosthetic surgeries.

IV.1.3 Relations of elastic constants with structural parameters and tissue mineralization

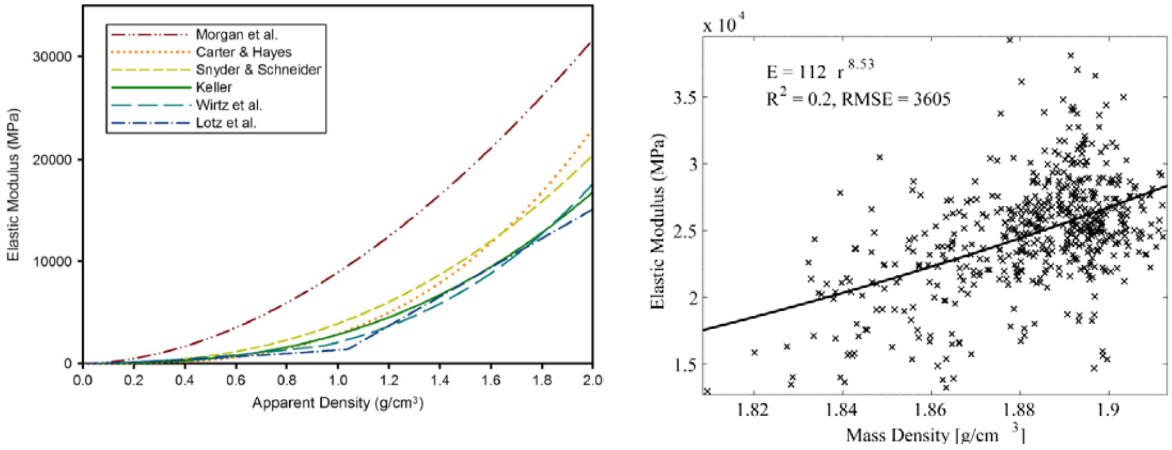

a) *b)*

Figure IV.2 *a) Graphical representation of the six different density – modulus equations that were trailed in each bone from Austman et al. (2008) and b) from this study.*

The relation of both microscopic and mesoscopic elastic coefficients with structural parameters and tissue degree of mineralization are shown in Table III.9. Several empirical or mathematical models have been developed to predict bone elasticity from the degree of mineralization (Fig. IV.2a) [23]. Since the elastic coefficients depend on density and sound velocity, both bone mineral content and microstructure will affect the estimated coefficient.

The results confirm previous findings that degree of mineralization is only weakly correlated with elastic properties (R^2 = 0.17 - 0.24). The variation in the relation can be due to different fibril orientations, embedding, or other differences in the collagenous organic matrix. The elastic modulus of hydroxyapatite crystals and collagen matrix are vastly different, and factors such as mineral crystal and collagen fibril orientations are main factors that affect the tissue elastic properties. The mechanical anisotropy at tissue level is due to the preferred collagen fibril orientation with the principal loading direction of bone. It is well accepted that porosity has a strong impact on macroscopic elastic properties of cortical bone as shown in this study. In particular, the highly oriented system of Haversian canals does not only affect the absolute elastic coefficient values, but also the macroscopic degree of elastic anisotropy [28;189].

IV.2 Skeletal muscle

Many pathological conditions exhibit a change in mechanical and structural properties of muscle. In this study, the meat quality trait related tissue composition mainly focused on the estimation of intramuscular fat content using non-destructive ultrasound technique. First studies have either measured the sound velocity [68;69] or have analyzed the texture of the gray scale backscatter images [58;70]. Although these methods have been quite successful in the prediction of IMF in living steers and hot carcasses [70-72], the studies performed in porcine muscle were less predictive [73;74]. During the last decade, spectral analysis of the backscattered ultrasound signals has been shown to provide more detailed information about tissue constitution compared to conventional image texture or sound velocity analyses [73-76]. But it is not clear to what degree the oriented structures of muscle contribute to ultrasonic propagation properties. Many different backscatter models have been proposed to extract statistically averaged information from the backscattered radio frequency signals measured within a distinct tissue volume. The accuracy of microstructural tissue features estimation can be increase with some model parameters restriction, e.g., with a prior knowledge of scatter size, density and relative acoustic impedance change. The discussion is arranged in three parts: tissue level, macro molecular level acoustic properties in porcine muscle in vitro and ultrasonic propagation and scattering properties in vivo.

IV.2.1 Tissue level acoustic properties in porcine muscle *in vitro*

The anisotropies of acoustic propagation parameters and material parameters of porcine *m. longissimus* were analyzed at the level of individual fibers at high resolution, using a 100 MHz time resolved scanning acoustic microscope. To avoid thickness assumptions cepstrum analysis of RF signal was used for the thickness estimation of a 50 µm thick sample. In this study, acoustic parameters were mainly estimated within the fibers and only a few bundles were involved.

Significant differences of ultrasonic propagation parameters were observed between parallel and perpendicular fiber directions. In agreement with previous investigations, speed of sound and attenuation coefficient measured parallel to the fibers revealed higher values than those measured perpendicular to the fiber direction [87;87;162;164;190]. Among the measured acoustic parameters, attenuation had the strongest direction dependence. The attenuation anisotropy found in this study was slightly higher compared to earlier measurements on *longissimus* dorsi, psoas major and lobster extensor, which showed ratios of 1.56 to 1.82 [87], frozen and bovine skeletal muscle [190;191], and fresh canine myocardium, which showed ratios of 1.9 to 3.4. In all cases the difference between speed of sound measured parallel and perpendicular to the sound propagation direction is on the order of 1.02, which is comparable with the range provided in Smith 1996 [87].

Anisotropic properties of material parameters (impedance, elastic coefficients and density of muscle) have also been investigated in this study. All the material parameters are significantly higher along the fiber orientation compared to the perpendicular direction. Only a few studies are available targeting elastic coefficients of muscle tissue at macroscopic level [162;192;193]. The elastic coefficients and their anisotropic ratio of porcine *longissmus* muscle was higher than on human myocardium [193] and lower than the formalin fixed bovine tendon [192]. As shown in the bone study, acoustic impedance is excellent proxy for the muscle stiffness coefficient (R^2 = 0.71, RMSE = 0.02) compared to density (R^2 = 0.11, RMSE = 0.05).

The acoustic properties of different muscle fiber types were also compared by using the image registration method with histology image. Even though the differences of sound speed within the fiber type were not significant, the slightly lower sound velocity values of STO compared to FTG and FTO fibers may be reasoned in higher fat content and lower

protein content in STO muscle fiber type [194]. Positive relationships between sound velocity and protein content have already been shown in human blood [195].

Fiber level acoustic parameters did not show any significant correlation with tissue compositions as shown in the other studies [120]. However, this could be explained by the fact that intramuscular fat is mainly associated with connective tissue covering primary muscle bundles. In this study, acoustic parameters were mainly estimated within the fibers and only a few bundles were involved. The negative relation between dry matter and acoustic parameters is contrary to earlier findings, where a higher amount of water was related to a decreasing sound speed and attenuation in both fiber parallel and perpendicular directions in porcine muscle [87]. However, this could be explained by in methodical differences and tissue type. First, the use of PBS as a coupling medium may have affected the sample balancing the loss of water during storage time, and handling (e.g., freezing, storage, temperature) may highly affect the amount of water and therefore also the acoustic parameters.

To our knowledge, this is the first study providing both ultrasonic propagation properties and material properties of skeletal muscle at tissue level at close to *in vivo* conditions. These parameters depend on the tissue compositions and structural parameters of tissue. The echo intensity distribution obtained from *in vivo* ultrasound image has been used to investigate tissue behaviour during the disease state in clinical applications, and fat content in muscle in the meat industries. This echo intensity is determined by the difference of acoustic impedance between neighbouring tissues. This study will give more details for proper interpretation in the *in vivo* ultrasound analysis. The measurement techniques used in this study can be applied in other tissue types; for example, cartilage and tendon have a higher college fiber alignment which affects their mechanical behaviour in different direction.

The embedding material [196] or cover slip [87;165] which can affect the acoustic parameters slightly was not applied in this study. The RF signals used for estimation of acoustic parameters are only from the tissue. However, the measurement system is not able to estimate the acoustic parameters when the surface reflection is weak or the thickness is approximately thinner than axial resolution of the transducer, because the two reflections from sample and substrate surfaces cannot be separated with the cepstrum method [176;196]. The range of tissue compositions and number of samples used in this study is comparatively

smaller than in the previous studies [87]. To improve the analysis of variation of acoustic and material parameters with tissue composition, structural parameters and different fiber types, more samples have to be investigated with a broad range of chemical and structural parameters.

IV.2.2 Macro molecular level acoustic properties in porcine muscle *in vitro*

The molecular level acoustic propagation parameters of porcine *m.longissimus* were analyzed with muscle fiber orientation similar to the measurements on the intact carcass using a 10 MHz time resolved scanning acoustic microscope. The ultrasound parameters estimated at molecular level were related to the set of structural and compositional traits of the muscle samples under investigation. Sound velocity in fresh beef muscle measured along the fiber axis has been reported to be negatively correlated with IMF (r = -0.82) [76]. This could be confirmed by our work for porcine muscle samples measured 24 h.p.m. (r = -0.50). The higher correlations mentioned by Park et al.[76] may be due to the considerably higher IMF range in bovine muscle (~ 2-14%).

In terms of *in vivo* ultrasound measurement correction algorithms, the obtained relationships between compositional parameters and sound velocity are promising. Besides IMF the given sound velocity values can be considered to be mostly independent from the compositional parameters investigated in this study. Correlations of sound velocity with e.g., protein content or histological traits (not shown) are always minor and never exceed r = 0.41. Furthermore, auto-correlations between compositional parameters (e.g., protein) and IMF may cause correlations with sound velocity. Overall, the low coefficient of variation (~ 0.3%) of sound velocity indicates only a minor effect of muscle structure and composition. Therefore, while sound velocity seems to be unsuitable for IMF determination in porcine muscle as stated for bovine muscle or hashed meat, the obtained dataset can be used as reference.

Attenuation was found to be strongly correlated with IMF (r = 0.66). These findings are in accordance with previous investigations in porcine muscle reporting about 50 % higher attenuation in groups with high IMF level [89]. Relationships between the amount of IMF and the attenuation have also been published for beef muscle as a decreasing attenuation with increasing water content[87]. Minor positive relationships with dry matter obtained during our investigations confirm these findings.

Contrary to sound velocity, the attenuation seems to be more influenced by IMF. The measured coefficient of variation ranges between 25 and 30%, which is about 100 times higher than that for sound velocity. Therefore, the usability of attenuation predicting the IMF content in loin muscle as already reported in literature [87;89] can be proven by our results. As a further advantage, the attenuation was mostly unaffected by compositional parameters (including histological differences) besides IMF. Only pH, drip loss, and the amount of FTG fibers showed additional minor influences on the attenuation of the native samples. All of these relationships however, are rather small compared to those between attenuation and IMF and can partially be explained by correlations with the IMF causing an auto-correlation between attenuation and the amount of FTG fibers, for example. Therefore, the majority of the investigated parameters can be considered to either not influence the attenuation of the loin muscle or to be already described by the influence of the IMF. These findings will help to classify ultrasound measurements intending to predict compositional traits of muscle.

IV.2.3 Non-destructive muscle characteristics estimation

In this study, muscle characteristics were investigated non-destructively using a quantitative ultrasonic device by spectral analysis of ultrasonic echo signals. The sound field correction has been done by including the wavefront curve compensation using a normalized known phantom AIB distribution and finding the exact reference position while sound propagating through the biological tissue medium. In the previous studies, acoustic properties of the prelayered medium (medium between ultrasonic transducer and region of interest) were assumed or excluded, which will affect the RF signal in ROI. Here, those prelayered medium effect corrections were improved by the calculation of their thickness and SOS from the RF TOFs itself. In addition to the spectral parameters used in previous studies for estimation of tissue characteristics [77;78;197], the cepstral parameters are also extracted from the RF signals, which are independent of any intermediate mediums effect compensation.

The ultrasonic parameters estimated in this study show moderate correlations with tissue composition and structural parameters (Table III.17). A moderate positive relationship with the IMF has been found for TOF_{BFcomd}. Our previous study [120], showed only a weak relation between SOS_{BFcomd} and muscle compositions. So, change in TOF_{BFcomd} may be mostly due to their thickness. Muscle attenuation revealed a high correlation with IMF confirming our SAM (Sec. III.B.3.2) and earlier results [89]. Only a few studies have reported relations between IMF and spectral and cepstral parameters. Mörlein et al. [89]

analyzed a wide range of parameters obtained with the medical ultrasound device of center frequency 3.5 MHz. While Mörlein stated no significant relationships between IMF and cepstral parameters, the present study reports correlations of up to r = 0.29. Procedural differences (e.g., the used frequency or the signal processing) have affected the results.

The IMF deposition in the perimysium during fattening of the muscle disorganizes and breaks down the honeycomb structure of endomysia. That decreases the mechanical strength of the muscle [53;198]. A reduction in mechanical strength due to increased IMF [53;198] can therefore be considered to affect the ultrasonic backscatter intensity due to differences in scatter size, structure and elastic properties, i.e. acoustic impedance of the connective tissue. Midband fit and AIB are associated with the size and the acoustic impedance of the scattering structures [81;82]

Structural parameter, fiber diameter revealed a moderate correlation with the estimated parameters. The findings suggested that the backscatter parameters most affected by fiber diameter (scatter size) than ultrasonic propagation properties like attenuation and speed of sound [120]. As shown in the backscatter model proposed by Lizzi et al. [199], the slope of the obtained power spectrum (m) is related to the size and midband fit (M) and spectral intercept are affected by size, concentration, and impedance of the scatterers. Here, the fiber diameter has a very weak negative correlation with the spectral slope. This can be explained by the varying fiber orientation angle. As all the measurements were performed on hog carcass, the angle differed between the animals and an exact determination was not possible. The scattering strength represented by midband fit and AIB depends on multiple factors, including fiber diameter, concentration and relative acoustic impedance between fiber and the surrounding medium, here connective tissue. The increase of IMF will reduce the fiber diameter, which could be the reason for the inverse correlation of fiber diameter, and IMF with spectral parameters midband fit and AIB. The cepstral parameter τ_{max} represents the scatterer diameters and distances depending on the axial resolution of the ultrasonic system [176]. However, the weak correlation between τ_{max} and bundle diameter in this study could be due to the muscle ROI size, and the number of bundles taken into account for histology and ultrasonic analysis were different and the fiber orientation angle with respect to sound propagation may vary within the animals.

The obtained linear correlations suggest the feasibility to predict the IMF content. Promising candidates for IMF prediction were found among the estimated spectral parameters. In the present investigation multiple linear regression yielded an R^2 of .76 and an RMSE of 0.34% IMF. In the previous investigation [89], IMF could be predicted with a large set of spectral parameters using partial least-squares regression (R2 = 0.58, RMSE = 0.36%). In contrast to spectral analysis, image analysis of *in vivo* ultrasound scans allowed the prediction of porcine loin IMF with R^2 of 0.48 and an RMSE of 0.71% IMF [200] and R^2 = 0.32; RMSE: 1.02%) [73]. B-mode image analysis of bovine *longissimus* muscle scans resulted in R^2 values comparable to the present investigation (up to 0.75) [58;70]. Higher R^2 in beef may be due to the broader IMF range (from 1% to more than 11%) of bovine muscle [70]. Compared to the previous study [89], the number of acoustic parameters needed for IMF prediction could be reduced. This could be achieved by improved algorithms for ultrasound data pre-processing to correct system specific and intermediate tissue effects. Furthermore, the ability to correctly classify 73% of the carcasses into 3 IMF groups (thresholds at 1 and 2%) proves the practical use of ultrasound spectral analysis. The correct classification of 92% of all carcasses into 2 classes is a further improvement to earlier investigations in which nearly 80% of the carcasses were classified into 2 IMF groups (threshold at 2% IMF) using discriminant analysis [89].

In this study, we have been able to show that different spectroscopic variables extracted from ultrasound backscattering can be related to muscle composition and structural parameters by analyzing spectral and cepstral parameters in the backscatter ultrasound. All the system dependent correction measurements were carried out at temperature of 38°C. The results suggest that the proposed method is feasible for non-invasive IMF estimation in commercial abattoirs. The IMF is mainly associated with connective tissue covering primary muscle bundles. It is well known that the mechanical properties of dystrophic muscle vary significantly with progression of the disease. These changes have been related to an increase in connective tissue content and changes in structural properties [52]. With the simultaneous estimation of spectral and cepstral parameters, which are affected by tissue composition and structural parameters, future muscular dystrophy diagnosis techniques can be improved using the proposed spectral analysis method. However, the correlation used for intermediate tissue effect correlations was estimated from porcine *longissimus* muscle, which is not feasible for other muscle types [119].

V Summary

A musculoskeletal system is an important organ system that gives the ability to move the body. It is made of bone, muscles, cartilage, tendon, ligaments, joints and connective tissue. Its primary functions are supporting the body, protecting vital organs and allowing motion. The large tissue part involving for this functional properties in this system are bone and muscle. Both bone and muscle have the highly oriented underlying extracellular matrix structure to perform mechanical and biological functions. Many pathological conditions such as physical condition, age, genetic background and treatment change the mechanical and structural properties of both tissues. There are a number of clinical imaging techniques that are used to assess the functional properties of musculoskeletal tissues in every day clinical diagnosis. Among them, ultrasound technique shows considerably more promise for tissue characterization within a clinical setting. For clear understanding the influence of various pathological conditions on biological system, the micro architecture and functional properties of that system at tissue level should be analyzed. The ultrasonic technique has an advantage to assess those properties at multiple-scale.

Stiffness is one important characteristic of bone material biomechanical competence. It is a material arranged in different hierarchical levels according to the structural components involved. Major components of the cortical bone are mineral crystal, collagen molecules and water. Structural features on lower levels serve as the building blocks for higher levels. Each hierarchical level contributes to the overall mechanical properties as a whole. The femur is the longest, strongest and heaviest bone in the human body. It is one of the principal load bearing bones in the lower extremity [40]. It is a common skeletal site of fracture in elderly people. To understand the mechanisms involved in bone alteration due to several conditions, not only bone quantity but also bone quality have to be characterized at tissue level.

In this study, the elastic properties for a human femur were measured in detail using a new cylindrical shaped sample ultrasonic scanning procedure at microscopic level. The results showed that bone tissue is anisotropic and varies depending on the anatomical location. Because sample preparation, measurement and data analysis are straight forward, systematic screening studies are realistic. The scalar quantity, degrees of mineralization was determined by synchrotron radiation μCT measurement. The results confirm previous findings that degree of mineralization is only moderately correlated with tissue elastic

properties, and their coefficients of variation are comparatively smaller than tissue elastic properties. The mechanical anisotropy at microscopic level is due to the preferred collagen fibril orientation with the principal loading direction of bone. It is well accepted that porosity has a strong impact on the macroscopic elastic properties of cortical bone. In particular, the highly oriented system of Haversian canals does not only affect the absolute elastic values, but also the macroscopic degree of elastic anisotropy. The mesoscopic anisotropic stiffness matrixes were estimated by the combination of microscopic stiffness matrix of bone tissue, determined from the cylinder measurement and porosity by an asymptotic homogenization model. As shown in the previous findings, pore inclusion in bone matrix reduces the elastic efficiency and increases the degree of elastic anisotropy.

The detailed locally-assessed data in this study may serve as a real-life input for numerical 3-D FE simulation models instead of the commonly used assumption that bone tissue is homogeneous and isotropic. Moreover, assessment of changes of local tissue anisotropy may provide new insight in research of bone remodeling, e.g., in the course of fracture healing, bone pathologies, aging, or adaptation to modified loading conditions at the bone-implant interface after endoprosthetic surgeries.

Muscle is the composition of multiple bundles of muscle fibers binded together by connective tissue. It contains water, proteins, lipids, carbohydrates and minerals. The fibers of muscle are made up of a number of different proteins arranged in a very specific manner. Muscle contraction takes place when force is produced by the shortening of muscle fiber which causes the movement of bone. Meat industrial interest in the muscle structure and constituents of skeletal muscle is concerned with the nutritional value of the tissue. The quality of the meat is related to the marbling or the amount of fat in the tissue. Muscles with a reasonable percentage of fat are ranked as more tender and favorable. The ability to accurately determine the quality of meat based on tissue composition has great economic value to the meat industry.

Pork is the most important meat in Germany with approximately 60 kg consumed per capita and year. The intramuscular fat content, IMF is widely regarded as one of the major parameters influencing qualify and sensory characteristics of meat. In this study, IMF of the *m.longissimus* on suspended pig carcasses was predicted non-invasively using a quantitative ultrasonic device and ultrasonic properties were analyzed at fiber level. The structural

properties like muscle fiber size, geometry and their distribution, ultrasonic propagation parameters, e.g., speed of sound and attenuation, and material properties, e.g., elastic coefficient and apparent density and their behavior with respect to tissue composition and fiber orientation of muscle in fiber level were analyzed at *in vivo* conditions using a high resolution time resolved scanning acoustic microscope. The acoustic properties of individual fiber types have also been analyzed for the first time. As shown in the previous studies, for all parameters except scalar quantity, apparent density showed the higher values along the fiber than perpendicular. Among those, attenuation has the most direction dependency. The acoustic parameters were not affected by fiber types.

The meat quality parameter, the IMF estimation model was developed non-destructively using a quantitative ultrasonic device by analyzing the frequency dependent spectral parameters. The compensation function for the system transfer function and intermediate medium effect correction for data analysis has been improved. The simultaneous estimation of tissue composition and structural parameters with this technique can provide more information about tissue characteristics in clinical application. The data provided at tissue level and investigated ultrasound backscattering from muscle tissue, can be used in a numerical simulation FE model for acoustical backscattering from muscle for the further improvement of diagnostic methods and equipment.

This research represents the detailed ultrasonic characterization of musculoskeletal tissues at microscopic and macroscopic level, with respect to their composition, for further improvement of diagnostic methods.

VI References

[1] P. Zioupos, "Ageing human bone: factors affecting its biomechanical properties and the role of collagen," *J. Biomater. Appl.*, vol. 15, no. 3, pp. 187-229, 2001.

[2] P. Zioupos and J. D. Currey, "Changes in the stiffness, strength, and toughness of human cortical bone with age," *Bone*, vol. 22, no. 1, pp. 57-66, 1998.

[3] P. Laugier and G. Haiat, *Bone Quantitative Ultrasound*. London: Springer, 2011.

[4] K. Raum, I. Leguerney, F. Chandelier, M. Talmant, A. Saied, F. Peyrin, and P. Laugier, "Site-matched assessment of structural and tissue properties of cortical bone using scanning acoustic microscopy and synchrotron radiation muCT," *Phys. Med. Biol.*, vol. 51, no. 3, pp. 733-746, 2006.

[5] G. Boivin and P. J. Meunier, "Effects of bisphosphonates on matrix mineralization," *J. Musculoskelet. Neuronal. Interact.*, vol. 2, no. 6, pp. 538-543, 2002.

[6] G. Boivin and P. J. Meunier, "The mineralization of bone tissue: a forgotten dimension in osteoporosis research," *Osteoporos. Int.*, vol. 14 Suppl 3, p. S19-S24, 2003.

[7] M. Saito, K. Fujii, S. Soshi, and T. Tanaka, "Reductions in degree of mineralization and enzymatic collagen cross-links and increases in glycation-induced pentosidine in the femoral neck cortex in cases of femoral neck fracture," *Osteoporos. Int.*, vol. 17, no. 7, pp. 986-995, 2006.

[8] S. Judex, R. Garman, M. Squire, L. R. Donahue, and C. Rubin, "Genetically based influences on the site-specific regulation of trabecular and cortical bone morphology," *Journal of Bone and Mineral Research*, vol. 19, no. 4, pp. 600-606, 2004.

[9] T. M. Link and S. Majumdar, "Current diagnostic techniques in the evaluation of bone architecture," *Curr. Osteoporos. Rep.*, vol. 2, no. 2, pp. 47-52, 2004.

[10] S. Nuzzo, M. H. Lafage-Proust, E. Martin-Badosa, G. Boivin, T. Thomas, C. Alexandre, and F. Peyrin, "Synchrotron radiation microtomography allows the analysis of three-dimensional microarchitecture and degree of mineralization of human iliac crest biopsy specimens: effects of etidronate treatment," *J. Bone Miner. Res.*, vol. 17, no. 8, pp. 1372-1382, 2002.

[11] P. Roschger, P. Fratzl, J. Eschberger, and K. Klaushofer, "Validation of quantitative backscattered electron imaging for the measurement of mineral density distribution in human bone biopsies," *Bone*, vol. 23, no. 4, pp. 319-326, 1998.

[12] C. E. Hoffler, K. E. Moore, K. Kozloff, P. K. Zysset, M. B. Brown, and S. A. Goldstein, "Heterogeneity of bone lamellar-level elastic moduli," *Bone*, vol. 26, no. 6, pp. 603-609, 2000.

[13] P. K. Zysset, X. E. Guo, C. E. Hoffler, K. E. Moore, and S. A. Goldstein, "Elastic modulus and hardness of cortical and trabecular bone lamellae measured by nanoindentation in the human femur," *J. Biomech.*, vol. 32, no. 10, pp. 1005-1012, 1999.

[14] N. J. Wachter, P. Augat, G. D. Krischak, M. Mentzel, L. Kinzl, and L. Claes, "Prediction of cortical bone porosity in vitro by microcomputed tomography," *Calcif. Tissue Int.*, vol. 68, no. 1, pp. 38-42, 2001.

[15] N. J. Wachter, G. D. Krischak, M. Mentzel, M. R. Sarkar, T. Ebinger, L. Kinzl, L. Claes, and P. Augat, "Correlation of bone mineral density with strength and microstructural parameters of cortical bone in vitro," *Bone*, vol. 31, no. 1, pp. 90-95, 2002.

[16] V. Bousson, F. Peyrin, C. Bergot, M. Hausard, A. Sautet, and J. D. Laredo, "Cortical bone in the human femoral neck: three-dimensional appearance and porosity using synchrotron radiation," *J. Bone Miner. Res.*, vol. 19, no. 5, pp. 794-801, 2004.

[17] S. Hengsberger, J. Enstroem, F. Peyrin, and P. Zysset, "How is the indentation modulus of bone tissue related to its macroscopic elastic response? A validation study," *J. Biomech.*, vol. 36, no. 10, pp. 1503-1509, 2003.

[18] F. Peyrin, C. Muller, Y. Carillon, S. Nuzzo, A. Bonnassie, and A. Briguet, "Synchrotron radiation microCT: a reference tool for the characterization of bone samples," *Adv. Exp. Med. Biol.*, vol. 496, pp. 129-142, 2001.

[19] L. Pothuaud, A. Laib, P. Levitz, C. L. Benhamou, and S. Majumdar, "Three-dimensional-line skeleton graph analysis of high-resolution magnetic resonance images: a validation study from 34-microm-resolution microcomputed tomography," *J. Bone Miner. Res.*, vol. 17, no. 10, pp. 1883-1895, 2002.

[20] G. Boivin and P. J. Meunier, "The degree of mineralization of bone tissue measured by computerized quantitative contact microradiography," *Calcif. Tissue Int.*, vol. 70, no. 6, pp. 503-511, 2002.

[21] C. Hellmich, J. F. Barthelemy, and L. Dormieux, "Mineral-collagen interactions in elasticity of bone ultrastructure - a continuum micromechanics approach," *European Journal of Mechanics A-Solids*, vol. 23, no. 5, pp. 783-810, 2004.

[22] R. M. Pidaparti, A. Chandran, Y. Takano, and C. H. Turner, "Bone mineral lies mainly outside collagen fibrils: predictions of a composite model for osteonal bone," *J. Biomech.*, vol. 29, no. 7, pp. 909-916, 1996.

[23] R. L. Austman, J. S. Milner, D. W. Holdsworth, and C. E. Dunning, "The effect of the density-modulus relationship selected to apply material properties in a finite element model of long bone," *J. Biomech.*, vol. 41, no. 15, pp. 3171-3176, 2008.

[24] C. H. Turner, J. Rho, Y. Takano, T. Y. Tsui, and G. M. Pharr, "The elastic properties of trabecular and cortical bone tissues are similar: results from two microscopic measurement techniques," *J. Biomech.*, vol. 32, no. 4, pp. 437-441, 1999.

[25] K. Raum, R. O. Cleveland, F. Peyrin, and P. Laugier, "Derivation of elastic stiffness from site-matched mineral density and acoustic impedance maps," *Phys. Med. Biol.*, vol. 51, no. 3, pp. 747-758, 2006.

[26] J. Xu, J. Y. Rho, S. R. Mishra, and Z. Fan, "Atomic force microscopy and nanoindentation characterization of human lamellar bone prepared by microtome sectioning and mechanical polishing technique," *J. Biomed. Mater. Res. A*, vol. 67, no. 3, pp. 719-726, 2003.

[27] K. Raum, J. Reisshauer, and J. Brandt, "Frequency and resolution dependence of the anisotropic impedance estimation in cortical bone using time-resolved scanning acoustic microscopy," *J Biomed. Mater. Res.*, vol. 71A, no. 3, pp. 430-438, 2004.

[28] J. Y. Rho, P. Zioupos, J. D. Currey, and G. M. Pharr, "Microstructural elasticity and regional heterogeneity in human femoral bone of various ages examined by nano-indentation," *J. Biomech.*, vol. 35, no. 2, pp. 189-198, 2002.

[29] A. Basillais, S. Bensamoun, C. Chappard, B. Brunet-Imbault, G. Lemineur, B. Ilharreborde, M. C. Ho Ba Tho, and C. L. Benhamou, "Three-dimensional characterization of cortical bone microstructure by microcomputed tomography: validation with ultrasonic and microscopic measurements," *J. Orthop. Sci*, vol. 12, no. 2, pp. 141-148, 2007.

[30] S. Bensamoun, M. C. Ho Ba Tho, S. Luu, J. M. Gherbezza, and J. F. de Belleval, "Spatial distribution of acoustic and elastic properties of human femoral cortical bone," *J. Biomech.*, vol. 37, no. 4, pp. 503-510, 2004.

[31] Y. Yamato, M. Matsukawa, T. Otani, K. Yamazaki, and A. Nagano, "Distribution of longitudinal wave properties in bovine cortical bone in vitro," *Ultrasonics*, vol. 44 Suppl 1, p. e233-e237, 2006.

[32] J. Litniewski, "Determination of the elasticity coefficient for a single trabecula of a cancellous bone: scanning acoustic microscopy approach," *Ultrasound Med. Biol.*, vol. 31, no. 10, pp. 1361-1366, 2005.

[33] S. Weiss, M. C. Zimmerman, R. D. Harten, F. G. Alberta, and A. Meunier, "The acoustic and structural properties of the human femur," *Journal of Biomechanical Engineering-Transactions of the Asme*, vol. 120, no. 1, pp. 71-76, 1998.

[34] K. Raum, T. Hofmman, I. Leguerney, A. Saied, F. Peyrin, L. Vico, and P. Laugier, "Variations of microstructure, mineral density and tissue elasticity in B6/C3H mice," *Bone*, vol. in preparation 2006.

[35] T. Hofmann, F. Heyroth, H. Meinhard, W. Franzel, and K. Raum, "Assessment of composition and anisotropic elastic properties of secondary osteon lamellae," *J. Biomech.*, vol. 39, pp. 2282-2294, 2006.

[36] S. Lakshmanan, A. Bodi, and Raum.K, "Assessment of Anisotropic Tissue Elasticity of Cortical Bone from High-Resolution, Angular Acoustic Measurements," *IEEE Trans. Ultrason. , Ferroelect. , Freq. Contr.*, vol. 54, no. 8, pp. 1560-1570, 2007.

[37] K. Raum, I. Leguerney, F. Chandelier, E. Bossy, M. Talmant, A. Saied, F. Peyrin, and P. Laugier, "Bone microstructure and elastic tissue properties are reflected in QUS axial transmission measurements," *Ultrasound Med. Biol.*, vol. 31, no. 9, pp. 1225-1235, 2005.

[38] H. Platzer, "[Nation-wide program for the prevention of atherosclerosis. Physicians, patients and health insurance carriers must all pull together]," *MMW. Fortschr. Med.*, vol. 145, no. 13, pp. 37-38, 2003.

[39] C. Whittle, W. Martinez, G. Baldassare, G. Smoje, K. Bolte, D. Busel, and S. Gonzalez, "[Pilomatrixoma: ultrasound diagnosis]," *Rev. Med. Chil.*, vol. 131, no. 7, pp. 735-740, 2003.

[40] C. C. Asplund and T. J. Mezzanotte, "Midshaft femur fractures in adults,". P. W. Eiff, Ed. Wolters Kluwer Health: www.uptodateonline.com, 2009.

[41] N. Binkley, J. Bilezikian, D. Kendler, E. Leib, E. Lewiecki, and S. Petak, "Official positions of the international society for clinical densitometry and executive summary of the 2005 position development conference," *Journal of clinical densitometry*, vol. 9, pp. 4-14, 2006.

[42] M. T. Cuddihy, S. E. Gabriel, C. S. Crowson, E. J. Atkinson, C. Tabini, and W. M. OFallon, "Osteoporosis intervention following distal forearm fractures: a missed opportunity?," *Archives of Internal Medicine*, vol. 162, pp. 421-426, 2002.

[43] P. Haentjens, O. Johnell, J. A. Kanis, R. Bouillon, C. Cooper, G. Lamraski, D. Vanderschueren, J. M. Kaufman, and S. Boonen, "Evidence from data searches and life-table analyses for gender-related differences in absolute risk of hip fracture after Colles' or spine fracture: Colles' fractire as an early and sensitive marker of skeletal fragility in white men," *Journal of bone mineral research*, vol. 19, pp. 1933-1944, 2004.

[44] R. Barkmann and C. C. Gluer, "[Quantitative ultrasound]," *Radiologe*, vol. 46, no. 10, pp. 861-869, 2006.

[45] E. Bossy, M. Talmant, M. Defontaine, F. Patat, and P. Laugier, "Bidirectional axial transmission can improve accuracy and precision of ultrasonic velocity measurement in cortical bone: a validation on test materials," *IEEE Trans. Ultrason. Ferroelectr. Freq. Control*, vol. 51, no. 1, pp. 71-79, 2004.

[46] P. H. Nicholson, P. Moilanen, T. Karkkainen, J. Timonen, and S. Cheng, "Guided ultrasonic waves in long bones: modelling, experiment and in vivo application," *Physiol Meas.*, vol. 23, no. 4, pp. 755-768, 2002.

[47] E. Bossy, M. Talmant, F. Peyrin, L. Akrout, P. Cloetens, and P. Laugier, "An in vitro study of the ultrasonic axial transmission technique at the radius: 1-MHz velocity

measurements are sensitive to both mineralization and intracortical porosity," *J. Bone Miner. Res.*, vol. 19, no. 9, pp. 1548-1556, 2004.

[48] R. B. Ashman, S. C. Cowin, W. C. Van Buskirk, and J. C. Rice, "A continuous wave technique for the measurement of the elastic properties of cortical bone," *J. Biomech.*, vol. 17, no. 5, pp. 349-361, 1984.

[49] H. S. Yoon and J. L. Katz, "Ultrasonic wave propagation in human cortical bone--II. Measurements of elastic properties and microhardness," *J. Biomech.*, vol. 9, no. 7, pp. 459-464, 1976.

[50] A. A. Espinoza Orias, J. M. Deuerling, M. D. Landrigan, J. E. Renaud, and R. K. Roeder, "Anatomic variation in the elastic anisotropy of cortical bone tissue in the human femur," *J. Mech. Behav. Biomed. Mater.*, vol. 2, no. 3, pp. 255-263, 2009.

[51] R. P. Gould, *'Muscle Physiology', In The structure and function of muscle*. New York: Bourne, G.H., Ed., Academic Press, 1973.

[52] B. Hete and K. K. Shung, "A study of the relationship between mechanical and ultrasonic properties of dystrophic and normal skeletal muscle," *Ultrasound Med. Biol.*, vol. 21, no. 3, pp. 343-352, 1995.

[53] T. Nishimura, A. Hattori, and K. Takahashi, "Structural changes in intramuscular connective tissue during the fattening of Japanese black cattle: effect of marbling on beef tenderization," *J. Anim Sci*, vol. 77, no. 1, pp. 93-104, 1999.

[54] J. D. Wood, R. I. Richardson, G. R. Nute, A. V. Fisher, M. M. Campo, E. Kasapidou, P. R. Sheard, and M. Enser, "Effects of fatty acids on meat quality: a review," *Meat Science*, vol. 66, pp. 21-32, 2003.

[55] R. H. Edwards, "Studies of muscular performance in normal and dystrophic subjects," *Br. Med. Bull.*, vol. 36, no. 2, pp. 159-164, 980.

[56] J. A. Lucy, "Is there a membrane defect in muscle and other cells?," *Br. Med. Bull.*, vol. 36, no. 2, pp. 187-192, 1980.

[57] T. N. Blumer, M. B. Wise, E. A. Pierce, W. W. G. Smart, and H. B. Craig, "Nature and Variability of Marbling Deposits in Longissimus-Dorsi Muscle of Beef Carcasses," *Journal of Animal Science*, vol. 21, no. 4, p. 935-&, 1962.

[58] J. R. Brethour, "Estimating marbling score in live cattle from ultrasound images using pattern recognition and neural network procedures," *J. Anim Sci.*, vol. 72, no. 6, pp. 1425-1432, 1994.

[59] K. Rosenvold and H. J. Andersen, "The significance of pre-slaughter stress and diet on colour and colour stability of pork," *Meat Science*, vol. 63, pp. 199-209, 2003.

[60] X. Fernandez, G. Monin, A. Talmant, J. Mourot, and B. Lebret, "Influence of intramuscular fat content on the quality of pig meat - 2. Consumer acceptability of m. longissimus lumborum," *Meat Science*, vol. 53, no. 1, pp. 67-72, 1999.

[61] P. J. Blanchard, C. C. Warkup, M. Ellis, M. B. Willis, and P. Avery, "The influence of the proportion of Duroc genes on growth, carcass and pork eating quality characteristics," *Animal Science*, vol. 68, pp. 495-501, 1999.

[62] K. Heylen, "Variation von anatomisch-physiologischen Merkmalen sowie Merkmalen der Fleischqualität im *M. longissimus thoracis et lumborum* des Schweins unter besonderer Berücksichtigung des intramuskulären Fettgehaltes." 1999.

[63] H. Kipfmüller, K. Bodis, W. Peschke, and H. M. Eichinger, "Qualität von Schweinefleisch. Beeinflussung durch das intramuskuläre Fett.," *Ernährungsumschau*, vol. 47, no. 11, pp. 416-422, 2000.

[64] D. Mörlein, G. Link, C. Werner, and M. Wicke, "Suitability of three commercially produced pig breeds in Germany for a meat quality program with emphasis on drip loss and eating quality," *Meat Science*, no. 77, pp. 504-511, 2007.

[65] D. Alomar, C. Gallo, M. Castaneda, and R. Fuchslocher, "Chemical and discriminant analysis of bovine meat by near infrared reflectance spectroscopy (NIRS).," *MEAT SCIENCE*, vol. 63, no. 4, pp. 441-450, 2003.

[66] D. Suster, B. J. Leury, E. Ostrowska, K. L. Butler, D. J. Kerton, J. D. Wark, and F. R. Dunshea, "Accuracy of dual energy X-ray absorptiometry (DXA), weight and P2 back fat to predict whole body and carcass composition in pigs within and across experiments.," *Livestock production science*, vol. 84, no. 3, pp. 231-242, 2003.

[67] G. H. Sorland, P. M. Larsen, F. Lundby, A. P. Rudi, and T. Guiheneuf, "Determination of total fat and moisture content in meat using low field NMR," *Meat Science*, no. 66, pp. 543-550, 2004.

[68] J. Benedito, J. A. Carcel, C. Rossello, and A. Mulet, "Composition assessment of raw meat mixtures using ultrasonics," *Meat Science*, vol. 57, no. 4, pp. 365-370, 2001.

[69] B. Park, A. D. Whittaker, R. K. Miller, and D. S. Hale, "Predicting intramuscular fat in beef longissimus muscle from speed of sound," *J. Anim Sci.*, vol. 72, no. 1, pp. 109-116, 1994.

[70] A. Hassen, D. E. Wilson, V. R. Amin, G. H. Rouse, and C. L. Hays, "Predicting percentage of intramuscular fat using two types of real-time ultrasound equipment," *J. Anim Sci.*, vol. 79, no. 1, pp. 11-18, 2001.

[71] A. Hassen, D. E. Wilson, and G. H. Rouse, "Estimation of genetic parameters for ultrasound-predicted percentage of intramuscular fat in Angus cattle using random regression models," *Journal of Animal Science*, vol. 81, no. 1, pp. 35-45, 2003.

[72] A. D. Whittaker, B. Park, B. R. Thane, R. K. Miller, and J. W. Savell, "Principles of ultrasound and measurement of intramuscular fat," *J. Anim Sci.*, vol. 70, no. 3, pp. 942-952, 1992.

[73] D. W. Newcom, T. J. Baas, and J. F. Lampe, "Prediction of intramuscular fat percentage in live swine using real-time ultrasound," *J. Anim Sci.*, vol. 80, no. 12, pp. 3046-3052, 2002.

[74] H. Ville, G. Rombouts, P. Van Hecke, S. Perremans, G. Maes, G. Spincemaille, and R. Geers, "An evaluation of ultrasound and nuclear magnetic resonance spectroscopy to measure in vivo intramuscular fat content of longissimus muscle of pigs," *J. Anim Sci.*, vol. 75, no. 11, pp. 2942-2949, 1997.

[75] F. L. Lizzi, E. J. Feleppa, S. K. Alam, and C. X. Deng, "Ultrasonic spectrum analysis for tissue evaluation," *Pattern Recognition Letters*, vol. 24, pp. 637-658, 2003.

[76] B. Park, A. D. Whittaker, R. K. Miller, and D. E. Bray, "Measuring intramuscular fat in beef with ultrasonic frequency analysis," *J. Anim Sci.*, vol. 72, no. 1, pp. 117-125, 1994.

[77] B. Banihashemi, R. Vlad, B. Debeljevic, A. Giles, M. C. Kolios, and G. J. Czarnota, "Ultrasound imaging of apoptosis in tumor response: novel preclinical monitoring of photodynamic therapy effects," *Cancer Res.*, vol. 68, no. 20, pp. 8590-8596, 2008.

[78] B. I. Raju and M. A. Srinivasan, "High-frequency ultrasonic attenuation and backscatter coefficients of in vivo normal human dermis and subcutaneous fat," *Ultrasound Med. Biol.*, vol. 27, no. 11, pp. 1543-1556, 2001.

[79] K. Raum, M. Gottwald, D. Wohlrab, and F. Göbel, "Depth dependent high frequency backscatter analysis of degenerated cartilage," *IEEE Ultrasonics Symposium Proceedings*, no. 1, pp. 1109-1112, 2007.

[80] U. Scheipers, H. Ermert, H. J. Sommerfeld, M. Garcia-Schurmann, T. Senge, and S. Philippou, "Ultrasonic multifeature tissue characterization for prostate diagnostics," *Ultrasound Med. Biol.*, vol. 29, no. 8, pp. 1137-1149, 2003.

[81] F. L. Lizzi, M. Astor, T. Liu, C. Deng, D. J. Coleman, and R. H. Silverman, "Ultrasonic spectrum analysis for tissue assays and therapy evaluation.," *Int. J. Imaging Syst. Technol.*, vol. 8, pp. 3-10, 1997.

[82] F. L. Lizzi, S. K. Alam, S. Mikaelian, P. Lee, and E. J. Feleppa, "On the statistics of ultrasonic spectral parameters," *Ultras. in Med & Biol*, vol. 32, no. 11, pp. 1671-1685, 2006.

[83] K. Gelse, A. Olk, S. Eichhorn, B. Swoboda, M. Schoene, and K. Raum, "Quantitative ultrasound biomicroscopy for the analysis of healthy and repair cartilage tissue," *Eur. Cell Mater*, vol. 19, pp. 58-71, 2010.

[84] A. V. Oppenheim and R. W. Schafer, "From Frequency to Quefrency: A History of the Cepstrum,", 1053 ed 2004, pp. 95-106.

[85] B. Essengustavsson, A. Karlsson, K. Lundstrom, and A. C. Enfalt, "Intramuscular Fat and Muscle-Fiber Lipid Contents in Halothane-Gene-Free Pigs Fed High Or

Low-Protein Diets and Its Relations to Meat Quality," *Meat Science*, vol. 38, no. 2, pp. 269-277, 1994.

[86] D. Mörlein, "Bestimmung des intramuskulären Fettgehaltes (IMF) im *M. longissimus* von Schweinen mittels Ultraschall." 2005.

[87] N. B. Smith, "Effect of myofibril length and tissue constituents on acoustic propagation properties of muscle." Ph.D Ph.D, University of Illinois at Urbana-Champaign, 1996.

[88] S. Abou El Karam, B. Buquet, P. Berge, and J. Culioli, "Ultrasonic characterization of bovine muscle," *Proceedings of the 43rd IComST. 27 July to 1 August 1997, Aucland, New Zealand*, pp. 310-311, 1997.

[89] D. Mörlein, F. Rosner, S. Brand, K. V. Jenderka, and M. Wicke, "Non-destructive estimation of the intramuscular fat content of the longissimus muscle of pigs by means of spectral analysis of ultrasound echo signals," *Meat Science*, no. 69, pp. 187-199, 2005.

[90] T. Gärtner, "Ultraschallspektroskopie mit fokussierenden Systemen zur quantitativen Bestimmung von akustischen Parametern." Martin-Luther-Universität; Halle-Wittenberg, 2001.

[91] S. Brand, D. Mörlein, and F. Rosner, "Estimation of intramuscular fat content (IMF) in the muscle longissimus dorsi (LD) of pigs by analysis of RF echo signals obtained from a clinical B-mode device.," *IEEE Ultrason. Symp.*, pp. 8-11, 2002.

[92] M. L. Oelze and W. D. O'Brien, Jr., "Method of improved scatterer size estimation and application to parametric imaging using ultrasound," *J. Acoust. Soc. Am.*, vol. 112, no. 6, pp. 3053-3063, 2002.

[93] M. L. Oelze, J. F. Zachary, and W. D. O'Brien, Jr., "Characterization of tissue microstructure using ultrasonic backscatter: theory and technique for optimization using a Gaussian form factor," *J. Acoust. Soc. Am.*, vol. 112, no. 3 Pt 1, pp. 1202-1211, 2002.

[94] A. G. Reisinger, D. H. Pahr, and P. K. Zysset, "Sensitivity analysis and parametric study of elastic properties of an unidirectional mineralized bone fibril-array using mean field methods," *Biomech. Model. Mechanobiol.*, 2010.

[95] P. Fratzl, H. S. Gupta, E. P. Paschalis, and P. Roschger, "Structure and mechanical quality of the collagen-mineral nano-composite in bone," *Journal of Materials Chemistry*, vol. 14, no. 14, pp. 2115-2123, 2004.

[96] P. Fratzl and R. Weinkamer, "Nature's hierarchical materials," *Progress in Materials Science*, vol. 52, no. 8, pp. 1263-1334, 2007.

[97] J. Y. Rho, L. Kuhn-Spearing, and P. Zioupos, "Mechanical properties and the hierarchical structure of bone," *Med. Eng Phys.*, vol. 20, no. 2, pp. 92-102, 1998.

[98] S. Weiner and H. D. Wagner, "The material bone: Structure mechanical function relations," *Annual Review of Materials Science*, vol. 28, pp. 271-298, 1998.

[99] S. Weiner, W. Traub, and H. D. Wagner, "Lamellar bone: structure-function relations," *J. Struct. Biol.*, vol. 126, no. 3, pp. 241-255, 1999.

[100] S. Nikolov and D. Raabe, "Hierarchical modeling of the elastic properties of bone at submicron scales: the role of extrafibrillar mineralization," *Biophys. J.*, vol. 94, no. 11, pp. 4220-4232, 2008.

[101] M. M. Giraud-Guille, "Twisted plywood architecture of collagen fibrils in human compact bone osteons," *Calcif. Tissue Int.*, vol. 42, no. 3, pp. 167-180, 1988.

[102] W. Wagermaier, H. S. Gupta, A. Gourrier, M. Burghammer, P. Roschger, and P. Fratzl, "Spiral twisting of fiber orientation inside bone lamellae," *Biointerphases*, vol. 1, no. 1, p. 1, 2006.

[103] G. E. Fantner, T. Hassenkam, J. H. Kindt, J. C. Weaver, H. Birkedal, L. Pechenik, J. A. Cutroni, G. A. Cidade, G. D. Stucky, D. E. Morse, and P. K. Hansma, "Sacrificial bonds and hidden length dissipate energy as mineralized fibrils separate during bone fracture," *Nat. Mater.*, vol. 4, no. 8, pp. 612-616, 2005.

[104] U. Akiva, H. D. Wagner, and S. Weiner, "Modelling the three-dimensional elastic constants of parallel-fibred and lamellar bone," *Journal of Materials Science*, vol. 33, no. 6, pp. 1497-1509, 1998.

[105] O. Akkus, "Elastic deformation of mineralized collagen fibrils: An equivalent inclusion based composite model," *Journal of Biomechanical Engineering-Transactions of the Asme*, vol. 127, no. 3, pp. 383-390, 2005.

[106] Y. J. Yoon and S. C. Cowin, "The estimated elastic constants for a single bone osteonal lamella," *Biomech. Model. Mechanobiol.*, vol. 7, no. 1, pp. 1-11, 2008.

[107] I. Jager and P. Fratzl, "Mineralized collagen fibrils: A mechanical model with a staggered arrangement of mineral particles," *Biophysical Journal*, vol. 79, no. 4, pp. 1737-1746, 2000.

[108] S. P. Kotha, S. Kotha, and N. Guzelsu, "A shear-lag model to account for interaction effects between inclusions in composites reinforced with rectangular platelets," *Composites Science and Technology*, vol. 60, no. 11, pp. 2147-2158, 2000.

[109] J. M. Deuerling, W. Yue, A. A. Espinoza Orias, and R. K. Roeder, "Specimen-specific multi-scale model for the anisotropic elastic constants of human cortical bone," *J. Biomech.*, vol. 42, no. 13, pp. 2061-2067, 2009.

[110] Q. Grimal, K. Raum, A. Gerisch, and P. Laugier, "Derivation of the mesoscopic elasticity tensor of cortical bone from quantitative impedance images at the micron scale," *Comput. Methods Biomech. Biomed. Engin.*, vol. 11, no. 2, pp. 147-157, 2008.

[111] T. Hoc, L. Henry, M. Verdier, D. Aubry, L. Sedel, and A. Meunier, "Effect of microstructure on the mechanical properties of Haversian cortical bone," *Bone*, vol. 38, no. 4, pp. 466-474, 2006.

[112] E. Verhulp, B. van Rietbergen, and R. Huiskes, "Comparison of micro-level and continuum-level voxel models of the proximal femur," *J. Biomech.*, vol. 39, no. 16, pp. 2951-2957, 2006.

[113] K. Raum, K. V. Jenderka, A. Klemenz, and J. Brandt, "Multilayer analysis: Quantitative scanning acoustic microscopy for tissue characterization at a microscopic scale," *IEEE Trans. Ultrason. , Ferroelect. , Freq. Contr.*, vol. 50, no. 5, pp. 507-516, 2003.

[114] C. Baron, M. Talmant, and P. Laugier, "Effect of porosity on effective diagonal stiffness coefficients (c(ii)) and elastic anisotropy of cortical bone at 1 MHz: A finite-difference time domain study," *J. Acoust. Soc. Amer.*, vol. 122, no. 3, pp. 1810-1817, 2007.

[115] W. J. Parnell and Q. Grimal, "The influence of mesoscale porosity on cortical bone anisotropy. Investigations via asymptotic homogenization," *J. R. Soc. Interface*, vol. 6, no. 30, pp. 97-109, 2009.

[116] E. N. Marieb, P. B. Wilhelm, and J. B. Mallatt, *Human Anatomy*, 6nd ed. San Francisco: Benjamin-Cummings Publishing company, 2010.

[117] K. Wang, *'Sarcomere-associated cytoskeletal lattices in striated muscle'. In Cell and Muscle Motility*. New York: Shay, J.W. Ed., 1990.

[118] G. Offer and P. Knight, *The structural basis of water-holding in meat part 2: Drip losses*. London: Elsevier Applied Science: In R. Lawrie (Ed.), Developments in meat science, 1988, pp. 172-243.

[119] E. Albrecht, F. Teuscher, K. Ender, and J. Wegner, "Growth- and breed-related changes of muscle bundle structure in cattle," *J. Anim Sci.*, vol. 84, no. 11, pp. 2959-2964, 2006.

[120] T. Koch, S. Brand, L. Sannachi, K. Raum, M. Wicke, and D. Mörlein, "Ultrasound velocity and attenuation of porcine soft tissues with respect to structure and composition: I. Muscle," *Meat Science*, vol. accepted 2010.

[121] A. Briggs, *Acoustic Microscopy*. New York: Oxford University Press, 1992.

[122] B. A. Auld, *Acoustic Fields and Waves in Solids*, 2nd ed. Florida: Krieger Publishing Company, 1990.

[123] R. M. Jones, *Mechanics of composite materials*. New York: McGraw-Hill, 1984.

[124] P. M. Morse and K. U. Ingard, *Theoretical Acoustics*, 2nd ed. New York: McGraw-Hill, 1968.

[125] A. D. Pierce, *Acoustic: An Introduction to its Physical Principals and Applications*, 2nd ed. New York: McGraw-Hill, 1981.

[126] E. Skudrzyk, *The Foundations of Acoustics*, 2nd ed. Wien: Springer, 1971.

[127] F. Morse, *Vibration and Sound*. New York: McGraw-Hill, 1947.

[128] K. Raum, "Quantitative Akustische Rastermikroskopiemethoden zur Charakterisierung der elastischen Eigenschaften von Knochengewebe." Ph.D thesis Martin - Luther - University Halle - Wittenberg, Germany, 2002.

[129] R. Pike and P. Sabatier, *Scattering and inverse scattering in pure and applied science*. London and New York: Academic Press, 2002.

[130] M. F. Insana, T. J. Hall, and J. L. Fishback, "Identifying acoustic scattering sources in normal renal parenchyma from the anisotropy in acoustic properties," *Ultrasound Med. Biol.*, vol. 17, no. 6, pp. 613-626, 1991.

[131] F. L. Lizzi, M. Ostromogilsky, E. J. Feleppa, M. C. Rorke, and M. M. Yaremko, "Relationship of ultrasonic spectral parameters to features of tissue microstructure," *IEEE Trans. Ultrason. Ferroelectr. Freq. Control*, vol. 34, no. 3, pp. 319-329, 1987.

[132] J. Mamou, M. L. Oelze, W. D. O'Brien, Jr., and J. F. Zachary, "Identifying ultrasonic scattering sites from three-dimensional impedance maps," *J. Acoust. Soc. Am.*, vol. 117, no. 1, pp. 413-423, 2005.

[133] J. T. Bushberg, J. A. Seibert, and J. M. Boone, *The essential physics of medical imaging*, 2nd ed. Philadelphia: Lippincot Williams & Wilkins, 2002.

[134] E. P. Papadakis, *Ultrasonic instruments & devices*. San Diego: Academic Press, A harcout science and technology company, 1999.

[135] J. Park and R. S. Lakes, *Biomaterials: an introduction*, 3rd ed. NewYork: Springer Science & Business Media, 2007.

[136] J. A. Kanis, J. P. Devogelaer, and C. Gennari, "Practical guide for the use of bone mineral measurements in the assessment of treatment of osteoporosis: a position paper of the European foundation for osteoporosis and bone disease. The Scientific Advisory Board and the Board of National Societies," *Osteoporos. Int.*, vol. 6, no. 3, pp. 256-261, 1996.

[137] C. Bergot, A. M. Laval-Jeantet, F. Preteux, and A. Meunier, "Measurement of anisotropic vertebral trabecular bone loss during aging by quantitative image analysis," *Calcif. Tissue Int.*, vol. 43, no. 3, pp. 143-149, 1988.

[138] A. M. Parfitt, "Trabecular bone architecture in the pathogenesis and prevention of fracture," *Am. J. Med.*, vol. 82, no. 1B, pp. 68-72, 1987.

[139] G. Y. Boivin, P. M. Chavassieux, A. C. Santora, J. Yates, and P. J. Meunier, "Alendronate increases bone strength by increasing the mean degree of

mineralization of bone tissue in osteoporotic women," *Bone*, vol. 27, no. 5, pp. 687-694, 2000.

[140] S. Nuzzo, F. Peyrin, P. Cloetens, J. Baruchel, and G. Boivin, "Quantification of the degree of mineralization of bone in three dimensions using synchrotron radiation microtomography," *Med. Phys.*, vol. 29, no. 11, pp. 2672-2681, 2002.

[141] S. E. Peters, "Structure and Function in Vertebrate Skeletal-Muscle," *American Zoologist*, vol. 29, no. 1, pp. 221-234, 1989.

[142] V. Horak, "A successive histochemical staining for succinate dehydrogenase and "reversed"-ATPase in a single section for the skeletal muscle fibre typing," *Histochemistry*, vol. 78, no. 4, pp. 545-553, 1983.

[143] LFGB, "Bestimmung des Gesamtfettgehaltes in Fleisch und Fleischerzeugnissen," *Amtliche Sammlung von Untersuchungsverfahren nach 64 LFGB: L 06. 00 6*, 2005.

[144] L. B. Christensen, "Drip loss sampling in porcine m. longissimus dorsi," *Meat Science*, vol. 63, no. 4, pp. 469-477, 2003.

[145] K. Raum and W. D. Obrien, "Pulse-echo field distribution measurement technique for high-frequency ultrasound sources," *IEEE Trans. Ultrason. , Ferroelect. , Freq. Contr.*, vol. 44, no. 4, pp. 810-815, 1997.

[146] S. Hirsekorn, S. Pangraz, G. Weides, and W. Arnold, "Measurement of elastic impedance with high-spatial-resolution using acoustic microscopy," *Applied Physics Letters*, vol. 67, no. 6, pp. 745-747, 1995.

[147] N. Männicke, "Quantitative Ultraschallspektroskopie an hyalinem Gelenkknorpel und phantomen." Diploma thesis Martin - Luther - University Halle - Wittenberg, Germany, 2010.

[148] S. Lakshmanan, A. Bodi, and K. Raum, "Determination of Transverse isotropic stiffness coefficients from high resolution angular acoustic impedance measurements," *5th World Congress of Biomechanics Proceedings*, pp. 35-40, 2006.

[149] P. Laugier, F. Padilla, F. Peyrin, K. Raum, A. T. M. Saied, and L. Vico, "Current trends in the ultrasonic investigation of bone," *ITBM-RBM*, vol. 26, no. 5-6, pp. 299-311, 2005.

[150] T. Hofmann, K. Raum, I. Legeurney, A. Saied, F. Peyrin, L. Vico, and P. Laugier, "Assessment of bone structure and elasticity in B6/C3H mice using high resolution scanning acoustic microscopy," *Ultrasonics*, vol. 44S, pp. 1307-1311, 2006.

[151] B. Preininger, S. Checa, F. Molnar, P. Fratzl, GN. Duda, and K. Raum, "Spatial-temporal mapping of bone structural and elastic properties in a sheep model following osteotomy," *Ultrasound Med. Biol.*, vol. Submitted 2010.

[152] C. Hellmich, F. J. Ulm, and L. Dormieux, "Can the diverse elastic properties of trabecular and cortical bone be attributed to only a few tissue-independent phase

properties and their interactions? Arguments from a multiscale approach," *Biomech. Model. Mechanobiol.*, vol. 2, no. 4, pp. 219-238, 2004.

[153] C. Hellmich and F. J. Ulm, "Are mineralized tissues open crystal foams reinforced by crosslinked collagen? Some energy arguments," *J. Biomech.*, vol. 35, no. 9, pp. 1199-1212, 2002.

[154] Hellmich, "Micromechanical model for ultrastructural stiffness of mineralized tissues," *J. Engi. Mech.* pp. 898-908, 2002.

[155] J. L. Katz and K. Ukraincik, "On the anisotropic elastic properties of hydroxyapatite," *J. Biomech.*, vol. 4, no. 3, pp. 221-227, 1971.

[156] S. Cusack and A. Miller, "Determination of the elastic constants of collagen by Brillouin light scattering," *J. Mol. Biol.*, vol. 135, no. 1, pp. 39-51, 1979.

[157] H. S. Yoon and J. L. Katz, "Ultrasonic wave propagation in human cortical bone-I. Theoretical considerations for hexagonal symmetry," *J. Biomech.*, vol. 9, no. 6, pp. 407-412, 1976.

[158] W. J. Parnell and I. D. Abrahams, "Dynamic homogenization in periodic fibre reinforced media. Quasi-static limit for SH waves," *Wave Motion*, vol. 43, no. 6, pp. 474-498, 2006.

[159] W. J. Parnell and I. D. Abrahams, "Homogenization for wave propagation in periodic fibre-reinforced media with complex microstructure. I - Theory," *Journal of the Mechanics and Physics of Solids*, vol. 56, no. 7, pp. 2521-2540, 2008.

[160] M. Salome, F. Peyrin, P. Cloetens, C. Odet, A. M. Laval-Jeantet, J. Baruchel, and P. Spanne, "A synchrotron radiation microtomography system for the analysis of trabecular bone samples," *Med. Phys.*, vol. 26, no. 10, pp. 2194-2204, 1999.

[161] D. Rohrbach, S. Lakshmanan, F. Peyrin, and K. Raum, "Spatial distribution of tissue mineralization and anisotropic tissue elastic constants in human femoral cortical bone," *World congress of Medical Physics and Biomedical Engineering, IFMBE proceedings*, no. 25/4, pp. 962-965, 2009.

[162] C. R. Mol and P. A. Breddels, "Ultrasound velocity in muscle," *J. Acoust. Soc. Am.*, vol. 71, no. 2, pp. 455-461, 1982.

[163] D. Shore, M. O. Woods, and C. A. Miles, "Attenuation of ultrasound in post rigor bovine skeletal muscle," *Ultrasonics*, vol. 24, no. 2, pp. 81-87, 1986.

[164] K. A. Topp and W. D. O'Brien, Jr., "Anisotropy of ultrasonic propagation and scattering properties in fresh rat skeletal muscle in vitro," *J. Acoust. Soc. Am.*, vol. 107, no. 2, pp. 1027-1033, 2000.

[165] K. M. Tervola, M. A. Gummer, J. W. Erdman, Jr., and W. D. O'Brien, Jr., "Ultrasonic attenuation and velocity properties in rat liver as a function of fat concentration: a

study at 100 MHz using a scanning laser acoustic microscope," *J. Acoust. Soc. Am.*, vol. 77, no. 1, pp. 307-313, 1985.

[166] E. L. Madsen, F. Dong, G. R. Frank, B. S. Garra, K. A. Wear, T. Wilson, J. A. Zagzebski, H. L. Miller, K. K. Shung, S. H. Wang, E. J. Feleppa, T. Liu, W. D. O'Brien, K. A. Topp, N. T. Sanghvi, A. V. Zaitsev, T. J. Hall, J. B. Fowlkes, O. D. Kripfgans, and J. G. Miller, "Interlaboratory comparison of ultrasonic backscatter, attenuation, and speed measurements.," *Journal of Ultrasound in Medicine*, vol. 18, no. 9, pp. 615-631, 1999.

[167] R. Strelitzki, A. J. Clarke, and J. A. Evans, "The measurement of the velocity of ultrasound in fixed trabecular bone using broadband pulses and single-frequency tone bursts," *Phys. Med. Biol.*, vol. 41, no. 4, pp. 743-753, 1996.

[168] T. Koch, S. Brand, L. Sannachi, K. Raum, M. Wicke, and D. Mörlein, "Ultrasound velocity and attenuation of porcine soft tissues with respect to structure and composition: II. Skin and backfat," *Meat Science*, vol. accepted 2010.

[169] J. A. Jensen and N. B. Svendsen, "Calculation of Pressure Fields from Arbitrarily Shaped, Apodized, and Excited Ultrasound Transducers," *IEEE Transactions On Ultrasonics Ferroelectrics And Frequency Control*, vol. 39, no. 2, pp. 262-267, 1992.

[170] S. Brand, "Ultraschallspektroskopie an fokussierenden Systemen unter Berücksichtigung vorgelagerter absorbierender Schichten." Ph.D thesis Otto - von - Guericke - University Magdeburg, Germany, 2004.

[171] K. Raum, K. Kempf, H. J. Hein, J. Schuber, and P. Maurer, "Preservation of microelastic properties of dentin and tooth enamel in vitro - A scanning acoustic microscopy study," *Dental Materials*, vol. 23, no. 10, pp. 1221-1228, 2007.

[172] K. Raum, "Microelastic imaging of bone," *IEEE Trans Ultrason. Ferroelectr. Freq. Control*, vol. 55, no. 7, pp. 1417-1431, 2008.

[173] S. Lakshmanan, T. Koch, D. Mörlein, S. Brand, and K. Raum, "Intramuscular fat content estimation in the loin muscle pig carcasses by ultrasound spectral parameter analysis," *IFMBE Proceedings*, vol. 25, no. 13, pp. 92-95, 2010.

[174] T. A. Bigelow, M. L. Oelze, and W. D. O'Brien, "Estimation of total attenuation and scatterer size from backscattered ultrasound waveforms," *Journal Of The Acoustical Society Of America*, vol. 117, no. 3, pp. 1431-1439, 2005.

[175] T. A. Bigelow and W. D. O'Brien, "A model for estimating ultrasound attenuation along the propagation path to the fetus from backscattered waveforms," *Journal Of The Acoustical Society Of America*, vol. 118, no. 2, pp. 1210-1220, 2005.

[176] N. Männicke, T. Koch, S. Lakshmanan, D. Mörlein, and K. Raum, "Application of cepstral analysis for ultrasonic structural parameter characterization," *BMT 2010 Proceedings, submitted*, 2010.

[177] J. M. Bland and D. G. Altman, "Statistical methods for assessing agreement between two methods of clinical measurement," *Lancet*, vol. 1, no. 8476, pp. 307-310, 1986.

[178] S. Lees, J. D. Heeley, and P. F. Cleary, "A study of some properties of a sample of bovine cortical bone using ultrasound," *Calcif. Tissue Int.*, vol. 29, no. 2, pp. 107-117, 1979.

[179] J. Y. Rho, "An ultrasonic method for measuring the elastic properties of human tibial cortical and cancellous bone," *Ultrasonics*, vol. 34, no. 8, pp. 777-783, 1996.

[180] W. C. Van Buskirk, S. C. Cowin, and R. N. Ward, "Ultrasonic measurement of orthotropic elastic constants of bovine femoral bone," *J. Biomech. Eng*, vol. 103, no. 2, pp. 67-72, 1981.

[181] H. S. Yoon and J. L. Katz, "Ultrasonic properties and microtexture of human cortical bone," *Ultrasonic Tissue Characterization II*, no. Washington, D.C.: National Bureau of Standards, Spec.Publ. 525, pp. 189-196, 1979.

[182] M. C. Zimmerman, A. Prabhakar, B. V. Chokshi, N. Budhwani, and H. Berndt, "The Acoustic Properties of Normal and Imbedded Bovine Bone As Measured by Acoustic Microscopy," *Journal of Biomedical Materials Research*, vol. 28, no. 8, pp. 931-938, 1994.

[183] F. G. EVANS and M. LEBOW, "Regional differences in some of the physical properties of the human femur," *J. Appl. Physiol*, vol. 3, no. 9, pp. 563-572, 1951.

[184] G. N. Duda, M. Heller, J. Albinger, O. Schulz, E. Schneider, and L. Claes, "Influence of muscle forces on femoral strain distribution," *J. Biomech.*, vol. 31, no. 9, pp. 841-846, 1998.

[185] A. D. Speirs, M. O. Heller, G. N. Duda, and W. R. Taylor, "Physiologically based boundary conditions in finite element modelling," *J. Biomech.*, vol. 40, no. 10, pp. 2318-2323, 2007.

[186] R. B. Martin and P. J. Atkinson, "Age and sex-related changes in the structure and strength of the human femoral shaft," *J. Biomech.*, vol. 10, no. 4, pp. 223-231, 1977.

[187] T. Kimura and E. Amtmann, "Distribution of mechanical robustness in the human femoral shaft," *J. Biomech.*, vol. 17, no. 1, pp. 41-46, 1984.

[188] Sobotta, "Atlas of Human Anatomy,", 13th Edition CD ed.

[189] X. N. Dong and X. E. Guo, "The dependence of transversely isotropic elasticity of human femoral cortical bone on porosity," *J. Biomech.*, vol. 37, no. 8, pp. 1281-1287, 2004.

[190] W. D. O'Brien and J. E. Olerud, "Ultrasonic assessment of tissue anisotropy," *IEEE Ultrasonics symposium*, pp. 1145-1148, 1995.

[191] V. Roberjot, P. Laugier, and G. Berger, "Anisotropy in bovine skeletal muscle in vitro: Frequency dependent attenuation and backscatter coefficient over a wide range of frequencies," *IEEE Ultrasonics symposium*, pp. 1467-1470, 1994.

[192] B. K. Hoffmeister, E. D. Verdonk, S. A. Wickline, and J. G. Miller, "Effect of collagen on the anisotropy of quasi-longitudinal mode ultrasonic velocity in fibrous soft tissues: a comparison of fixed tendon and fixed myocardium," *J. Acoust. Soc. Am.*, vol. 96, no. 4, pp. 1957-1964, 1994.

[193] E. D. Verdonk, S. A. Wickline, and J. G. Miller, "Anisotropy of ultrasonic velocity and elastic properties in normal human myocardium," *J. Acoust. Soc. Am.*, vol. 92, no. 6, pp. 3039-3050, 1992.

[194] A. Karlsson, A. C. Enfalt, B. Essen-Gustavsson, K. Lundstrom, L. Rydhmer, and S. Stern, "Muscle histochemical and biochemical properties in relation to meat quality during selection for increased lean tissue growth rate in pigs," *J. Anim Sci*, vol. 71, no. 4, pp. 930-938, 1993.

[195] E. L. Bradley, III and J. Sacerio, "The velocity of ultrasound in human blood under varying physiologic parameters," *J. Surg. Res.*, vol. 12, no. 4, pp. 290-297, 1972.

[196] H. Sasaki, Y. Saijo, M. Tanaka, and S. Nitta, "Influence of tissue preparation on the acoustic properties of tissue sections at high frequencies," *Ultrasound Med. Biol.*, vol. 29, no. 9, pp. 1367-1372, 2003.

[197] S. Brand, E. C. Weiss, R. M. Lemor, and M. C. Kolios, "High frequency ultrasound tissue characterization and acoustic microscopy of intracellular changes," *Ultrasound Med. Biol.*, vol. 34, no. 9, pp. 1396-1407, 2008.

[198] J. D. Wood, M. Enser, A. V. Fisher, G. R. Nute, P. R. Sheard, R. I. Richardson, S. I. Hughes, and F. M. Whittington, "Fat deposition, fatty acid composition and meat quality: A review," *Meat Science*, vol. 78, no. 4, pp. 343-358, 2008.

[199] F. L. Lizzi, M. Astor, E. J. Feleppa, M. Shao, and A. Kalisz, "Statistical framework for ultrasonic spectral parameter imaging," *Ultrasound Med. Biol.*, vol. 23, no. 9, pp. 1371-1382, 1997.

[200] L. Maignel, J. P. Daigle, C. Gariépy, D. Wilson, and B. Sullivan, "Prediction of intramuscular fat in live pigs using ultrasound technology and potential use in selection.," *9th World Congress on Genetics Applied to Livestock Production*, 2010.

Acknowledgements

My most profound thanks go to my supervisor Prof. Dr. Kay Raum for giving me this great opportunity to work in his group. Thank you for your continuous support during hard times, encouragement and fruitful discussions.

My thanks also to go my collaborator Dr. Daniel Mörlein and Prof. Michael Wicke, Department of Animal Sciences, University of Göttingen for supporting the muscle project and valuable discussions from a biological point of view.

I would like to thank my collaborator Tim Koch, Department of Animal Sciences, University of Göttingen for muscle sample preparation, chemical analysis and valuable discussions from a biological point of view.

I also offer thanks to Dr. Sebastian Brand, Fraunhofer Institute for Mechanics and Materials, Halle and Nils Männicke for helping me in signal processing in the muscle project

To Andreas Bodi, Department of Orthopedics, Martin Luther University of Halle – Wittenberg and Daniel Rohrbach I offer my thanks for giving me some ideals on data analysis in the bone project and regarding synchrotron radiation data processing, and also for their ideas to improve my Matlab programming.

I like to thank Deutsche Forschungsgemeinschaft (grant Ra1380/1 and Ra1380/3) and SFK Technology GmbH for their financial support.

Special thanks go to Martin Schöne, Ferenc Lajos Molnar, Bernhard Hesse and Katrein Sauer for spending time in my thesis correction and for the help with the translation and for giving me company during my long stays in the lab.

Many thanks go also to my friends and family for their moral support and love over the years.

Selbständigkeitserklärung

Hiermit erkläre ich eidesstattlich, dass ich die hier vorliegende Arbeit selbst verfasst und nur die angegenennen Hilfsmittel verwendet habe.

Berlin